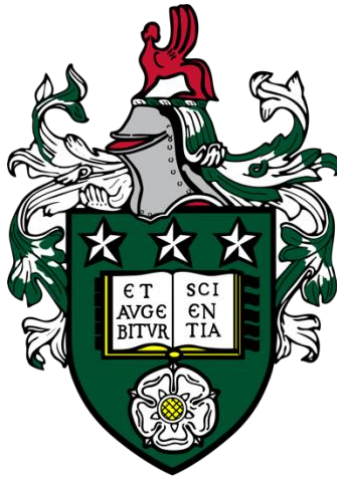# An Anthropomorphic Multimodality (CT/MRI) Head and Neck Phantom for Radiotherapy Applications

Meshal Alzahrani

Submitted in accordance with the requirements for the degree of
Doctor of Philosophy

The University of Leeds
School of Medicine

October 2024

Intellectual Property and Publication Statement

The candidate confirms that the work submitted is his own, except where work which has formed part of jointly authored publications has been included. The contribution of the candidate and the other authors to this work has been explicitly indicated below. The candidate confirms that appropriate credit has been given within the thesis where reference has been made to the work of others.

1. **Chapter 4** forms the basis for the manuscript titled "Assessing suitability and stability of materials for a head and neck anthropomorphic multimodality (MRI/CT) phantoms for radiotherapy". *Physics in Medicine & Biology*. Published.
   https://doi.org/10.1088/1361-6560/ad8830
2. **Chapter 5** forms the basis for the manuscript titled "A novel multimodality anthropomorphic phantom enhances compliance with quality assurance guidelines for MRI in radiotherapy". *Physics and Imaging in Radiation Oncology*. Revised and resubmitted.
3. **Chapter 6** forms the basis for the manuscript titled "Optimisation of cone beam CT radiotherapy imaging protocols using a novel 3D printed Head and Neck anthropomorphic phantom" *Physics in Medicine & Biology*. Published.
   https://doi.org/10.1088/1361-6560/ad88d2

Contributions of the Candidate and Team Members

Authors: Meshal Alzahrani (MA), David A Broadbent (DAB), Irvin Teh (IT), Bashar Al-Qaisieh (BAQ), Christopher O'Hara (CO), David Bird (DB), Jack Baldwin (JB), Mitchell Naisbit (MN), Emily Johnston (EJ), and Richard Speight (RS)

Chapter 4

MA (the candidate): Designed the study, prepared samples, conducted data collection and analysis, and write-up.

RS, DAB, IT, and BAQ: Provided supervision and feedback on drafts.

BAQ and RS: Assisted in implementing the sample exposure to radiation.

DAB and RS: Assisted with MRI and CT scans to investigate stability over time and after radiation exposure.

DAB: Developed the MATLAB code used to create the T1 and T2 maps.

Chapter 5

MA (the candidate): Designed the study, conducted all required MRI and CT scans, developed and implemented the radiotherapy plan, performed data analysis, and write-up.

RS, DAB, IT, and BAQ: Provided supervision and feedback on drafts.

DAB and RS: Assisted with the MRI and CT scans.

BAQ: Assisted with performing end-to-end testing on the linear accelerator for the plan designed by the candidate.

DAB: Wrote the MATLAB code for analysing the relationship between transmit gain and signal intensity.

EJ and RS: Developed the multimodality anthropomorphic phantom.

Chapter 6

MA (the candidate): Designed the study, conducted the CT and CBCT scans, performed data analysis, and write-up.

RS, DAB, IT, MN and BAQ: Provided supervision and feedback on drafts.

CO: Assisted in conducting the CBCT scans as proposed by the candidate.

JB: Provided the technical support needed to reconstruct the CBCT images as requested by the candidate.

CO, DB and RS: Assessed the CBCT image quality and usability as requested by the candidate.

EJ and RS: Developed the multimodality anthropomorphic phantom.

Acknowledgements

Publications and Presentations

Published Papers

Alzahrani, M., et al. "Assessing suitability and stability of materials for a head and neck anthropomorphic multimodality (MRI/CT) phantoms for radiotherapy." *Physics in Medicine & Biology,* 69.21 (2024): 215034. https://doi.org/10.1088/1361-6560/ad8830 *(Based on Chapter 4).*

Alzahrani, M., et al. "Optimisation of cone beam CT radiotherapy imaging protocols using a novel 3D printed head and neck anthropomorphic phantom." *Physics in Medicine & Biology,* 69.21 (2024): 215031. https://doi.org/10.1088/1361-6560/ad88d2 *(Based on Chapter 6)*

Alzahrani, M., et al. "Audit feasibility for geometric distortion in magnetic resonance imaging for radiotherapy." *Physics and Imaging in Radiation Oncology,* 15 (2020): 80-84. https://doi.org/10.1016/j.phro.2020.07.004 *(Based on MSc Research Project).*

Under Review

Alzahrani, M., et al. "A novel multimodality anthropomorphic phantom enhances compliance with quality assurance guidelines for MRI in radiotherapy" Submitted to *Physics and Imaging in Radiation Oncology*. *(Based on Chapter 5)*

Conference Publications

Alzahrani, M., et al. "PO-1731 Evaluation of materials suitable for anthropomorphic multimodality (CT/MRI) phantoms for RT purposes". *Radiotherapy and Oncology,* 182 (2023): S1449-S1451. Presented at the ESTRO 2023 Annual Meeting, Vienna, Austria.

Conferences

"Do anthropomorphic phantoms enhance compliance with the professional bodies' quality assurance guidelines for MRI in radiotherapy?" presented at:

- The Annual Meeting of the British and Irish International Society for Magnetic Resonance in Medicine (BIC-ISMRM) Chapter, Aberdeen, 13-15 September 2023. *Poster Presentation*.
- The Annual Meeting of the International Society for Magnetic Resonance in Medicine (ISMRM), Toronto, 3-8 June 2023, *Poster Presentation*.

"Stability of an anthropomorphic multimodality (CT/MRI) head and neck phantom for radiotherapy QA" presented at:

- The Annual Meeting of the British and Irish International Society for Magnetic Resonance in Medicine (BIC-ISMRM) Chapter, Cardiff, 7-9 September 2022. *Poster Presentation*.
- Magnetic resonance in Radiotherapy meeting, Institute of Physics and Engineering in Medicine (IPEM), Manchester, 17 May 2022. *Poster Presentation.*

Abstract

Aims

To develop and evaluate an anthropomorphic multimodality phantom for the head and neck (H&N) anatomy that can be used with computed tomography (CT) and magnetic resonance imaging (MRI) for radiotherapy (RT) applications. The research aims to identify suitable materials for creating these phantoms, assess the suitability and effectiveness of a 3D head and neck phantom for MRI-based quality assurance (QA) in RT planning, and to optimise cone beam computed tomography (CBCT) protocols for H&N imaging as part of QA processes.

Methods

Through literature research, candidate materials potentially suitable for developing multimodality (MRI/CT) phantoms were identified and produced. Their suitability and stability over time and after exposure to radiation were then evaluated. An anthropomorphic multimodality H&N phantom was used to evaluate the benefits of using such a phantom for conducting QA tests recommended by international bodies in MRI guided RT treatment planning services. Moreover, the scope of the phantom's use has been expanded to include optimising CBCT protocols, further demonstrating its value in enhancing QA processes across multiple imaging modalities.

Results

The results of this project indicate that while some materials meet specific requirements for creating anthropomorphic multimodality phantoms, it has been challenging to find materials that simultaneously satisfy the needs of both MRI and CT modalities. However, the results have shown that the T1 and T2 relaxation times and CT numbers of 10% polyvinyl alcohol cryogel closely match those of normal brain grey matter, and remain stable over a year, and after exposure to radiation levels up to 1000 Gy, demonstrating its potential effectiveness in making phantoms. The anthropomorphic multimodality phantom has demonstrated superior performance to non-anthropomorphic phantoms in certain aspects of MRI-based RT planning QA, particularly in end-to-end testing. The phantom can be used in optimising CBCT protocols as part of QA processes, with results showing that it allows for a reduction in radiation doses by more than 50% compared to the default protocol for patients with head and neck tumours without significantly affecting image or registration quality and with the expectation that this would not have a consequential impact on treatment plans.

Conclusions

The identification of only one suitable material underscores the need for expanded research into multimodality phantom materials. The phantom proves effective for MRI-based QA. Additionally, it was employed to test and optimise CBCT protocols, leading to reductions in radiation doses without compromising image quality.

Table of Contents

List of Figures

List of Tables

List of Abbreviations

AAPM	American Association of Physicists in Medicine
ACR	American College of Radiology
AEC	Automatic Exposure Control
AI	Artificial Intelligence
ALARP	As Low As Reasonably Practicable
ART	Adaptive Radiotherapy
$BaSO_4$	Barium Sulphate
CBCT	Cone Beam Computed Tomography
CIRS	Computerized Imaging Reference Systems
CNR	Contrast-To-Noise
CT	Computed Tomography
CTV	Clinical Target Volume
$CuSO_4$	Copper (II) Sulfate
DICOM	Digital Imaging and Communications in Medicine
DNA	Deoxyribonucleic acid
DSC	Dice Similarity Coefficient
EBRT	External-Beam Radiation Therapy
FFF	Flattening Filter-Free
FOV	Field of View
FTC	Freeze-Thaw Cycle
Gd	Gadolinium
GNL	Gradient nonlinearity
GRE	Gradient Echo
GTV	Gross Tumour Volume
H&N	Head-and-Neck
HNC	Head and neck cancer
HU	Hounsfield Unit
ICRU	International Commission on Radiation Units and Measurements
IMRT	Intensity Modulated Radiotherapy
IPEM	Institute of Physics and Engineering in Medicine
IR	Inversion Recovery
IRT	Internal Radiation Therapy
kV	Kilovoltage
LCC	Leeds Cancer Centre

Linac	Linear accelerator
LTHT	Leeds Teaching Hospitals NHS Trust
LTO	Leeds Test Objects
mA	Milliampere
MAE	Mean Absolute Error
mAs	Milliampere-Seconds
MDA	Mean Distance to Agreement
MLC	Multi-leaf Collimator
MV	mega-voltage
MR-Linac	Magnetic Resonance Linear Accelerator
MRgRT	Magnetic Resonance-Guided Radiotherapy
MRI	Magnetic Resonance Imaging
ms	Milliseconds
MU	Monitor Unit
NEX	Number of Excitations
OAR	Organ at Risk
pC	PicoCoulombs
PET	Positron Emission Tomography
PET/CT	Positron Emission Tomography/Computed Tomography
PIU	Percent Image Uniformity
PPM	Part per Million
PSG	Percent Signal Ghosting
PTV	Planning Target Volume
PVA	Polyvinyl Alcohol
PVA-c	Polyvinyl Alcohol cryogel
QA	Quality Assurance
R&V	Record and Verify
RF	Radiofrequency
ROI	Region of Interest
ROUT	Robust Regression and Outlier Removal
RT	Radiotherapy
sCT	Synthetic Computed Tomography
SD	Standard Deviation
SE	Spin Echo
SNR	Signal-to-Noise Ratio
SPECT/CT	Single photon emission tomography/computed tomography

SRS	Stereotactic Radiosurgery
SSD	Source to Skin Distance
STEEV	Stereotactic End-to-End Verification Phantom
STL	Stereolithography
TE	Echo Time
TLD	Thermoluminescent Dosimeters
TMM	Tissue-Mimicking Material
TPS	Treatment Planning System
TR	Repetition Time
TRE	Target Registration Error
UTE	Ultra-short Echo-time
VMAT	Volumetric Modulated Arc Therapy
WHO	World Health Organization
3D-CRT	3D-conformal radiotherapy

Chapter 1 Introduction

1.1 Introduction to the research question

In medical imaging and radiotherapy (RT), phantoms are test objects that can be imaged or irradiated for use in quality assurance (QA) (1), training (2) and research (3). Phantoms have been used since the risk of exposure to ionising radiation was recognised soon after the discovery of X-rays (4). A phantom's design depends on the system for which it will be used and the purpose it intends to serve. Some have simple designs, while others, such as anthropomorphic phantoms, are more complex (5).

In RT for head and neck (H&N) cancers, imaging plays an important role in both treatment planning and delivery. Traditionally, RT planning has relied on computed tomography (CT) scans. In recent years, magnetic resonance imaging (MRI) has been increasingly used alongside CT to improve soft-tissue contrast and precision in RT planning (6, 7). Additionally, cone beam computed tomography (CBCT) is essential for real-time imaging during treatment, improving patient positioning, and ensuring precise radiation delivery by detecting anatomical changes (8). Linear accelerators (linacs), which deliver high-energy radiation to target tumours, have been recently advanced to heighten their precision and effectiveness in cancer treatment. These developments, along with improvements in imaging techniques, have revolutionised the planning and delivery of RT. Although these new technologies and developments help improve RT and reduce mistakes, they can also introduce new sources of error (9, 10). The continuous development of RT planning and delivery has led to the need for multimodal phantoms specifically for RT purposes in H&N patients (11, 12).

The majority of the current phantoms used in RT are either simple, such as homogeneous or geometric phantoms that lack anatomical detail, or are specifically designed for certain imaging modalities. However, the lack of human-like anatomical details in the former may limit their applicability and potentially reduce the reliability of the results derived from them. Phantoms for specific imaging modalities may not assess the entire RT pathway, including MRI/CT imaging, image registration, and therapeutic linac dose delivery. Therefore, the need for multimodality anthropomorphic phantoms for RT is increasing. Furthermore, in order to ensure consistent QA and reproducible results, the material properties of these phantoms must be stable not only over their lifetimes, but also after exposure to radiation. Despite this, only a limited number of such phantoms exist, and their full potential has yet to be thoroughly explored.

1.2 Aims and Objectives

This research project aims to evaluate anthropomorphic multimodality phantoms and explore their benefits. The H&N region was chosen due to its being one of the most common areas for MRI use in RT. While this project focuses exclusively on the H&N region, the principles and methodologies developed may have broader applicability to other anatomical areas. The objectives of this project will be achieved through the following steps:

1. Assessing the availability of suitable materials for the development of anthropomorphic multimodality (CT/MRI) H&N phantoms.
2. Evaluating the effectiveness of these phantoms for QA for MRI in RT planning.
3. Employing these phantoms to optimise CBCT acquisition protocols for H&N as part of QA.

1.3 Novelty of the Research

Previous studies (13-15) have identified potentially suitable materials for multimodal phantoms, as they mimic the properties of human tissue in MRI, CT, or both. Some of these materials have only been evaluated for a single imaging modality without considering their long-term or post-radiation stability. Addressing this gap is crucial for the development of commercial phantoms suitable for use in RT clinics.

Guidelines published in 2021 by the Institute of Physics and Engineering in Medicine (IPEM) (16) and the American Association of Physicists in Medicine (AAPM) (17) for MRI simulation in RT are expected to influence practices in RT clinics worldwide. While recommending commissioning and QA tests, these guidelines leave the methodology itself open, dependent on the chosen phantom. To the best of the researcher's knowledge, this project is the first to evaluate a multimodality anthropomorphic phantom against others, aiming to meet the guidelines' specified QA standards. By examining QA tests, methodologies, and phantoms, this research aims to support RT centres in choosing suitable phantoms for MRI.

Despite advances in RT, further research is needed on the optimisation of CBCT protocols, and improvements in image quality and reductions in the radiation dose required for CBCT to enhance its application in RT. As ethical and safety concerns prohibit the use of patient exposure for protocol testing, the role of anthropomorphic phantoms becomes critical. Despite their value, the accuracy of commercial phantoms in replicating patient anatomy is limited (18). One project in this thesis involved conducting experiments using the same 3D-printed multimodality anthropomorphic phantom to optimise CBCT scan protocols. Through the innovative application of the phantom, this research contributes to

the advancement of safer and more efficacious RT practices, and demonstrates an additional area where such phantoms may have value beyond QA for MRI.

1.4 Overview of the Thesis

The remainder of this thesis is structured as follows. Chapter 2 outlines the background to RT and associated imaging techniques relevant to the objectives of this project. Chapter 3 presents a review on anthropomorphic multimodality (CT/MRI) H&N phantoms, focusing on their capabilities and limitations. To develop such phantoms, it is crucial to identify the most appropriate materials, a search to which Chapter 4 is dedicated. In Chapter 5 and Chapter 6, the same anthropomorphic multimodality H&N phantom is used. Chapter 5 uses the phantom to conduct QA tests for MRI in RT planning. These tests compare the efficacy of the anthropomorphic phantom to other conventional phantoms, assessing which is more suitable for compliance with the 2021 guidelines (16, 17). Chapter 6 demonstrates how the phantom can be used to optimise CBCT protocols specifically for H&N patients, exploring their application to improve patient care. The final chapter offers a general discussion on the use of anthropomorphic multimodality phantoms, collating insights from previous experimental chapters and presenting recommendations for future work.

Chapter 2 background

2.1 Head and neck cancer (HNC)

Head and neck cancer (HNC) comprises the sixth most common form of cancer globally, with estimations indicating that 660,000 people per year are newly diagnosed, with 325,000 annual deaths (19). HNC incidence is still rising, with predictions suggesting that it will increase by 30% annually by 2030 (84). HNC is frequently treated using RT (20). The H&N region, including the skull, vertebra, facial bones, and air cavities, present challenges for RT due to the proximity of organs at risk (OARs) (21) such as the brain stem, spinal cord, parotid glands, and optical structures. Due to the high radiosensitivity of various OARs in this region, individuals receiving RT for HNC can experience significant side effects, categorised as early (acute) or long term (chronic) (22). The former manifest during the delivery of therapy, as well as immediately after its completion (around two to three weeks after the end of an RT course), and can include mucositis and oedema, which impair the ability to swallow when the treatment process is ongoing (23). Long-term effects can occur at any point in the ensuing period and may manifest weeks or even years after the treatment (24), including neuropathy, as well as fibrosis of the pharyngeal, laryngeal, and oral musculature (25). As survival rates for patients with HNC improve following RT (26, 27), these individuals may experience persistent side effects from the treatment, even after considerable time has passed.

Imaging plays a crucial role in the RT workflow by improving the treatment for HNC patients. The use of MRI has become more prevalent, owing to its superior soft-tissue contrast (28), which enhances target delineation and helps distinguish tumours from surrounding healthy tissue. This precision is vital in the H&N region.

Throughout the course of RT, both OARs and target volumes can undergo significant anatomical changes (29), such as tumour shrinkage/growth, parotid gland displacement, and weight loss (30, 31). These changes can significantly affect the dose that is actually delivered to the tumour and/or healthy tissues compared to the planned dose (32). Daily CBCT can help minimise any errors in the set-up between treatments (33). Thus, efforts have been made to investigate the application of CBCT imaging in adaptive radiotherapy (ART), acknowledging its key benefits, despite its constraints (34-36).

2.2 Radiotherapy

RT, surgery, and chemotherapy are cancer treatments that can be used alone or in combination. It is expected that over 50% of patients who develop cancer will be treated with RT, either as a curative and/or adjuvant therapy (37-39). RT was quickly adopted for treating tumours just months after the discovery of X-rays in 1895 (40). It provides comparatively good cost-efficiency, constituting only 5% of the total costs incurred in cancer treatment (41, 42). The specific mechanism by which RT produces its effect is that the cell deoxyribonucleic acid (DNA) is damaged, thus resulting in either the death of the cell or the restriction its reproductive ability. In this process, the objective is to use a radiation dose high enough to eliminate the tumour, while also mitigating the absorption of radiation by healthy organs and tissues in areas adjacent to the cancer cells (43).

Two distinct types of RT are generally employed: internal radiation therapy (IRT) or brachytherapy, and external-beam radiation therapy (EBRT). In the former, one or multiple sources of radiation are situated close to or touching the tumour within the body of the patient (44). In the latter, the radiation source is situated outside the body in an external position. EBRT is the most frequently-used RT type (45), and is predominantly performed using mega-voltage (MV) medical

linacs. Throughout the rest of this thesis, the term 'RT' shall refer to linac-administered EBRT.

2.3 Linear Accelerator (Linac)

A linac is a device in which electrons are accelerated using high-frequency electromagnetic waves in a straight line towards a target material with a high atomic number, generally tungsten. This process results in the production of bremsstrahlung photons that enter the patient's body for the purpose of cancer cell elimination (46-48). The linac head structure is presented in Figure 2-1, and contains numerous components responsible for filtering and shaping the beam of radiation. The intended shape of the beam is achieved by collimating it through the use of both primary and secondary collimators, along with a multi-leaf collimator (MLC). The photon beam can also be attenuated using a flattening filter, thus creating a flat profile. The machine output of the linac device is measured in monitor units (MU), the calibration of which is set to a specific dose in Gy under a specific geometry; defined as the dose calibration of the treatment unit (47).
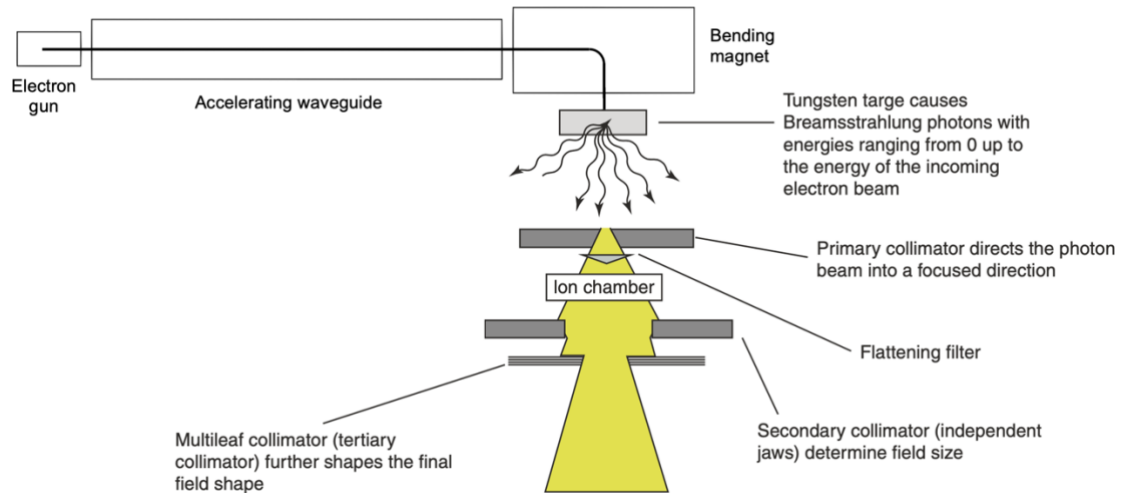
Figure 2-1 Diagram of a linear accelerator head. Reproduced with permission from Springer Nature (47).

2.4 Treatment Technique

Linacs have undergone many technological innovations. This has contributed to the achievement of multiple useful treatment techniques of delivering photon radiation (49), including: 3D-conformal radiotherapy (3D-CRT), intensity modulated radiotherapy (IMRT), and volumetric modulated arc therapy (VMAT).

3D-CRT refers to imaging data-based treatments which generate dose distributions that tightly conform to the target volume while depositing minimal doses to normal tissue. In 3D-CRT, radiation is delivered from static beams, typically from multiple angles and shaped by an MLC to target the tumour while minimising exposure to normal tissue.

IMRT is an advanced form of 3D-CRT, and also based on imaging data, wherein the radiation beam's intensity is dynamically modulated by adjusting the MLC under computer control. This technique provides an additional degree of control (intensity modulation), thus allowing for a more precise and conformal dose distribution to the target volume while minimising exposure to surrounding healthy tissues (50).

In the VMAT approach, the gantry continuously rotates around the patient, delivering radiation. This technique is a rotational form of IMRT, which is typically delivered from multiple static angles. VMAT allows for faster treatment by delivering radiation with single or multiple arcs, while maintaining dose distributions comparable to IMRT (51). Additionally, the beam output and gantry rotation speed can be further modified, thus potentially enhancing the dose distribution conformity (52).

2.5 Radiotherapy Clinical Pathway

RT pathways show the steps for treating cancer patients. The steps included in this process include diagnosing and staging the tumour, simulating and planning treatment, and delivering the required dosage and monitoring outcomes. Medical imaging is a key factor throughout all RT stages (53, 54). Although several different systems can be used for imaging in RT, those techniques which are of particular relevance to the scope of this thesis will be the focus of this background.

2.5.1 Simulation and treatment planning

After diagnosing and staging the tumour, simulation is the second step of the RT process. In this stage, the targeted treatment area is scanned, producing detailed images. The objective is to create an accurate depiction of both the area in which the tumour is located and the neighbouring anatomy. During this process, the patient is required to adopt the same position they will be in during actual treatment sessions. This position is maintained through such immobilisation equipment as masks. Tattoos or markers are placed on the skin to allow the position to remain the same in subsequent treatment sessions using the same laser system as in the simulation scanning room and the linac (55). For H&N patients, 5-point thermoplastic masks are often used (56). These are carefully

crafted so as to conform to the contours of human H&N anatomy. Before being moulded to the patient's specific features, the mask is heated in water to make it pliable. Once cooled, it hardens, ensuring the H&N remain immobilised in the exact therapeutic position. The simulation process is critical for exactly describing the area to be treated and directing the process of planning the subsequent treatment.

Prior to undergoing RT, a treatment plan needs to be prepared for the patient. There are generally two key stages involved in planning treatment: determining what will be treated and how it will be treated. A treatment planning system (TPS) is used for designing a treatment plan that is tailored to the patient's specific situation. This typically involves creating a patient model using medical images. An oncologist then contours the target volumes and relevant OARs on the model, which vary depending on the treatment site. Once done, the spatial distribution of the dose is overlaid on this model. The type of RT technique to be used is also decided at this point. In 3DCRT, a traditional forward planning approach is used, where the planner manually selects beam angles and shapes. In contrast, such techniques as IMRT and VMAT use inverse planning, where the desired dose is defined based on clinical objectives, after which the computer optimises the beam delivery.

When prescribing the dose to be administered in the treatment, the guidelines of the International Commission on Radiation Units and Measurements (ICRU) are generally followed (57). As shown in Figure 2-2, RT target volume is grouped into three different categories. Based on the ICRU reports (58-60), the primary site in which the tumour is located is described as gross tumour volume (GTV), which constitutes the verifiable malignant mass within the image. The clinical target volume (CTV) is defined as the area encompassing the GTV plus a margin that

includes sub-clinical growth. This margin consists of various cancerous structures not visible on imaging, but assumed to contain a significant number of cancer cells surrounding the GTV. The planning target volume (PTV) comprises the CTV in addition to a margin that incorporates the unpredictability of the process through which radiotherapy is planned and delivered, as well as any possible inter- and intra-fraction motion of both the tumour and patient. The margin's size can vary according to the magnitude of the uncertainties, thus ensuring that the prescription dose is administered to the CTV in the treatment delivery process.
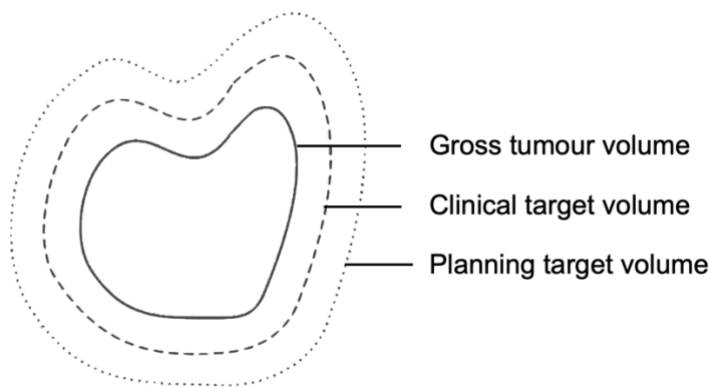
Figure 2-2 A schematic illustration of ICRU volumes.

OARs comprise normal tissue that can potentially be damaged from radiation exposure. In theory, all tissues that are not specifically targeted can be considered OARs (61), but the choice as to which healthy tissues are classified as such for a specific patient is dependent on the tumour's position, the prescribed dosage, and the inherent radiosensitivity of these tissues. These healthy tissues may be sensitive to radiation and are located near the treatment area. Therefore, minimising the dose received by the OARs is crucial to maintain the organ's function and reduce the risk of radiation-induced side effects (62, 63).

2.5.1.1 Imaging used in simulation and planning

CT scans are the predominant imaging technique in RT planning. They offer precise spatial detail (64, 65) and provide the information needed for dose calculation, whether as relative electron or mass density, depending on the TPS and its dose calculation algorithm (66-68). However, CT scans have limited soft-tissue contrast due to the similarity in the linear attenuation coefficients of soft tissues across the kilovoltage spectrum (53). MRI can be used to enhance the precision of tumour targeting, reducing the risk to healthy tissues. This is because MRI scans offer significantly improved soft-tissue contrast compared to CT scans (69, 70). CT or MRI simulators are similar to diagnostic scanners but are specifically adapted for the RT environment to ensure precise patient setup and alignment. Key adaptations include flat table tops or couches that replicate those used on linacs, external laser positioning systems for accurate patient alignment, and immobilization devices to maintain consistent patient positioning during imaging and subsequent treatment (71, 72).

Computed Tomography (CT)

CT is a medical imaging technique in which X-rays are used in combination with computer reconstruction technology to generate comprehensive cross-sectional images of the patient. CT scanning involves positioning the patient inside the scanner's gantry, which emits a thin beam (fan beam) of X-rays via an X-ray tube that revolves around the patient. When traversing the patient's body, the radiation emitted is attenuated by the bodily tissues at different levels according to their density. It is then possible to measure any residual radiation exiting the patient using detectors positioned on the gantry's other side. The radiation source revolves around the patient, enabling data to be captured from various different angles. At the same time, the table on which the patient is positioned can

transition axially, facilitating the reconstruction of multiple slices. Subsequently, advanced mathematical algorithms are employed to reconstruct the data captured from multiple angles directly into a 3D volumetric dataset (73). In a CT image, each pixel represents relative X-ray attenuation of a tissue compared to water at its specific location, known as the CT number expressed in Hounsfield unit (HU) and described by Equation 2-1 (74).

$$CT\ Number\ (HU) = \frac{\mu_t - \mu_w}{\mu_w} \times 1000$$ **Equation 2-1**

μ_t: the linear attenuation coefficient of the tissue.

μ_w: the linear attenuation coefficient of water.

The CT number provides essential information for differentiating various anatomical structures in H&N imaging. For example, bone typically ranges from 700 to 3000 HU (75), making it one of the most attenuating tissues, easily distinguishable in CT scans. Soft tissues exhibit lower HU values, such as 20-30 HU for brain white matter, 30-40 HU for brain grey matter, and 20-40 HU for muscle, depending on specific density and composition. Fat, with a much lower density, typically ranges between -30 to -70 HU, while cancellous bone falls between 300 to 400 HU. Air spaces, such as the sinuses and airway, remain at approximately -1000 HU due to minimal attenuation (76). These HU ranges are indispensable for delineating anatomical structures, identifying pathological changes, and defining target volumes in RT planning. However, the ability of CT to differentiate soft tissues is constrained by the minimal variation in their attenuation properties within the kilovoltage range (53), which may necessitate the use of complementary imaging modalities like MRI for enhanced contrast.

Magnetic Resonance Imaging (MRI)

A different type of imaging technique used is MRI, which can more effectively differentiate between types of soft tissue (77). MRI devices are comprised of various different components, including the magnet, gradient coil, and radiofrequency (RF) coils (78).

The basis of MRI is the nuclear magnetic resonance (NMR) phenomenon, which is derived from the fact that specific atomic nuclei possess magnetic moments due to their spin, similar to a standard bar magnet. When a magnetic field is applied, this causes the magnetic moments to rotate in a manner called precession, which is similar to how spinning tops slowly wobble (79) (Figure 2-3). The frequency of this precession is predictable and can be calculated by multiplying the gyromagnetic ratio (γ) of the nuclei by the strength of the external magnetic field (80).
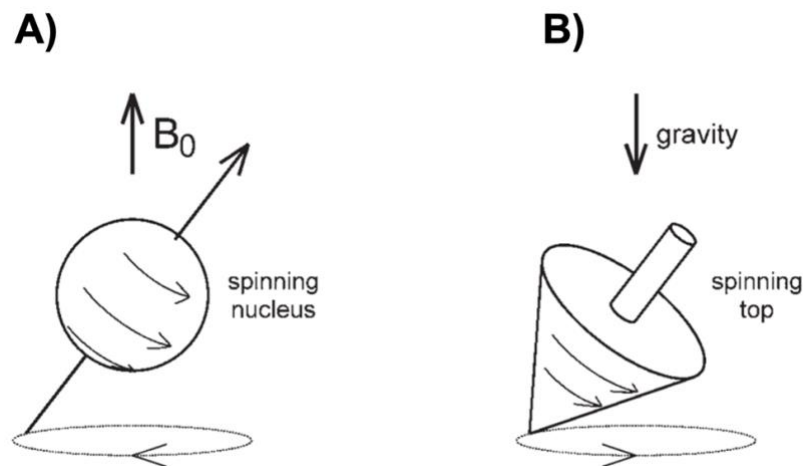
Figure 2-3 Precession phenomenon. A) When a magnetic field is applied externally, (B0) nuclei undergo precession about the field, B) which is a similar motion to a spinning top; here, gravity constitutes the vertical force. Reproduced with permission from Humana Press (79).

MRI is usually used to leverage the magnetic properties of hydrogen protons in the body. The nucleus of a hydrogen atoms contains an individual proton that

functions as a small magnet. Without an external magnetic field, these tiny magnets (protons) are oriented in random directions, leading to their magnetic moments cancelling each other out, resulting in a net magnetic moment of zero. When placed inside the MRI scanner, the strong external magnetic field, known as the main magnetic field (B0), causes all the protons to precess and a small number to slowly. As a result there is a slight excess of protons that align parallel to the magnetic field. This excess creates a net magnetisation (M) in the direction of the magnetic field (or the z-direction), known as the longitudinal magnetisation (Mz) (81) (Figure 2-4).
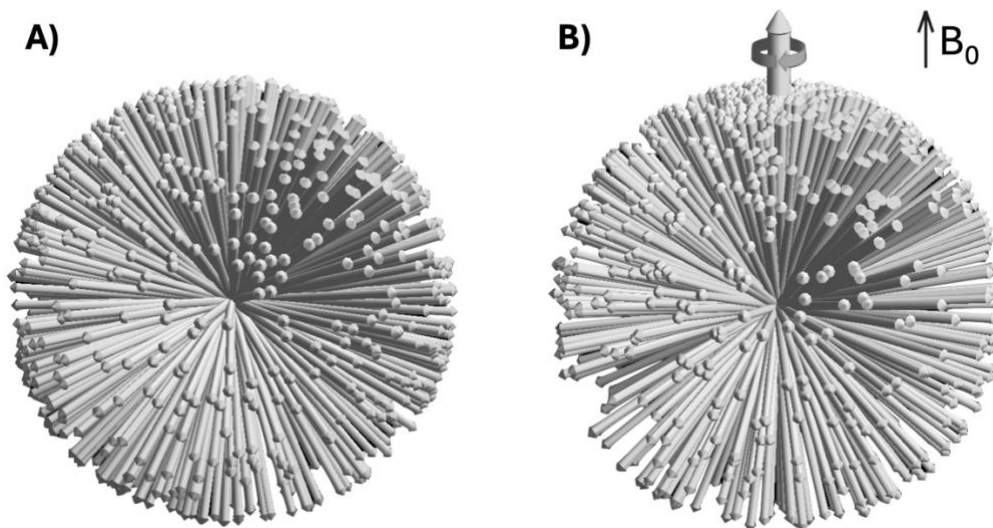
Figure 2-4 Spin distribution for a large number of protons. A) Random proton spin distribution in the absence of a magnetic field resulting in no net magnetization. B) Spin distribution in the presence of a magnetic field (B$_0$) pointing upward and a net magnetisation has developed. Reproduced with permission from authors (82).

After the alignment of hydrogen atoms under the influence of the B0 field, MRI uses a secondary magnetic field generated by a RF pulse, often referred to as B1. The RF pulse is applied perpendicular to the direction of B0 and is tuned to match the precession frequency of the hydrogen atoms, known as the Larmor frequency (ω). This precise matching allows the RF pulse to effectively interact

with the aligned protons. The application of the B1 field temporarily disturbs the stable alignment of the protons with the B0 field. Instead of remaining in their aligned state, the protons are forced to move out of alignment and precess in the transverse plane (the x-y plane) and also brings the individual spins into phase, a phenomenon known as transverse magnetization (Mxy) (79) (Figure 2-5).
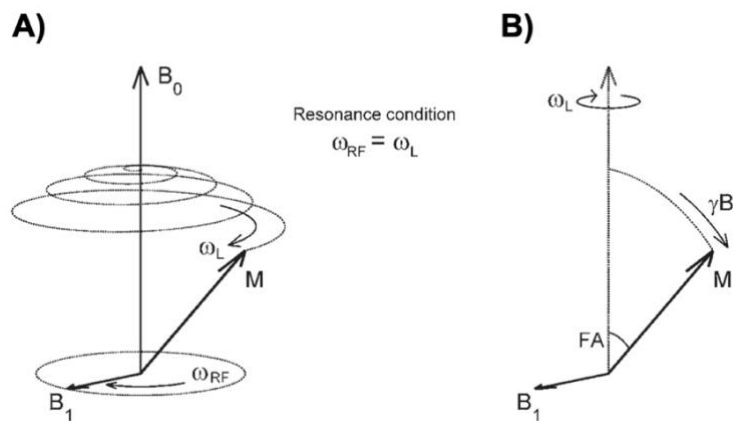
Figure 2-5 Behaviour of magnetisation (M) in an MRI system: A) In the laboratory frame, M creates a helical path around the main magnetic field (B0) due to the influence of the radiofrequency field (B1); and B) In the rotating frame, the B1 field appears static, and M is tipped towards the transverse plane. ω_{RF} is the frequency of the applied RF pulse. ω_L is Larmor frequency, the angular frequency of nuclear magnetic moment precession in the magnetic field. γ is the gyromagnetic ratio. Reproduced with permission from Humana Press (79).

After the RF pulse is turned off, the protons gradually return to their alignment with the B0 field, a process known as relaxation, emitting radio waves as they do so. These waves can be detected and used to generate an MRI image. Relaxation results from the transfer of energy to the surrounding environment, leading to an increase in longitudinal magnetisation (Mz), a process defined as T1 relaxation (spin-lattice). Conversely, the transfer of energy between spins themselves causes a decrease in transverse magnetisation (Mxy) due to a dephasing of the spins (referred to as T2 relaxation, spin-spin). Additionally, the observed decay of transverse magnetisation (T2* relaxation) is influenced by

both spin-spin interactions and magnetic field inhomogeneities, leading to faster

dephasing (83) (Figure 2-6).
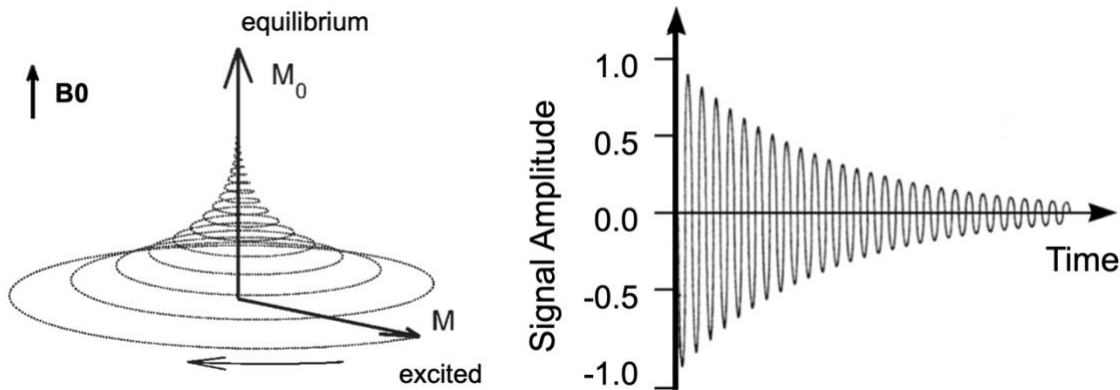
Figure 2-6 Signal measurement: A current is induced in the receiver coil by transverse magnetisation, thus enabling signal collection. As a result of the relaxation process, the signal gradually begins to decay. Reproduced with permission from Humana Press (79).

T1 and T2 are rate constants describing exponential relaxation processes in magnetic resonance. T1 relaxation characterises the recovery of Mz to equilibrium, while T2 relaxation describes the decay of Mxy. The specific values of 63% recovery for T1 and 37% decay for T2 apply after a time equal to one T1 and one T2, respectively, following a 90° pulse from equilibrium. T1 and T2 relaxation are mathematically described by Equation 2-2 and Equation 2-3 respectively.

$$M_z(t) = M_0\left(1 - e^{-t/T1}\right)$$ **Equation 2-2**

$M_z(t)$: Longitudinal magnetization at time t (aligned with the z-axis).

M0: Equilibrium magnetization (maximum when fully relaxed).

T1: Time constant for longitudinal relaxation.

$$M_{xy}(t) = M_{xy}(0).e^{-t/T2}$$

Equation 2-3

$M_{xy}(t)$: Transverse magnetization at time t (in the xy-plane).

M_{xy}: Initial transverse magnetization.

T2: Time constant for transverse relaxation.

Figure 2-7 and Figure 2-8 visually represent the exponential recovery and decay curves for T1 and T2 relaxation, respectively.
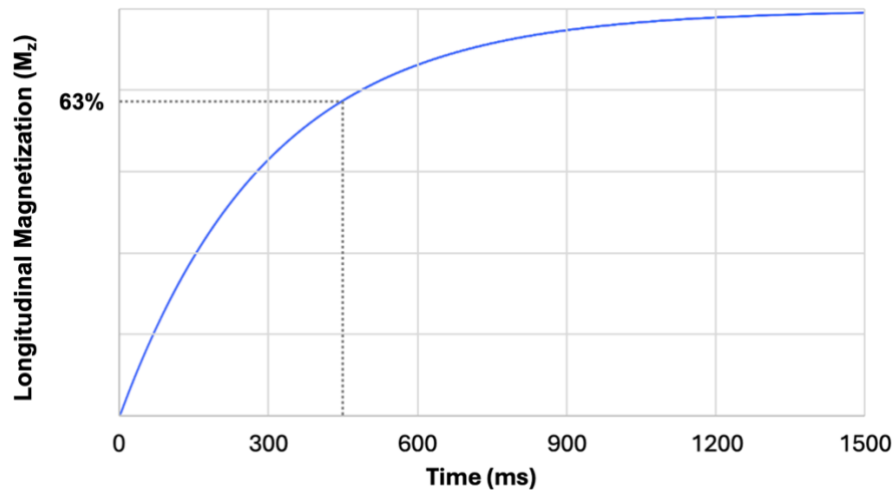
Figure 2-7 Recovery of longitudinal magnetization (M_z) with T1= 450 ms.
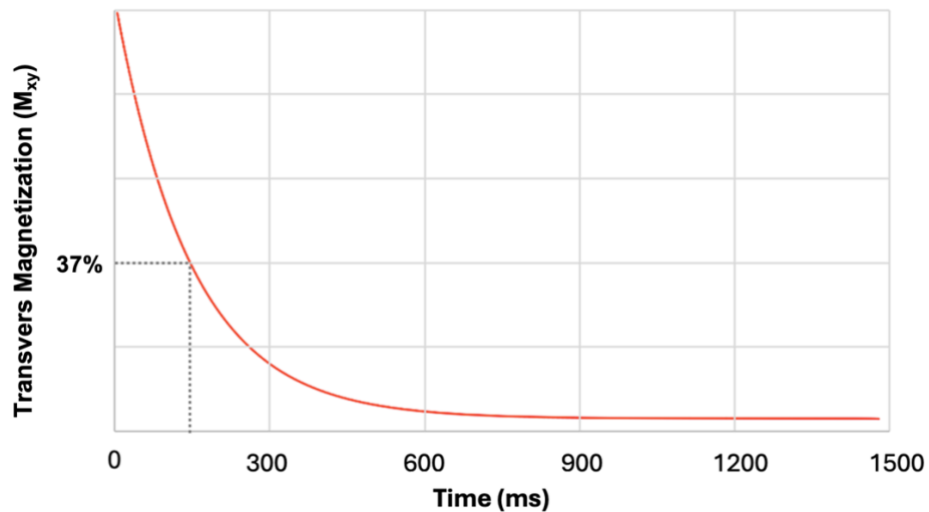
Figure 2-8 Decay of transverse magnetization (M_{xy}) with T2= 150 ms.

Differences between the time of T1 and T2 can result from the particular chemical/molecular conditions within the specific tissues in which the hydrogen atoms are contained, a characteristic that enables MRI's soft-tissue contrast

feature. Hydrogen protons in water are highly mobile, leading to longer T1 and T2 relaxation times. In fats, hydrogen protons are less mobile and have shorter T1 and T2 relaxation times. These differences are exploited to produce images with different contrasts. In cortical bone, the protons are tightly bound and largely immobile, resulting in very short T2 relaxation times and hypointense signals (84, 85). Meanwhile, air lacks mobile protons altogether, leading to a complete absence of signal in MRI.

It has previously been shown that dephasing in the transverse plane is influenced not only by true T2 relaxation, but also by inhomogeneities in the MRI system. Free induction decay (FID) is the signal observed immediately after an RF pulse is applied. An echo is formed by using specific pulse sequences that refocus dephased spins, such as spin echo (SE), which uses a 180° RF pulse see (Figure 2-9).
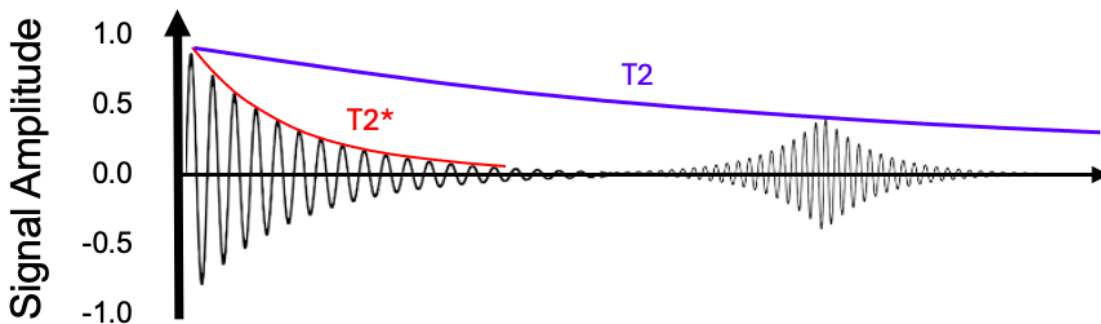
Figure 2-9 MRI Signal decay and echo formation.

MRI is vital for treatment planning in head and neck cancers as it provides precise tumour delineation, identifies critical structures (e.g., nerves, vessels), and evaluates the extent of tumour invasion into soft tissues, bones, or nerves. It aids in defining radiation therapy margins and optimizing surgical approaches by mapping tumour boundaries and involvement with surrounding anatomy (86). An MRI sequence is a specific protocol or set of parameters used during MRI to

obtain images involving RF pulses, gradient magnetic fields, echo time (TE), and repetition time (TR). The sequence determines the timing of signal measurement after the RF excitation pulse ends and magnetizations relax. The TE is the interval between the generation of transverse magnetization and the peak of the echo signal, which is when the signal is actually measured. Similarly, the TR is the duration between excitation RF pulses, as specified by the MRI sequence. By adjusting these times, the sequence can alter signal differences from tissues with varying relaxation rates, thereby modifying the MRI contrast. This allows for the relative intensification or suppression of the image intensities of specific tissues based on their relaxation properties (83). For example, T1-weighted sequences are optimal for assessing anatomical details, as fat appears bright, and it provides good visualization of structural anatomy. T2-weighted sequences are superior for identifying pathologies with high water content, such as tumours and inflammatory processes (87, 88).

Accurately determining the locations of the measured signal components within the body is crucial for generating images. This is achieved by using magnetic field gradients to encode spatial information into the signal. Slice selection in MRI is achieved by applying a linear gradient during the RF pulse to selectively excite a specific slice. Another gradient is applied perpendicularly to this slice so as to encode phase information. During signal acquisition, a gradient in the orthogonal direction encodes frequency information (83).

To create T1 and T2 maps, specific MRI pulse sequences are employed, such as inversion recovery for T1 and spin-echo sequences for T2. These sequences are widely regarded as the gold standard for relaxation time mapping (89). Data acquisition is followed by fitting the MRI signal intensities at different time points (inversion times for T1 and echo times for T2) to exponential models that describe

the relaxation processes. This results in a voxel-wise map, where each voxel contains a relaxation time value, thereby reflecting the tissue characteristics at that specific location.

MRI images can be affected by various artifacts, including chemical shift, which arises from small differences in resonance frequencies between different materials (90), such as fat and water in biological tissues or other compounds in phantoms. This frequency discrepancy leads to a spatial misalignment of signals, manifesting in the image as shifts or bands. Accordingly, it is essential to properly understand and manage this artifact to accurately interpret and analyse the image.

2.5.1.2 The use of MRI in Radiotherapy planning

CT/MRI Fusion in RT planning

MRI scans for RT can be combined with CT scans via alignment. Image registration for MRI-to-CT in H&N RT planning is a complex process due to differences in imaging modalities, spatial distortions, and artifacts (91). When scans are obtained via MRI and CT with the patient assuming a consistent treatment position, co-registration can be achieved by using immobilisation equipment such that the MRI is aligned with the CT via a rigid or deformable registration. Rigid registration, which aligns images based on translation and rotation, is computationally simple but cannot account for soft tissue deformation. Deformable registration allows for localized adjustments to better align soft tissues but is computationally intensive and requires rigorous validation to avoid errors. Often, rigid registration is used for initial alignment, with deformable methods fine-tuning the process for areas with significant anatomical variation (92). Resultantly, this enables the delineation of the target volumes on the MR

scan, prior to the subsequent transferal to the CT for treatment planning, as the CT remains necessary for calculating the dose (93, 94).

MRI-only RT Planning

MRI-only RT planning is where the treatment is planned only using an MRI scan with no acquisition of a CT scan (95, 96). The complexities associated with the co-registration of CT and MRI images support the argument for MRI-only treatment planning (97). The increasing availability of software tools for MRI-to-synthetic CT (sCT) conversion further enhances the MRI-only planning pathway by making it more advantageous compared to those which involve both CT and MRI (98, 99). In sCT, CT-like images are generated from MRI images. Within this technique (used in MRI-only RT planning), there is no need for a real CT scan to be used as a source of electron density information for RT planning (100). This approach enables a more efficient use of resources by eliminating the need for dual-modality scans and reducing errors associated with the co-registration process (101, 102). Specialized MRI sequences, such as ultra-short echo time (UTE) or zero echo time (ZTE), can enhance MRI-only RT planning by improving sCT generation and enabling visualization of low proton density tissues like cortical bone (103, 104).

2.5.2 Treatment delivery

Once the treatment planning process has been completed, radiation is delivered to the patient using a linac. Typically, the total radiation dose is divided into multiple smaller doses, a process known as fractionation. This approach gives healthy tissues time to recover while effectively targeting cancer cells, which have a lower ability to repair themselves (105). The accurate delivery of radiation requires the patient to be positioned identically as during their planning scan. Immobilisation devices, such as masks, can be used to ensure that the patient

remains in the same position throughout (every session of) the treatment. The initial setup is based on the marks made on the patient's skin or on the immobilisation devices during the simulation phase. Most modern linacs are equipped with imaging technology, which is used to perform a final check of the patient's position just before the radiation is delivered. Any necessary adjustments are made to align the patient precisely with the treatment plan. Before radiation delivery and after patient positioning, the record and verify (R&V) system is crucial for ensuring treatment adherence. It confirms that the linac settings align with the treatment plan, and checks the dose, field size, and orientation. The R&V system actively monitors parameters during treatment, comparing them in real-time to the plan.

The delivery of the overall dose planned for the treatment occurs via a series of 'fractions', which are generally administered on a daily basis (106). Throughout the treatment process, anatomical changes (both internal and external) can occur in the patient. These may require adjustments to the treatment plan to ensure that the radiation continues to target the cancer effectively, while sparing healthy tissue as much as possible. This adjustment process, known as ART, is possible with imaging during treatment or between fractions (107).

2.5.2.1 Imaging used in Treatment delivery

Cone Beam Computed Tomography (CBCT)

CBCT differs from traditional CT by using a cone-shaped X-ray beam instead of a fan-shaped one, and has become a standard tool for imaging directly in the treatment room. In this process, a kilovoltage (kV) X-ray source mounted on the treatment head rotates around the patient, emitting photon pulses from multiple angles. As the X-ray source revolves, these pulses pass through the patient and are captured by a detector at each angle, generating a series of 2D projection

images. These are then processed by a reconstruction algorithm to generate a detailed 3D image (108). Figure 2-10 illustrates the main constituents of a CBCT-integrated linac.
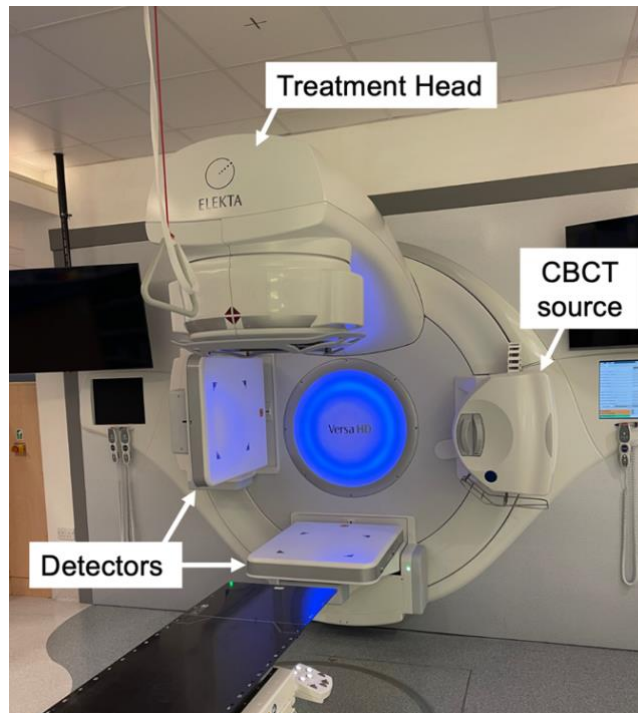
Figure 2-10 Linac equipped with CBCT positioned perpendicularly to the treatment head. The detector on the left is for CBCT detection (kV), while the detector at the bottom is used to detect megavoltage beam images directly from the treatment head.

The acquisition parameters that influence image quality include kV, which controls X-ray energy and penetration; nominal milliamps (mA) per frame, which sets the X-ray tube current; and nominal milliseconds (ms) per frame, defining the exposure time. These three parameters affect image quality and radiation dose. Collimators shape the X-ray beam, and filters refine it to enhance clarity and reduce scatter. Gantry speed controls the scan duration (109).

Although CBCT images are of a lower quality than those of fan-beams (110), this technique provides valuable information about patient positioning and anatomical changes, which can be used to determine whether the treatment plan should be

adapted (111). Key limitations of CBCT include inaccuracies, such as a lack of precision in HU due to the increased ratio of scatter to primary photon radiation (112), as well as limits to the magnitude of the reconstruction volume (113). Furthermore, repeated CBCT scans during RT increase overall radiation exposure, raising concerns over dose accumulation, particularly for patients on long treatment courses (114).

2.6 Quality Assurance (QA) in RT

The World Health Organization (WHO) (115) defines QA in RT as the set of procedures designed to ensure that the medical prescription is consistently followed and safely administered. This includes delivering the correct dose to the target area, minimising the dose to healthy tissues, reducing personnel exposure, and ensuring proper patient monitoring to evaluate the treatment outcome.

Initially, QA programmes primarily focused on dosimetry and the validation of equipment performance (116). However, they evolved to include the entire RT process, including treatment planning, patient setup and immobilisation, and treatment implementation (117). QA programmes are implemented by evaluating equipment performance against measurable parameters, with tolerances defined at specific values according to guidelines established by professional organisations, such as the IPEM and the AAPM.

Technological advances in RT, such as the incorporation of MRI for treatment planning, have further driven the need for QA protocols. Guidelines have been introduced by such professional bodies as the IPEM (16) and AAPM (17) to ensure the safe and effective use of MRI in clinical practice. Additionally, CBCT has become integral for such tasks as dose estimation and ART (118). As RT technology advances, there is an increasing need for specialised phantoms to support these evolving QA processes.

Chapter 3 Review of Anthropomorphic Multimodality (CT/MRI) Head and Neck Phantoms: Commercial Solutions and Developed In-house

Anthropomorphic phantoms are virtual or physical models that mimic the external shape and/or internal structures of the human body or its parts. Anthropomorphic phantoms have been essential from the start for enhancing accuracy and quality control in RT dosimetry (119). The increasing use of MRI in RT has led to the need for multimodality anthropomorphic phantoms, specifically for integration with both CT and MRI modalities (120).

H&N phantoms are essential due to the region's complex anatomy and frequent use of MRI in RT (121). A literature search for reviews on multimodality H&N phantoms identified three reviews, each with a different focus. Filippou and Tsoumpas (122) conducted a systematic review on the use of 3D printing for creating medical imaging phantoms across various imaging modalities, including CT and MRI, identifying four specifically designed for multimodality use in both. These phantoms were evaluated for their effectiveness in mimicking human tissues and enhancing imaging simulations. However, the review only focused on 3D-printed phantoms, excluding other types manufactured through different methods and which could also be suitable for CT/MRI.

Tino et al. (123) conducted a systematic review to explore the advances and applications of 3D-printing technologies in RT, with a particular focus on the development of 3D-printed imaging and dosimetry phantoms, whether homogeneous, heterogeneous, or anthropomorphic. Their review primarily concentrated on the broader implications of 3D printing in producing phantoms for RT. However, their review did not specifically delve into the application of

these advances in the context of anthropomorphic multimodality phantoms, such as those used in both MRI and CT.

Crasto et al. (124) conducted a systematic review of anthropomorphic brain phantoms for MRI systems, focusing on their development and utility, and highlighting their critical role in enhancing the accuracy and validation processes of MRI. Notably, the review specifically concentrated on MRI systems and brain phantoms, without covering other imaging modalities or anatomical areas.

In this review, the focus is on the physical models of anthropomorphic H&N phantoms which are claimed to be suitable for multimodal imaging, including at least CT and MRI as a minimum requirement, and can be used for either diagnostic radiology or RT purposes. It aims to describe these phantoms, detailing their manufacturing processes, uses, and limitations specifically in the context of RT.

This review adopts a narrative methodology to synthesize literature on multimodality anthropomorphic H&N phantoms. The literature search was conducted in July 2024 using Google Scholar, PubMed, and ScienceDirect with specific keywords and phrases, including "anthropomorphic phantom" and "multimodality," to identify relevant studies. Only studies published in English were considered. Studies were included if they addressed physical phantoms designed for the H&N region or the brain and if the authors stated that the phantoms were compatible with both MRI and CT. Studies focusing on other anatomical areas, virtual models, or single-modality imaging were excluded. Additionally, this review considers commercially available multimodality H&N phantoms identified through web searches on Google, using the same keywords as the academic literature search: "anthropomorphic phantom" and

"multimodality." Products were included if they met the criteria for multimodality compatibility with both CT and MRI.

Several standards must be met in the development of anthropomorphic multimodality (CT/MRI) phantoms for RT. These phantoms should ideally replicate the internal and external geometries of the targeted organ or body part. Additionally, the phantom materials must interact with radiation in the same way as human tissues do during RT. They must also possess imaging properties, including CT numbers for CT and T1 and T2 relaxation times for MRI, to ensure the realistic simulation of human tissues. Finally, the phantom must enable the precise placement of dose-measuring instruments for accurate dose verification (125).

There is a growing interest in the literature regarding the development of multimodality phantoms for the H&N region (including the brain) which are either commercially available or developed in-house by various centres and researchers. Accordingly, this review is organised into two primary sections: commercially available phantoms and non-commercially developed phantoms.

3.1 Commercially Available Phantoms

The Computerized Imaging Reference Systems, Inc. (CIRS) model 603A phantom (Norfolk, VA, USA) is an anthropomorphic skull phantom that can be imaged with CT and MRI (126) (see Figure 3-1). It is made from a plastic-based bone substitute for the skull and a proprietary signal-generating water-based polymer for the interstitial and surrounding soft tissues. The entire phantom is encased in a clear plastic shell to protect it from desiccation. Its intended use is for assessing MRI distortion in stereotactic radiosurgery (SRS) planning – a non-

invasive technique that uses a precisely-focused radiation beam commonly used to treat primary brain tumours and metastases (127). However, the phantom can also be used to verify image registration algorithms and confirm the accuracy of sCT (128). Radiation dosimeters cannot be inserted into this phantom, nor does it appear anatomically accurate to a real head (due to its absence of air cavities). Instead, a 3D grid is inserted inside the cranium to assess spatial distortion in MR images.

Photograph of the phantom   CT   MRI
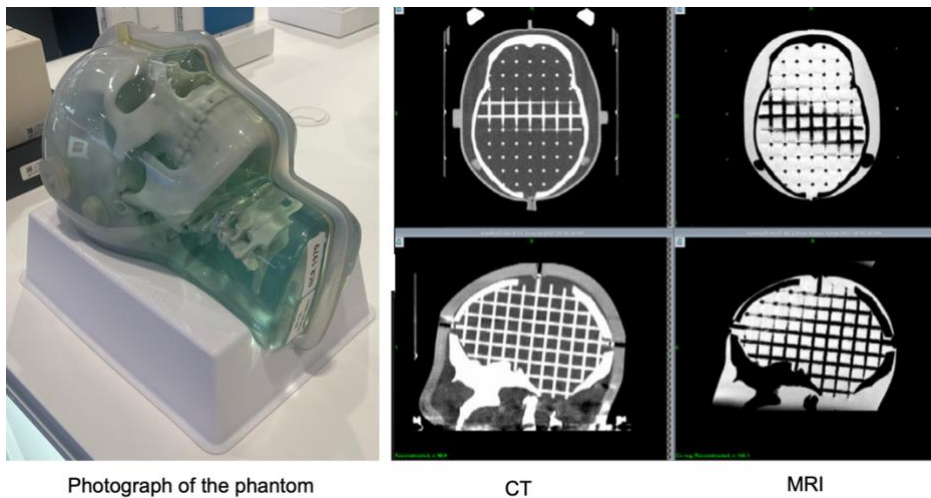
Figure 3-1. MRI and CT images of the model 603A phantom. The skull is produced from a plastic-bone tissue substitute, the soft tissues are made of a water-based polymer, and the 3D orthogonal grids are made of reinforced nylon. Reproduced from (129), under the Creative Commons CC BY license.

CIRS offers another anthropomorphic phantom used to validate the entire treatment planning and delivery process in SRS, known as the Stereotactic End-to-End Verification Phantom (STEEV) (see Figure 3-2) (130). According to the manufacturer, the phantom is made of CIRS's proprietary tissue-equivalent materials, and is compatible with MRI, CT, and Positron Emission Tomography (PET) scans, achieved through the use of various interchangeable inserts designed for each modality. The phantom supports a wide range of dosimeters for the purpose of dose verification. Although the STEEV phantom is designed for parts of the phantom, such as the brain, do not produce realistic MRI signals.
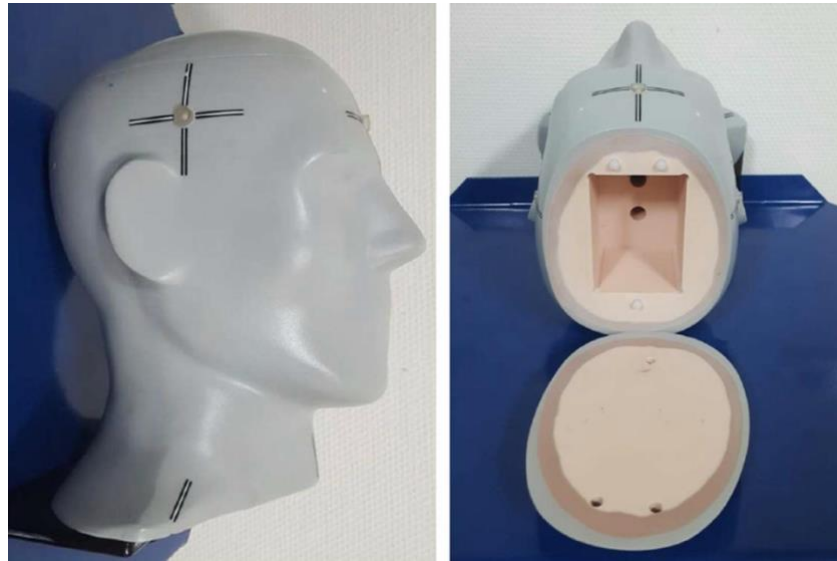
Figure 3-2 STEEV phantom A) Photograph of the phantom showing the brain without any insert. B) Sagittal CT showing ionization chambers in the brain and neck. Reproduced from (131) under the Creative Commons CC BY license.

Standard Imaging (Middleton, WI, USA) initially offered the MAX-HD (132), which has evolved into the MAX-HD 2.0 version (133) and was subsequently renamed LUCY™ MR (134) (see Figure 3-3), to verify the accuracy and safety of SRS procedures. According to the manufacturer, the phantom is fabricated from proprietary materials and can be used with MRI, CT, kV, and mega-voltage (MV) modalities, and has many tools for measuring dosage, such as ion chamber cavities and multiple film planes. The available images show the phantom's brain and soft tissues as one, unlike the clear distinction in human imaging.
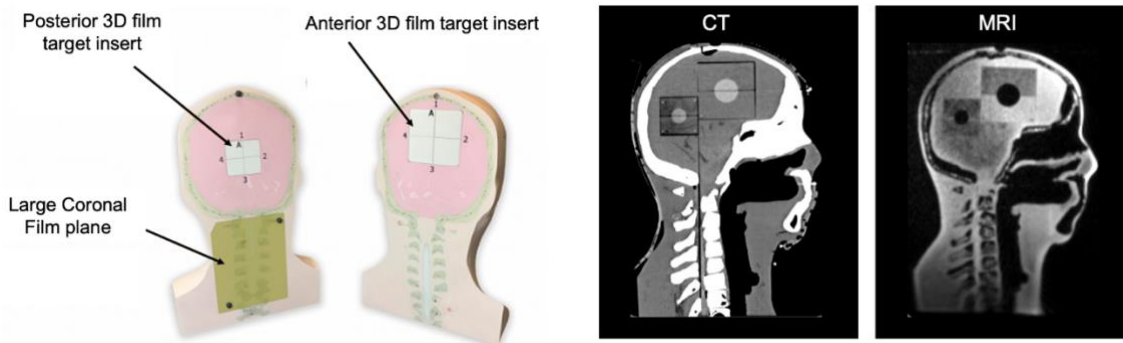
Figure 3-3 LUCY™ MR Phantom standard configuration and inserts. Reproduced with permission from Standard Imaging (133).

RTsafe (Artotinis, Greece) developed a Prime head phantom using 3D printing technology (135), where the bone structure and external contour of a patient's head are printed using a calcium-based raw material. Due to the fragility of the printing material, two layers of epoxy infiltrant are added to increase protection and physical density (136). Different inserts can be used, such as an ionisation chamber, films, and 3D polymer gel, and the phantom is filled with water as a soft tissue substitute (see Figure 3-4). This phantom can be imaged using MRI and CT scans for the end-to-end testing of SRS applications (135). The phantom is limited to the head region. While its external shape is anthropomorphic, its internal structure lacks such features, as it does not include air spaces or such detailed anatomical structures as vertebrae.
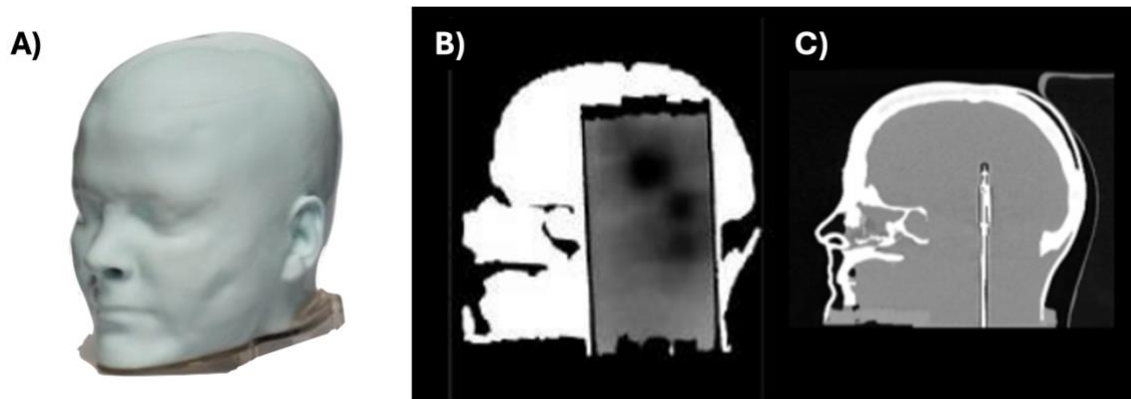
Figure 3-4 Prime head phantom. A) Image of the phantom, B) Sagittal MRI image of the phantom incorporating the gel dosimetry insert, and C) Sagittal CT image of the phantom incorporating the ion chamber insert. Reproduced with permission from RT Safe (135)

3.2 Non-commercial phantoms

Chen et al. (137) created a deformable brain phantom similar to the human brain in terms of both anatomy and mechanical properties (see Figure 3-5). This phantom can be used to evaluate image-processing techniques, such as segmentation, reconstruction, and registration in each modality (CT, MRI, and ultrasound). They selected polyvinyl alcohol cryogel (PVA-c) for use in its construction. To determine the best PVA-c formula for preparing its material, they prepared 12 samples using a range of Polyvinyl alcohol (PVA) solution concentrations and freeze-thaw cycles (FTCs). Once done, they asked a neurosurgeon to select the sample with the most similar texture to brain tissue. They decided to use 6% PVA with 1 FTC. After performing a number of tests, they found that concentrations of 2% BaSO4, 0.025% Copper(II) sulfate (CuSO4), and 1% talcum added to the PVA created effective contrasts for CT, MRI, and ultrasound, respectively, and suitable for making a single phantom multimodal. They used 3D printing to create anatomically-accurate moulds for the brain structure, which they fabricated using Tango Plus Polyjet Resin that could be filled with PVA-c. The phantom has inserts that are spherical markers made

with 8% PVA solution with 2 FTC, and is used to help in the registration of the images and a tumour made of a 4% PVA solution with 1 FTC (see Figure 3-6). They added an inflatable catheter in the phantom to cause a brain shift when inflated, similar to the results of gravity and brain swelling on the human brain. However, this phantom is not suitable for RT due to its non-anthropomorphic external appearance and inability to measure radiation dose or incorporate dosimeters.
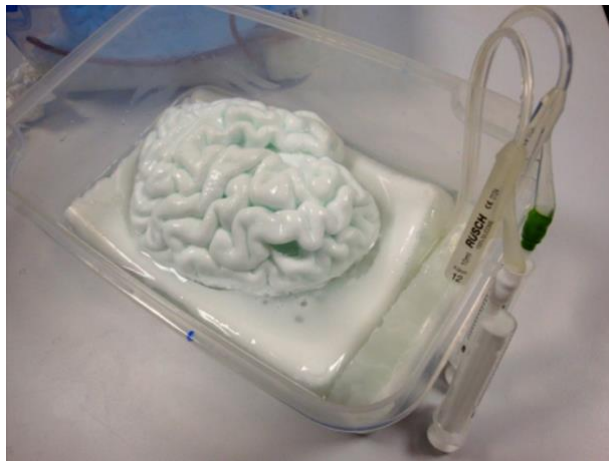
Figure 3-5. PVA-c Phantom. Reproduced with permission from Wiley publication (137).
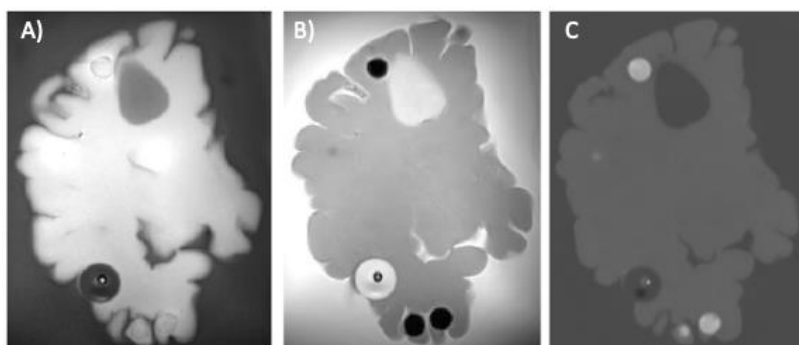
Figure 3-6. Selected images of the PVA-c phantom. A) MR T1-weighted image (B), MR T2-weighted image (C) CT image. Reproduced with permission from Wiley publication (137).

Gallas et al. (138) developed an anthropomorphic multimodal (CT/MRI) head phantom for end-to-end RT tests. This phantom is head-shaped with four

compartments, and it was 3D-printed using epoxy resin material (see Figure 3-7). The phantom's outer shape is based on CT data from a human, and contains a nasal cavity and solid chin part. The phantom's inner part consists of refillable cylindrical compartments. In terms of surrogates, the authors used a dipotassium phosphate-based material for bone (Compartment A), an agarose gel-based material for the brain (Compartment B), and distilled water for cerebrospinal fluid (compartment C). One of the compartments was filled with gel for dosimetry (compartment D). They used the phantoms for CT treatment planning and proton irradiation. However, the authors also obtained MRI images for the phantom to assess the similarity between the materials used and human tissues, as well as to compare the polymerisation gel dosimetry before and after irradiation. The authors acknowledged that their material for the bone surrogate was not suitable, as it gave a high signal in MRI images from containing water. Moreover, this phantom is not internally anthropomorphic, as it consists of simplified cylindrical compartments rather than the complex anatomical structures found in a human head.
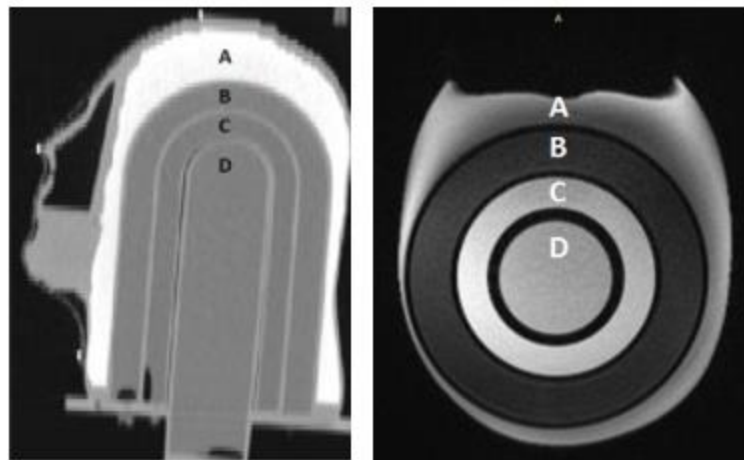
Figure 3-7 - Head phantom, A) Cranial bone surrogate, B) Brain tissue surrogate, C) Cerebrospinal fluid surrogate, D) Polymerization gel dosimeter. Reproduced with permission from Elsevier (138).

Soliman et al. (139) used a real human skull (provided by Osta International, White Rock, BC, Canada) to assess the ability to detect bone using ultra-short echo-time (UTE) MRI sequences, which can determine the appropriate acquisition parameters for the bone and develop an approach to generate sCT (see Figure 3-8). The skull was placed in a 3D-printed acrylic container, which was filled with a mixture of gadolinium chloride hexahydrate and powdered milk dissolved in deionised water to represent the average properties between white and grey matter. They obtained images of the phantom using CT and MRI scanners, after which they generated sCT using MRI data and compared them to real CT images. While the use of human bone can guarantee accurate results, its use remains legally and ethically complex, varying by location and situation. Additionally, the manufacturing cost is very high, and real bone degrades over time.
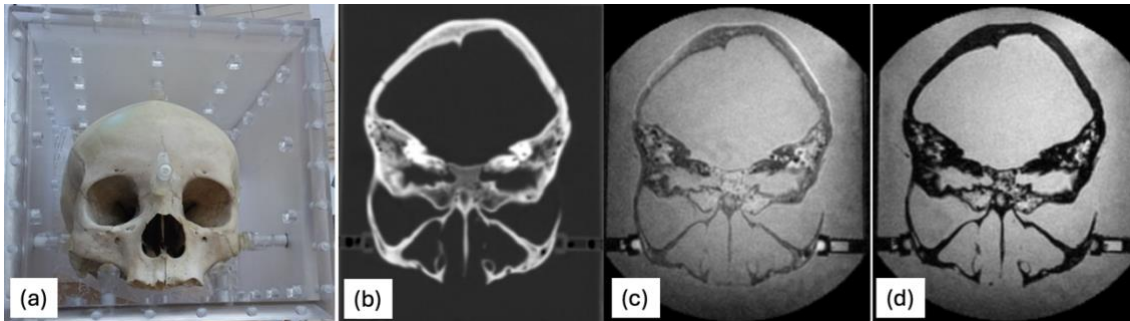
Figure 3-8 a) The human skull is held steady inside the container with posts filled with water. B) CT image, c) and d) first and second echoes of UTE, respectively. Reproduced with permission from Wiley publication (139).

Steinmann et al. (140) developed an anthropomorphic H&N phantom that could be imaged with MRI and CT to evaluate the safety and usefulness of magnetic resonance-guided radiotherapy (MRgRT) systems through multicentre studies. The phantom is a commercially available acrylic shell shaped like a human head (The Phantom Laboratory, Salem, New York, USA) that can be filled with water

and contains a concavity for a custom insert. This insert contains primary and secondary PTVs made of a synthetic clear ballistic gel and an OAR represented by an acrylic cylindrical spinal cord-like structure (see Figure 3-9). These structures are surrounded by melted Superflab, which is a plastic material used as a tissue equivalent bolus in the clinic. The insert contains Radiochromic EBT3 film to measure the dose distribution and thermoluminescent detectors to measure absolute dose. The phantom was imaged using a CT and different MRgRT systems to evaluate the use and contrast of the materials employed (see Figure 3-10). The authors conducted two types of tests: a reproducibility study and a feasibility study. In the former, the same treatment plan was delivered multiple times on one MRgRT system on the same day. The phantom was sent to three different institutions for the feasibility study. In both studies, end-to-end tests were performed using radiation dosimeters, and the differences were evaluated. This phantom lacks bones and air cavities, and its design is limited solely to the head.
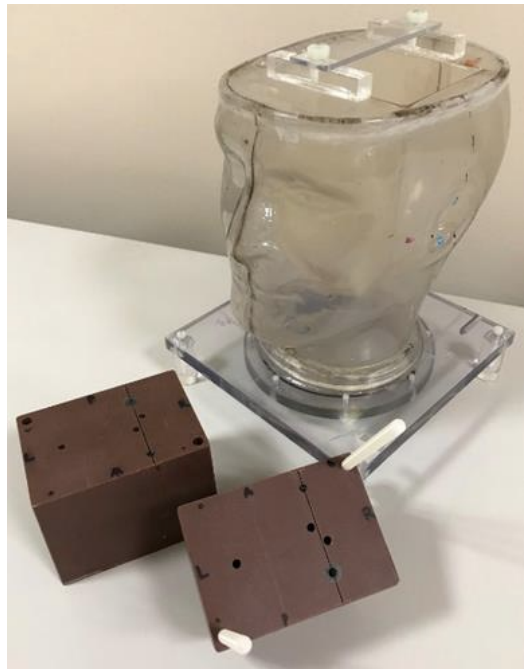
Figure 3-9. Image of a water-fillable anthropomorphic shell of the H&N phantom and the two-piece insert. Reproduced with permission from Wiley publication (140).
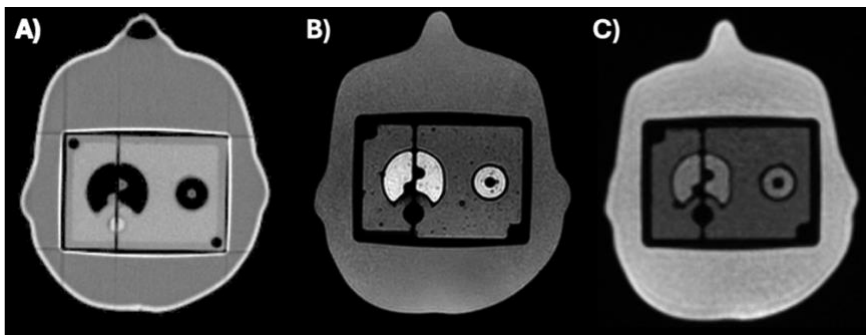
Figure 3-10. H&N phantom, A) Axial CT image, B) Axial MRI image scanned on Unity system's 1.5 T MRI system with a T1 sequence, C) Axial MRI image scanned on MRIdian Linac 0.35 T system with a True fast imaging with steady-state free precession (TrueFISP) sequence. Reproduced with permission from Wiley publication (140).

De Deene et al. (141) developed anthropomorphic H&N phantom designed for multimodality medical imaging, including MRI, CT, PET, and ultrasound (see Figure 3-11). It emulates blood flow and perfusion using a porous silicone elastomer brain compartment, fabricated through a cast-moulding-dissolution technique. The skull and cervical vertebrae are made from a mix of 3D printing and cast-moulding, with materials mimicking human tissue density. Specifically, skin is replicated with water-clear flexible polyurethane, blood vessels with off-

the-shelf silicone tubing, the skull and cervical vertebra with a mixture of polyurethane and calcium carbonate, and muscle and connective tissue with gelatin hydrogel. This phantom serves educational and research purposes, facilitating the optimisation and validation of medical imaging techniques and protocols.
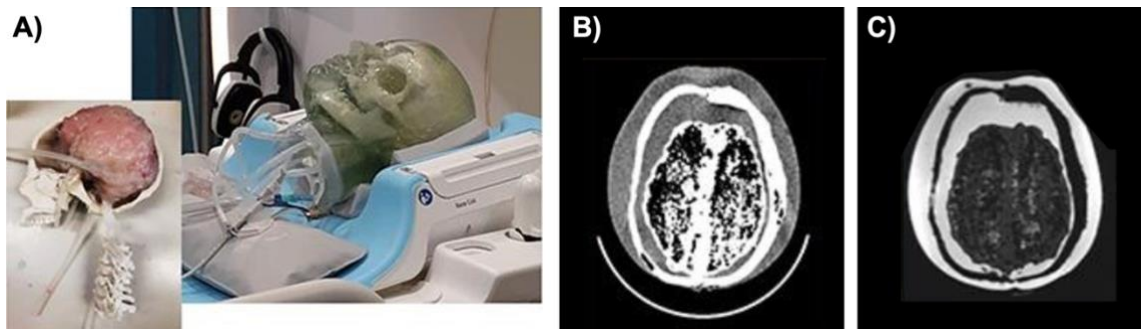
Figure 3-11 A) Photograph of the phantom. B) CT, and C) MRI images. Reproduced with permission from Elsevier (141).

The anthropomorphic multimodal H&N phantom, developed through a collaboration between the University of Leeds, Leeds Test Objects (LTO) Ltd. (Boroughbridge, UK), and the Leeds Teaching Hospitals NHS Trust (LTHT), is designed for use in RT (13) (Figure 3-12). Its design is based on an anonymised CT scan of a typical H&N patient treated at the LTHT. Such structures as bone, air cavities, and the brain were delineated using the Oncentra Masterplan treatment planning system (Elekta AB, Stockholm, Sweden). The resulting structure files were converted into stereolithography (STL) format for 3D printing by first converting them into separate NIfTI files for each structure using Smilx (Australian e-Health Research Centre, CSIRO, ITK version 4.7.0), followed by generating surface meshes with ITK-SNAP software (version 3.6.0, www.itksnap.org).

The phantom's outer shell is 3D printed using a photopolymer, and bone anatomy is printed using a ceramic material. The outer shell includes dedicated compartments for soft tissue and the brain. The soft tissue compartment is filled with deionised water, while the brain compartment, formed using a mould, contains a 10% PVA-c prepared through four FTCs and immersed in deionised water. Furthermore, the phantom's design incorporates a hole within the cranium region to accommodate a semiflex ionisation chamber for the measurement of radiation dose. The lungs are represented by a low-density polyurethane material. This phantom was the one used in Chapter 5 and Chapter 6.
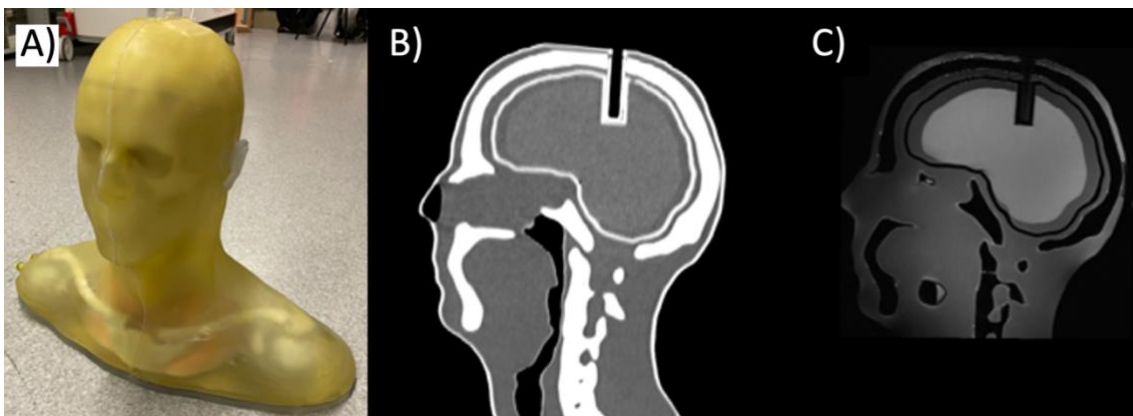
Figure 3-12 H&N anthropomorphic phantom. A) Photograph of the phantom. B) Sagittal CT and C) Sagittal T2-FLAIR (fluid-attenuated inversion recovery). At the top of the head, a recess was designed to allow the placement of a dosimeter.

Table 3-1 offers a brief comparison of the phantoms identified in the chapter, evaluating their replication of patient geometry, material properties for imaging and RT, suitability for RT through dose measurement capabilities, and stability over time or after radiation.

Table 3-1 Comparative Summary of H&N Phantoms. All reported T1 and T2 relaxation times were measured at 3T.

Phantom	Replication of patient geometry		Material properties						fits dosimeters	Stability
	Internal	External	Tissue	For imaging			For RT			
				T1 (ms)	T2 (ms)	CT (HU)	Mass density (g/cm³)	Relative electron density		
The CIRS Model 603A	Partially (includes non-human grid)	Yes		Not reported					No	Not Studied
STEEV	Yes	Yes	Cortical bone	Not reported	Not reported	Not reported	1.782	1.93	Yes	Not Studied
			Trabecular bone				1.156	1.20		
			Soft tissue				1.027	1.06		
			Brain				1.038	1.07		
			Spinal cord				1.043	1.07		
LUCY™ MR	Yes	Yes		Not reported					Yes	Not Studied
Prime	Yes	Yes		Not reported					Yes	Not Studied
Chen et al.	Yes	No		Not reported					No	Not Studied
Gallas et al.	No	Non-anthropomorphic, but includes nasal cavity and chin	Bone	Not reported	Not reported	978	1.308	1.53	Yes	Not Studied
			Brain	Not reported	Not reported	24	0.958	0.96		
			Tumour	Not reported		41	1.021	1.05		
Soliman et al.	Yes	No	Brain	1,805 ±51	96 ±1		Not reported		No	Stable within 28 days
Steinmann et al.	No (Basic shapes and no bone)	Yes		Not reported					Yes	Not Studied
De Deene et al.	Yes	Yes		Not reported					No	Not Studied
Johnstone (Leeds Anthropomorphic H&N phantom)	Yes	Yes	Brain	1,387 ±6	139 ±4	32 ±10	Not reported		Yes	Not Studied
			bone	N/A	N/A	457 ±42				
			Soft tissue	3350 ±9	1395	-2.9 ±1.5				
			Lung	N/A	N/A	-765 ±0.8				

3.3 Discussion

This review seeks to assess the available anthropomorphic multimodality (CT/MRI) H&N phantoms, focusing on their fabrication methods, applications, and potential utility in RT, and includes literature published up to July 2024. The phantoms identified in the literature can be categorised into two groups: commercially available and in-house manufactured.

Generally, the fabrication methods for commercial phantoms are not fully detailed, except for the Prime head phantom, which is explicitly stated to be 3D printed (135). For the majority of non-commercial phantoms, 3D printing appears to play a crucial role. For example, Chen et al. (137), Gallas et al. (138) and De Deene et al (141) used 3D printing to create the moulds and structural components necessary for developing their phantoms. Soliman et al. (139) used 3D printing to produce a plastic container designed to hold and stabilise a human skull, while Johnstone (13) employed the technology to produce the phantom's outer shell and bone anatomy. The rise of 3D-printing technology in the production of these phantoms is notable, likely due to its precision and flexibility in replicating human body parts and its potential to lower costs (142-144).

All four commercial phantoms were specifically designed for SRS applications. The CIRS model 603A is used primarily for MRI image distortion assessment in SRS, while the other three serve to support comprehensive end-to-end QA, enabling dose measurement with at least two methods, such as gel dosimetry, film, or ionisation chambers. This may be because SRS requires more stringent QA, given its reliance on delivering highly-precise radiation in a limited number of sessions (145).

On the other hand, not all in-house manufactured phantoms are designed for RT. Only three are used for end-to-end tests, incorporating the ability to accommodate radiation dosimeters. The dose measurement methods in these phantoms vary: Gallas et al.'s phantom uses gel dosimetry (138), whereas Steinmann et al.'s phantom incorporates thermoluminescent detectors (TLDs) and radiochromic film (EBT3) (140), and Johnstone's phantom is equipped to house a semifelx ionization chamber (13). Other in-house phantoms serve different purposes and are not suitable for RT due to their lack of realistic human simulation and inability to accommodate radiation dosimeters. For example, Chen et al.'s phantom (137) validates image processing for multimodal imaging. Soliman et al.'s phantom (139) certifies the use of sCT of cortical bone from MRI, while De Deene et al.'s phantom (141) supports education and research in optimising imaging techniques and protocols.

While most phantoms, whether commercial or in-house, are designed to be compatible with MRI and CT, many do not accurately replicate the quantitative imaging properties of biological tissues or have not been thoroughly validated to do so. To accurately replicate the imaging properties of specific human tissues, it is crucial that the materials used exhibit CT numbers, as well as T1 and T2 relaxation times, that closely match those of actual human tissues. Indeed, discrepancies could arise from failing to properly mimic these properties, potentially resulting in inaccurate QA test outcomes. Phantoms that fully meet RT requirements are rare due to such challenges as the inability to replicate patient geometry internally or externally, or accurately measure radiation doses in desired locations.

Moreover, there is limited evidence on the stability of these phantom materials over their expected lifespans and after repeated radiation exposure. If these

materials change, it could affect the interpretation of results. Variations in material properties might be mistaken for changes in the performance of imaging or RT devices, potentially leading to inaccurate assessments.

All anthropomorphic multimodality H&N phantoms developed for RT have primarily been used for end-to-end QA (138, 139, 146, 147) with their potential for broader MRI QA for RT having been left largely unexplored. This presents an opportunity for further research to expand their use across additional domains and enhance their utility in RT.

Chapter 4 Assessing suitability and stability of materials for a head and neck anthropomorphic multimodality (MRI/CT) phantoms for radiotherapy

4.1 Introduction

Recently, there has been an increased focus on the development of anthropomorphic phantoms for RT purposes (120). These phantoms, designed to mimic human anatomy with tissue-mimicking materials (TMMs), provide a ground truth for developing and validating new imaging and treatment techniques (148). They are crucial for end-to-end RT testing, encompassing all stages from simulation to actual delivery (149). Furthermore they play a key role in QA by enabling realistic, patient-specific testing scenarios to ensure treatment efficacy and safety (150).

In the field of RT, CT serves as a basis for treatment planning, owing to its widespread availability, capability to provide essential electron or mass density information required for accurate dose calculations, and inherent lack of geometric distortions (151, 152). However, recent advances in MRI have led to its increased adoption in RT settings, primarily due to its superior soft tissue contrast allowing for greater accuracy in tumour and healthy tissue delineation (94, 152). In order to utilise the strengths of MRI for RT treatment planning, traditionally it must be registered to CT and there has been a growing trend to do this (9, 153, 154). This trend has necessitated the development of MRI/CT multimodal phantoms, which play a crucial role in optimising and validating RT pathways (138, 155-157).

Creating an anthropomorphic multimodality phantom for MRI and CT requires TMMs with imaging properties similar to human tissues. Litt and Brody (158)

highlighted the challenge of finding materials that produce adequate signal intensity in both CT and MRI. One practical solution involved the use of adaptable phantoms designed to be filled with different materials suitable for each modality (159, 160), however this is not optimal for clinical use due to the complex and time-consuming setup.

More recently three-dimensional (3D) printing technology has been applied to the construction of phantoms (123). Despite its potential, a systematic review (122) highlighted significant limitations in the range of available 3D printing materials and their ability to simulate all necessary tissues for various imaging modalities. Alternatively, 3D printed moulds, allow use of a wider array of materials than those that can be printed directly (161).

The TMMs used for anthropomorphic multimodality (MRI/CT) phantoms for RT are required to interact with X-rays similarly to human tissues and generate comparable MRI signals. The stability of TMMs over time and after exposure to high radiation levels from linear accelerator (linac) use is essential for clinical consistency. Material properties can change over time due to environmental conditions, such as temperature and humidity changes, and biological factors, such as bacterial growth (162). Radiation can affect materials through ionization (163). Furthermore, phantoms should avoid the use of toxic substances for safety (164) and ideally be storable at room temperature for ease of use.

Biopolymers, such as polysaccharides, carrageenan, agar, agarose, and gelatin (165), are commonly used in phantom production due to their tissue-like properties from high water content. However, they exhibit limited stability over time, suffering from issues such as water evaporation and bacterial growth (166-168), and their imaging properties can vary between batches, complicating

standardization. In contrast, synthetic polymers are highly standardized (14) and demonstrate greater stability over time.

Polyvinyl alcohol cryogel (PVA-c) is a synthetic polymer hydrogel used to develop MRI and ultrasound phantoms (169, 170). The MRI properties of PVA-c can be modified by changing the PVA concentration (170) or the number of freeze-thaw cycles (FTCs) used in production (169). An early MRI study (171), identified issues with PVA-c's long-term stability, noting a decrease in T1 and T2 relaxation times over six months. This study did not determine the cause of the degradation, though the material was sealed to prevent water evaporation, suggesting other factors like bacterial growth might have contributed.

Taghizadeh et al. (172) found that the acoustic properties of a PVA-c phantom for ultrasonic purposes were stable over a year when immersed in distilled water without additives or refrigeration. However, this study did not evaluate the MRI and CT image property stability. Yee et al. (173) explored PVA slime phantoms for MRI phantoms, examining their T1 and T2 characteristics with varying gadolinium oxide concentrations, emphasizing the need for further studies on the long-term stability of these PVA-based phantoms.

Some other synthetic materials show promise for the development of multimodal phantoms. Hellerbach et al. (14) and Steinmann et al. (15) identified synthetic materials capable of mimicking tissue in MRI, CT, or both. However, many of these have only been evaluated in a single imaging modality, and their imaging properties over time and after-radiation exposure remain unexamined.

This study aims to bridge these knowledge gaps by exploring materials identified in the literature as potential substitutes for human tissues in the H&N region for multimodal (CT/MRI) phantoms. The suitability was determined by measuring

imaging properties, specifically CT numbers, T1, and T2 relaxation times, and comparing these to the human tissues they are intended to simulate. Additionally, the stability of these materials was assessed over time and after radiation exposure. These insights into imaging properties and stability provide practical solutions for improving multimodal phantom design for RT.

4.2 Methods

4.2.1 Samples Preparation

Potential candidate materials suitable for MRI and CT phantoms were identified through a literature search, see Table 4-1. This process included searching scientific databases such as Google Scholar, PubMed, and ScienceDirect using keywords and phrases such as "computed tomography," "CT," "magnetic resonance imaging," "MRI," "phantom," and "material." Relevant articles were screened by reviewing titles and abstracts, followed by a detailed assessment of full texts to extract information on material properties, as well as imaging performance in both modalities. Candidate materials were prepared in 5 mL test tubes as described below. Six test tubes of each material were prepared simultaneously in a single batch. One was used to evaluate the stability over time, and the remaining five used to measure stability after radiation exposure. Each material was assigned a unique number in Table 4-1 that is used throughout this chapter.

Table 4-1 candidate materials that are potential suitable for MRI/CT phantoms with assigned unique material numbers.

Material Type	material number	Material Name	Reference
synthetic polymer	1	10% PVA-c	(13)
	2	12.6% PVA-c	
	3	14.3% PVA-c	
Plastic	4	Extra soft	(15)
	5	75% Extra soft and 25% Softener mix	
	6	90% Extra soft and 10% Softener mix	
	7	Super Stuff (TX-151)	
Synthetic Gelatin	8	Gel 1	
	9	Gel 2	
	10	Gel 3	
	11	Gel 4	
	12	Gel 5	
Silicone	13	Dragon Skin™ 10 medium	
	14	Dragon Skin™ 30	
	15	Dragon Skin™ FX-Pro	
	16	Ecoflex™ 00-10	
	17	Ecoflex™ 00-30	
	18	Ecoflex™ 00-50	
	19	PlatSil® Gel-OO	
	20	PlatSil® Gel-OO30	
Synthetic gel	21	Carbopol 980 polymer	(14)
	22	Carbopol EZ-3 polymer	
	23	Carbopol EZ-4 polymer	

For PVA-c samples, materials 1-3, 40 g, 52 g, and 60 g of PVA powder (Sigma-Aldrich, Merck KGaA, Darmstadt, Germany) were mixed with 360 g of deionised water and 0.1 g of the preservative benzalkonium chloride in an Erlenmeyer flask to achieve PVA concentrations of 10%, 12.6%, and 14.3% by weight, respectively. Mixtures were stirred for 15 minutes using a magnetic stir plate and then autoclaved at 121°C for 30 minutes to ensure complete dissolution of the PVA powder. After autoclaving, the solution was stirred using a magnetic stir plate for 30 minutes at room temperature to ensure uniform gel formation. The

homogeneous solution was poured into large moulds and sealed to set at room temperature for 12 hours. The gel underwent four FTCs, each consisting of 24 hours of freezing at -20°C followed by 12 hours of thawing at room temperature. Finally, the gel was sectioned into appropriate sizes using a scalpel and placed in a test tube completely covered with water to prevent air contact.

The extra soft and softener plastics (Bright Baits, Lotenhullestraat, Belgium; materials 4-6) come in liquid form and emulsify when heated, curing rapidly at room temperature. To produce extra soft plastic (Material 4), 50 g of the liquid was poured into a heat-resistant glass measuring cup and heated on a hot plate to 170°C until it reached a thick, transparent consistency approximately 5 minutes). Then, it was poured directly into a 5 mL test tube and left at uncovered at room temperature to cool for 30 min and then the tubes were sealed.

The other two plastic mixtures (Materials 5 and 6) were formulated by adding extra soft plastic to the softener before heating. Material 5 was made by mixing 75 g of extra soft with 25 g of softener. While material 6 was made by mixing 90 g of extra soft with 10 g of softener. Mixing was performed manually with a spoon for 1 min. Each mixture was poured into a separate cup and heated until it reached the desired consistency. Then, they were poured directly into 5 mL test tubes and left at uncovered to cool at room temperature for 30 min before sealing the tubes.

Super Stuff (TX-151) bolus material (Radiation Products Design, Inc., Albertville, MN; material 7) is a gelling agent that comes as a powder and comprises gum guar and inorganic borates (174). The Super Stuff powder was mixed with deionised water as per the manufacturer's instructions and cured in a test tube at room temperature for 10 min before sealing.

Synthetic oil-based gels (Humimic Medical, South Carolina USA; materials 8-12) are commonly used for medical training as they mimic the mechanical properties of human tissue. These gels combine oils and gellants in various proportions ranging between 75-95% oil (175) and the manufacturer states each of these simulates different human tissue (176). All gels were heated to 170°C for 5 min on a hot plate, poured into test tubes and left uncovered to cool at room temperature for 30 minutes before sealing.

The silicone-based material, 13-18 (177) (Smooth-On Inc., Easton, PA, USA) and 19-20 (178) (Mouldlife Ltd., UK) comes in liquid parts A and B. Each material was prepared by manually mixing Parts A and B in a 1:1 ratio by mass, poured into test tubes and sealed before leaving to cure.

The synthetic gels (Lubrizol Corporation, USA; materials 21-23) are Carbopol polymers that come in powder form that when exposed to a pH range of 4.0 to 6.0 become a gel (179). Powders were dissolved in deionising water for 5 minutes using a magnetic stir plate, resulting solutions were neutralised with a sodium hydroxide solution to adjust the pH. The resultant gel was then placed in the test tubes and sealed.

4.2.2 Material evaluation

4.2.2.1 Assessing the similarity of candidate materials to real human tissue

A cylindrical acrylic tank with dimensions of 7.5 cm in height and 21.5 cm in diameter was fabricated to accommodate all test tubes containing the materials during CT and MRI scans. The tank was designed to be filled with water, a critical requirement for MRI to ensure proper coil loading, and for CT to establish appropriate scattering conditions. To monitor the temperature during each

experimental session, a liquid crystal strip thermometer was affixed to the exterior surface of the tank (Figure 4-1).
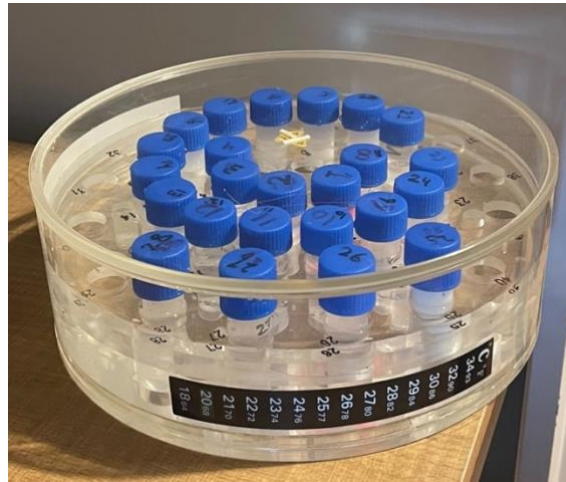
Figure 4-1 Water tank of samples with the thermometer strip.

Test tubes from all candidate materials were positioned in the acrylic tank filled with water and then imaged using MRI and CT. Measured properties were compared to literature values for human H&N tissues (Table 4-2). Tissue T1 and T2 ranges were taken from reported T1 and T2 measurements that used inversion recovery (IR) and spin echo (SE) sequences respectively (180).

Table 4-2 Computed tomography (CT) number and magnetic resonance imaging relaxation times at 3T for healthy human tissue in the head and neck region (180-182).

Tissue	T1 relaxation time (ms)	T2 relaxation time (ms)	CT (HU)
Cancellous bone	513 to 659	40 to 160	300 to 400
Brain white matter	295 to 992	59 to 78	20 to 30
Brain grey matter	1052 to 1764	79 to 120	30 to 40
Fat	291 to 476	41 to 154	−30 to −70
Muscle	865 to 1659	27 to 43	20 to 40

T1 and T2 were measured using a 3T Siemens Prisma MRI scanner (Siemens Healthineers, Erlangen, Germany). The tank was placed on the MRI table, both the spine coil underneath and the 18-channel body coil placed on the tank were used. 3D inversion recovery (IR) and 2D spin echo (SE) multi-contrast sequences for their well-established ability to accurately measure T1 and T2 relaxation times, respectively (89) and were produced using an in-house developed MATLAB code (MathWorks, Natick, MA, USA) by a clinical medical scientist specialising in MRI. The T1 and T2 maps were reconstructed on a voxel-by-voxel basis. The algorithms are designed to optimise the data used for mapping, including avoiding regions with very low signals close to the noise level. Moreover, the T2 fitting software uses an algorithm to exclude longer TE data from shorter T2 voxels to avoid noise bias (183). Equation 4-1 was fitted to the signal intensities at various inversion times to create T1 maps, whereas Equation 4-2 was fitted to the signal intensities at various TE values to develop T2 maps. Signal intensity (SI) values were measured experimentally at various TIs for T1 mapping and TEs for T2 mapping. T1 and T2 were fitted as the unknown relaxation times, and S0 the fully relaxed signal, was also fitted in both equations as a scaling factor. In Equation 4-1, the inversion pulse flip angle (Θ) was fitted to account for imperfections in the inversion process and B1 inhomogeneities. The TR in Equation 4-1 was fixed at 3000 ms as a scanner-controlled parameter. TI and TE were experimental parameters, varied during acquisition to generate data for T1 and T2 mapping, with their values chosen to cover a broad range of expected relaxation times.

$$SI(TI) = S0\left(1 - (1 - cos(\Theta))exp\left(-\frac{TI}{T1}\right) + exp\left(-\frac{TR}{T1}\right)\right)$$ **Equation 4-1**

$$SI(TE) = S0\left(exp\left(-\frac{TE}{T2}\right)\right)$$ **Equation 4-2**

SI = signal intensity

S0 = fully relaxed signal

Θ = inversion pulse flip angle

TE = echo time,

TR = repetition time, and

TI = inversion time.

The image acquisition parameters for the IR sequence were repetition time (TR) = 3000 ms, echo time (TE) = 1.53 ms; inversion times = 83, 400, 1500 and 2890 ms; Flip Angle = 8°; field of view (FOV) = 224×216 mm; voxel size = 1×1×2 mm, 36 slices. For the SE multi-contrast sequence, the image acquisition parameters were TR = 6030 ms, TE = (32 TEs equally spaced from 12.4 to 396.8 ms), FOV = 224 × 224 mm, voxel size = 0.875×0.875×2 mm, 10 slices.

Hounsfield units (HU) were measured on a CT scan acquired using a Philips Brilliance BigBore CT simulator (Philips Medical Systems, Best, Netherlands) with the following settings: 120 kV, 104 milliampere-seconds (mAs), in-plane resolution = 1.17×1.17 mm, slice thickness = 2 mm, FOV = 600×600 mm, 142 slices.

T1 and T2 maps and CT images were analysed using 3D slicer (v4.5.0; 3D Slicer contributors; www.slicer.org). Region of interest (ROI) were contoured for each sample and mean and standard deviation (SD) calculated for each. All ROIs were cylindrical and clipped by 3 voxels from the test tube walls to avoid partial volume effects and were visually assessed and modified where necessary to remove

regions of chemical shift artefact (i.e. where signal from the water tank overlapped the sample).

Chemical shift arises in MRI due to variations in local magnetic fields caused by differences in electron density around protons. This shifts the resonant frequency of protons in materials like fat or silicon relative to water, resulting in spatial displacement (90), particularly evident at lower bandwidths (184). When developing a phantom, it is crucial to select materials that mimic the properties and artifact patterns of the tissues they represent to ensure accurate and reliable simulation.

Chemical shift was measured by acquiring 3 MRI images using a SE coronal sequence with the following parameters: TR = 5000 ms, TE = 3.1 ms, FOV = 224×216 mm and voxel size = 1×1×8 mm. The first image was acquired using a bandwidth of 800 Hz/pixel to minimize the chemical shift artefact (185) and the subsequent 2 images were obtained with a bandwidth of 130 Hz/pixel and opposing frequency-encoding directions. To calculate the chemical shift, the images with the 130 Hz/pixel bandwidth and opposing frequency encoding direction were compared. The total displacement of the edges of the samples was measured in pixels and then halved to indicate the shift present in each image. This was then multiplied by the bandwidth to estimate the chemical shift.

4.2.2.2 Stability of materials

To measure stability over time, the imaging properties were measured monthly over a year using the same methodology described in section 4.2.2.1. The phantom was allowed to equilibrate to room temperature prior to each MRI scan, and this temperature was recorded using a liquid crystal strip thermometer on the

tank. Stability of the scanners for T1, T2 and CT number measurement was assured through regular QA using different phantoms throughout this work.

The stability of properties, including CT numbers, quantitative T1 and T2 relaxation times, over time was evaluated by comparing the data across the study period to baseline. The Shapiro–Wilk test was first applied to ensure normality of the data. The robust regression and outlier removal (ROUT) method, with a false discovery rate (Q value) of 1%, was then used to validate the baseline measurements and identify any outliers in the subsequent data. Values at each measurement point were compared to baseline using a one-sample t-test on the mean values, with month 1 as the baseline comparator, and statistical significance was set at $p ≤ 0.05$. Where statistically significant differences were identified, the magnitude of these differences was evaluated in comparison to the clinical context (i.e., to clinically relevant parameter ranges for the corresponding tissues, as identified from the literature), as well as within-scan variability. Additionally, plots showing variation of properties with time were also evaluated visually to assess overall trends and ensure that any statistically significant differences were interpreted in the context of both the clinical relevance of the changes and the overall stability of the properties across the study period. It is important to note that failing to reject the null hypothesis does not imply that the properties are definitively stable, but rather that no statistically significant change was detected within the observed data.

To determine the effects of radiation exposure on material properties, samples of each material were irradiated with doses of 10, 100, 250, 500, and 1000 Gy. This range was selected based on the intended use of the phantom for RT end-to-end testing and a life span of at least 500 uses, with conventional H&N treatments delivering approximately 2 Gy per fraction (186). For practicality, each dose was

applied in a single session, unlike the clincial reality where doses would be applied in multiple sessions of 2 Gy per fraction. The use of these higher doses in a single irradiation allows for an accelerated evaluation of the materials' long-term stability within a reasonable timeframe.

A CT image of all materials in the tank was acquired as in section 4.2.2.1 with the tank positioned with graticule markers placed on its lid aligned to the external lasers. The image was imported into RayStation (RaySearch Laboratories, Stockholm, Sweden). ROIs were contoured for the whole tank and for each individual material and 3D conformal RT plans were created to deliver a uniform radiation dose to the whole tank ROI with a prescription of D50% (the dose received by 50% of the ROI volume, i.e., the median dose) set to 10, 100, 250, 500 or 1000 Gy. Treatment plans included two 26x26 cm² parallel and opposed (anterior-posterior and posterior-anterior) 6 MV photon beams (Figure 4-2). The treatments were planned isocentrically with the isocentre placed in a reproducible point based on graticules on the tank. The number of monitor units (MUs) required to deliver the desired dose was calculated and the difference between D99% and D1% for each individual material was used to assess the coverage homogeneity. The coverage of all materials was homogeneous, with a maximum variation in coverage between D99% and D1% of ≤ 4%.
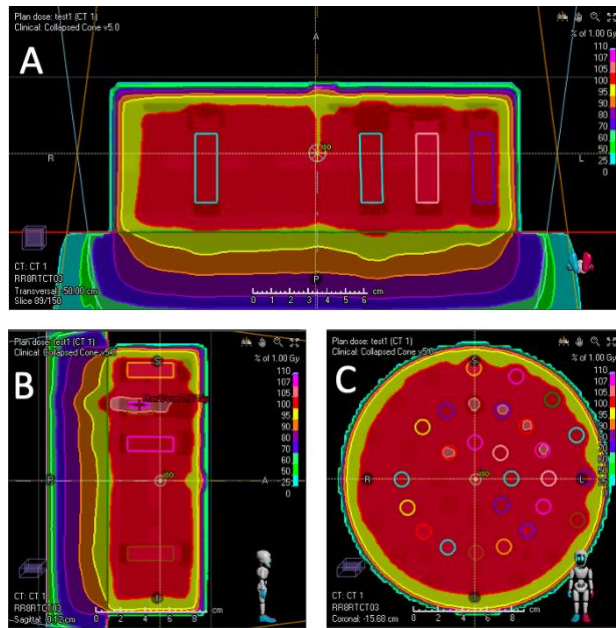
Figure 4-2 Dose distribution of the treatment planning: (A) axial, (B) sagittal and (C) coronal images.

A Versa HD™ linear accelerator (Elekta AB, Stockholm, Sweden) delivered the treatment plans. Samples were divided into five groups, each containing a sample of each material. Each group was setup in turn within the water filled tank, positioned on the treatment couch and aligned using the tanks graticules and a LAP laser system (Figure 4-3) and then exposed to the different radiation doses. After delivering the dose, T1, T2 and CT numbers were measured for all samples as described in section 4.2.2.1.
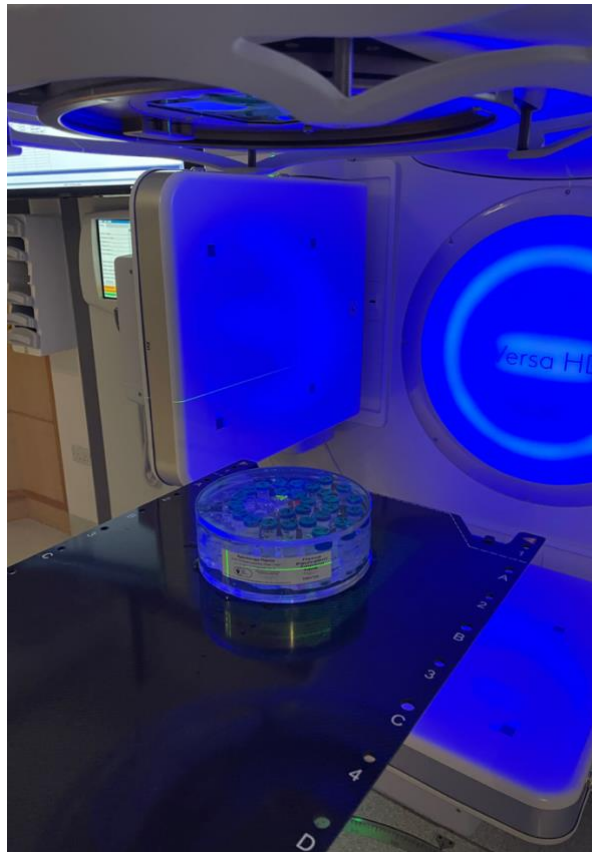
Figure 4-3 Tank on the linear accelerator table before irradiation.

To assess changes in CT numbers and T1 and T2 relaxation times with dose, a linear regression model was used. The coefficient of determination (r^2) and p-value were calculated to analyze the relationship between radiation doses (independent variable) and imaging properties (dependent variable). The Shapiro–Wilk test was applied to ensure data conformed to normality. The ROUT method, ensured there were no outlier data points.

4.2.2.3 Factors that could affect quantitative measurements

The temperature of the tank was measured using a liquid crystal strip thermometer during each MRI scan to assess its potential impact on MRI properties (187). Prior to scanning, the tank was filled with water and allowed to equilibrate before measurements.

To ensure that any observed changes were not due to scanner drift, the T1 mapping and extracellular volume (ECV) standardization (T1MES) phantom was

used. This phantom contains tubes of material with known T1 and T2 relaxation times and has FDA and CE regulatory clearance as well as demonstrated stability (188). MRI relaxation times were measured at each scanning session using the same methodology as for the sample materials. T1 and T2 relaxation times for the central tube in the T1MES phantom were reported over time.

The CT stability was ensured using the CT scanner monthly QA programme, which scans a phantom with known CT numbers and assesses the stability. Moreover, a region of water from the tank was used to verify stability. A cylindrical ROI was contoured in the middle of the tank with a size of 0.47 cm^3 and 171 voxels to obtain the mean CT number and SD of the water.

Outliers were identified and excluded using the ROUT method. After excluding outliers, the data distribution was evaluated using the Shapiro–Wilk test. A one-sample t-test was conducted to assess the stability of readings over time as discussed in section 4.2.2.2.

4.3 Results

4.3.1 Material evaluation

4.3.1.1 Assessing the similarity of candidate materials to real human tissue

Figure 4-4 to Figure 4-6 show the mean and SDs of the T1, T2 and CT number for each material at baseline.
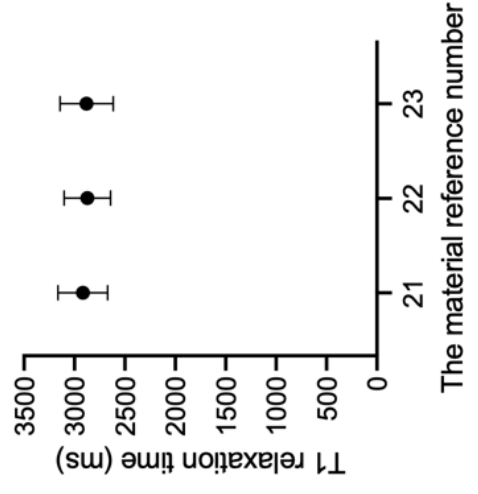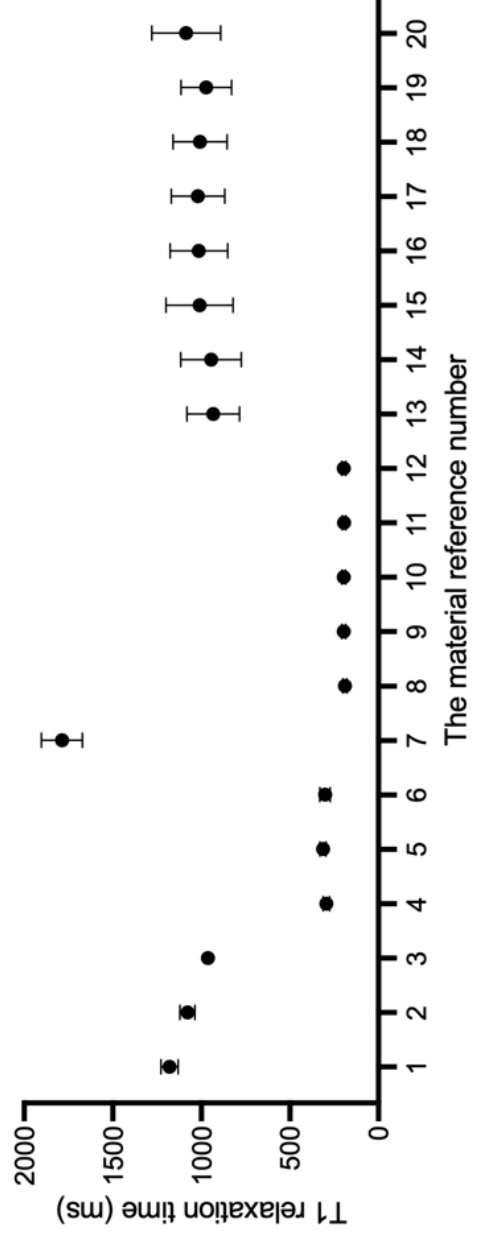
Figure 4-4 Mean (circle) and standard deviations (error bars) of T1 for each candidate material.
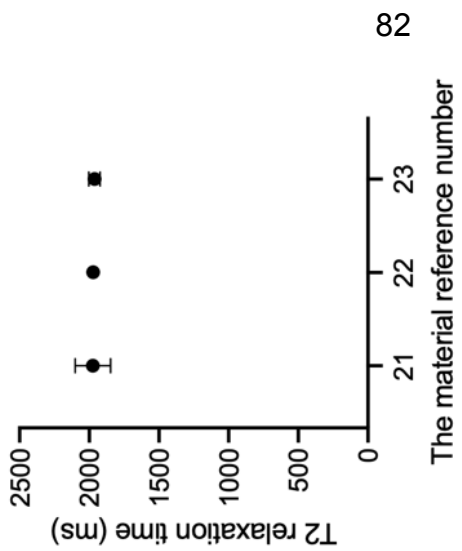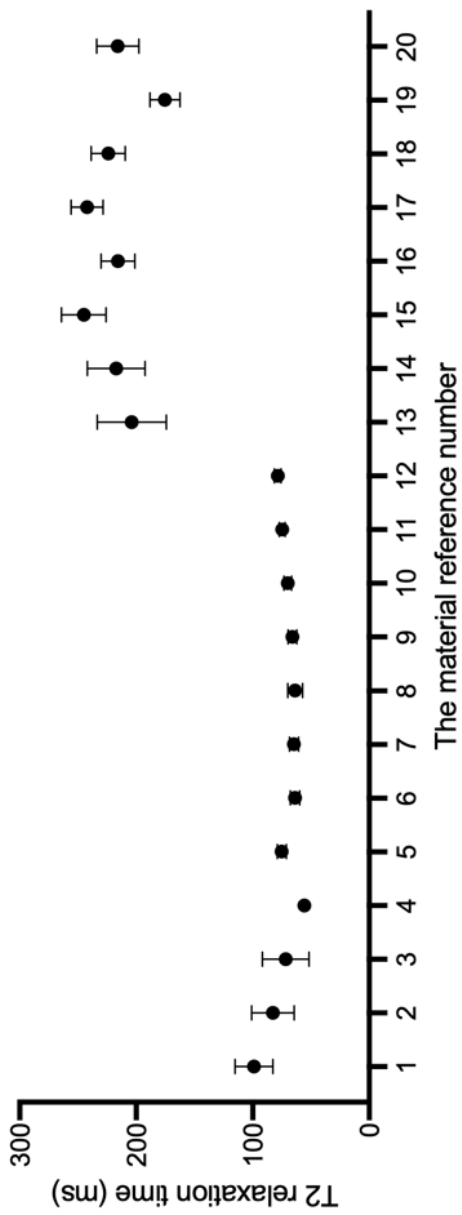
Figure 4-5 Mean (circle) and standard deviations (error bars) of T2 for each candidate material.
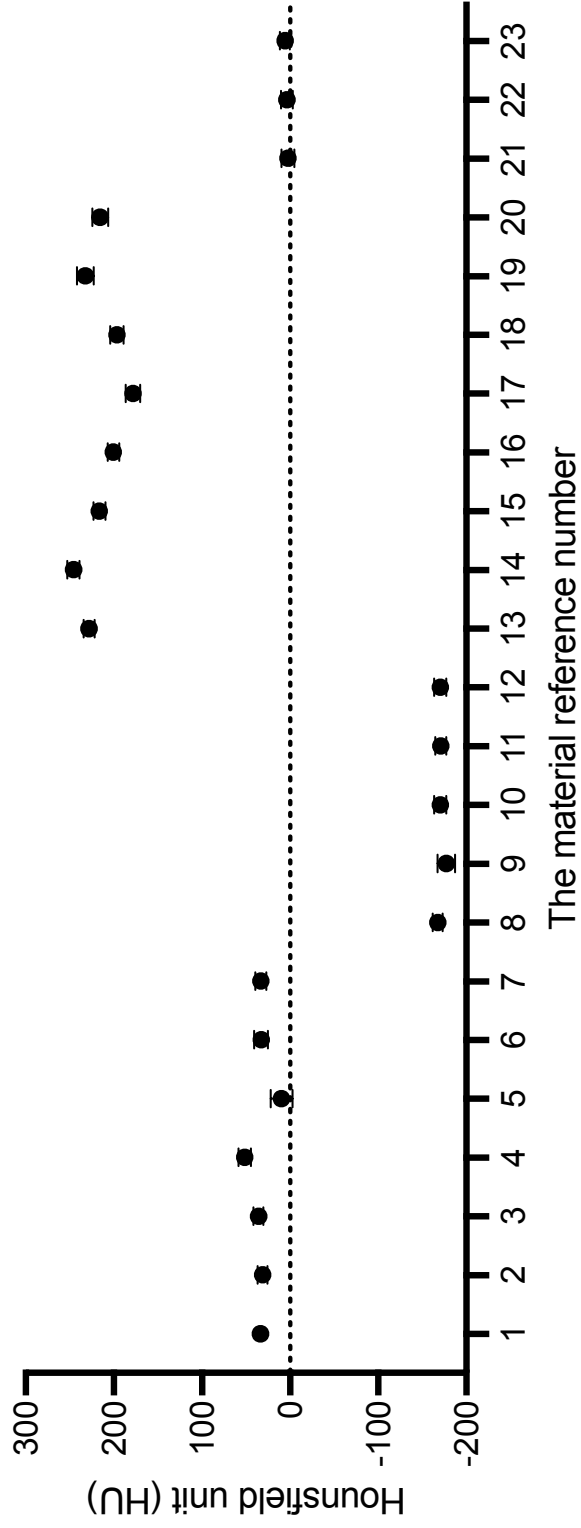
Figure 4-6 Mean (circle) and standard deviations (error bars) of CT number for each candidate material.

Figure 4-7 compares T1, T2 and CT numbers for selected materials with properties appropriate for mimicking human tissue, as detailed in Table 4-2. Notably, materials 1 and 2 were the only materials where both T1 and T2 relaxation times, as well as CT numbers, fell within the range for a specific tissue type, specifically brain grey matter. Materials 4-6 exhibited T1 and T2 relaxation times within the range for the MRI properties of fat, but do not have a suitable CT number. Additionally, materials 3, 5, and 6 demonstrated T1 and T2 relaxation times consistent with the MRI properties of brain white matter. However, while the CT numbers for these materials do not fall within the clinical range of 20 to 30 HU, materials 3 and 6 are close, with CT numbers of 36 HU and 33 HU, respectively.
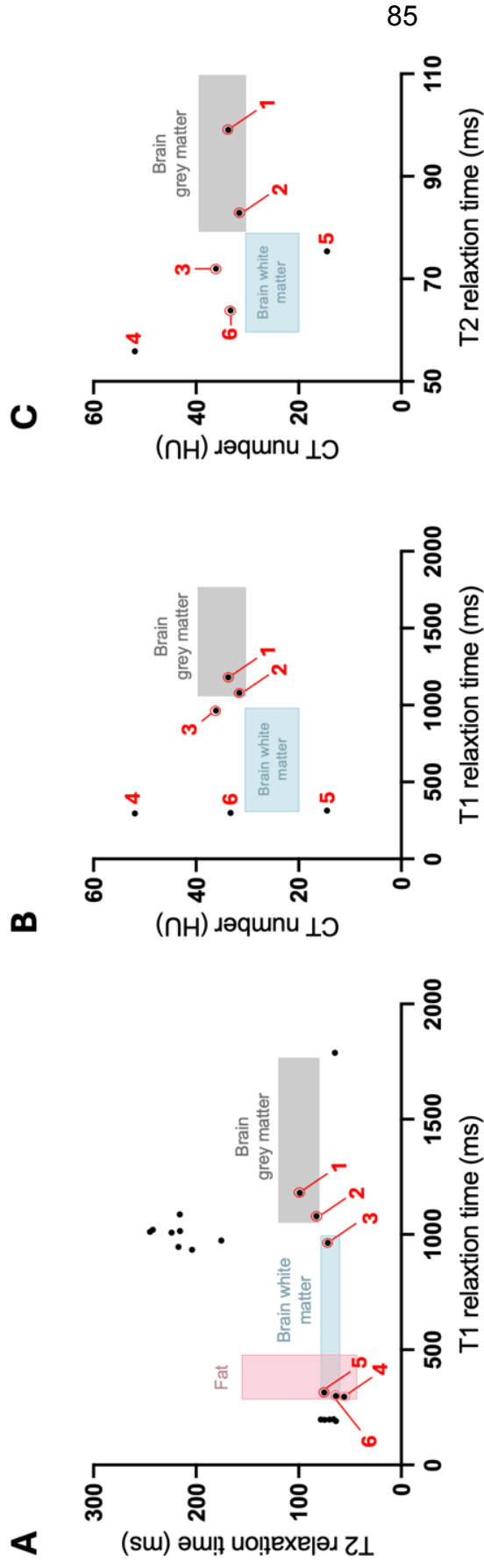
Figure 4-7 T1 and T2 relaxation times and CT numbers for selected materials and tissues. (A) T2 relaxation time (ms) versus T1 relaxation time (ms) for all materials except materials 21-23, which were excluded because their T1 and T2 values are much larger than the scale used. Materials 1 and 2 match brain grey matter, material 3 matches brain white matter, and materials 5-6 match fat for MRI. (B) and (C) CT number versus T1 relaxation time and T2 relaxation time, respectively, for materials 1-6. These figures show that materials 1 and 2 closely match brain grey matter properties in MRI and CT. The numbers in red indicate the material reference numbers. Different tissue values taken from the literature are color-coded and highlighted within the graph.

Figure 4-8 shows MR images obtained to evaluate the effect of the chemical shift artefact. All materials except materials 1, 2, 3, 7, 21, 22 and 23 exhibited a visible chemical shift artefact. Samples 4, 5, and 6 showed a pixel shift of 2 with an approximate chemical shift of 260 Hz. Sample 8, 9, 10, 11 and 12 exhibited a pixel shift of 3 with an approximate chemical shift of 390 Hz. Sample 13, 14, 15, 16, 17, 18, 19 and 20 displayed a pixel shift of 4.5 with an approximate chemical shift of 585 Hz.
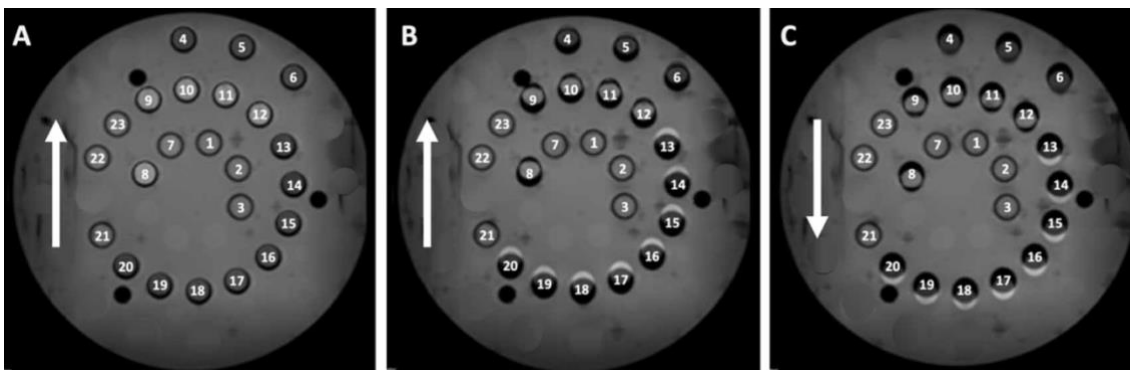
Figure 4-8 Coronal views of the samples in the tank that were obtained to evaluate the effect of chemical shift artefact. white arrow shows the frequency-encoding direction A) Image acquired with a bandwidth of 800 Hz/pixel, B) and C) Images obtained with a bandwidth of 130 Hz/pixel, the B) feet-head and C) head-feet. Alternating the frequency-encoding direction assesses whether the chemical shift artifacts are influenced by the encoding orientation, revealing any directional dependencies.

4.3.1.2 Stability of materials

Figure 4-9 shows the mean and SDs of the CT number and T1 and T2 relaxation times for materials 1-6 over time and after-radiation exposure. The results of these materials are presented because materials 1 and 2 are suitable for simulating brain grey matter in MRI and CT scans, and materials 3 and 5 suitable for simulating brain white matter and material 4-6 suitable for simulating fat in MRI scans. The results for unsuitable candidate materials are in Appendix 1. The Shapiro–Wilk test demonstrated all measurements over time and after-radiation

were normally distributed for all materials and the ROUT method did not identify

any outliers.

Figure 4-9 T1 (left) and T2 (middle) relaxation times and Hounsfield unit (right) values over time and after-radiation exposure. Mean values (circle) and their standard deviations (error bars) are displayed for materials 1-6. Numbers along the x-axis denote monthly measurements and Dx indicates the radiation dose, where x is the dose received by the sample in Gray.. Across all measurements, the solid line is the mean, and the dashed black lines are ± 2 SD. Any measurements that demonstrated a statistically significant change compared to the baseline is highlighted with ✲ or # for changes over time or dose respectively (*Continued on next page*).

Figure 4-9 T1 (left) and T2 (middle) relaxation times and Hounsfield unit (right) values over time and after-radiation exposure. Mean values (circle) and their standard deviations (error bars) are displayed for materials 1-6. Numbers along the x-axis denote monthly measurements and Dx indicates the radiation dose, where x is the dose received by the sample in Gray. Across all measurements, the solid line is the mean, and the dashed black lines are ± 2 SD. Any measurements that demonstrated a statistically significant change compared to the baseline is highlighted with ✳ or # for changes over time or dose respectively (*Continued on next page*).

Figure 4-9 T1 (left) and T2 (middle) relaxation times and Hounsfield unit (right) values over time and after-radiation exposure. Mean values (circle) and their standard deviations (error bars) are displayed for materials 1-6. Numbers along the x-axis denote monthly measurements and Dx indicates the radiation dose, where x is the dose received by the sample in Gray. Across all measurements, the solid line is the mean, and the dashed black lines are ± 2 SD. Any measurements that demonstrated a statistically significant change compared to the baseline is highlighted with ✳ or # for changes over time or dose respectively.

The imaging properties of material 1 remained consistent within the range of brain grey matter both over time and after radiation exposure. For Material 2, while the CT number and T2 relaxation time remained within the range for grey matter, the T1 relaxation time was within this range only in the first month, falling outside this range thereafter. Materials 3 and 5 exhibited T1 and T2 relaxation times consistently within the range of MRI properties for brain white matter over time and after-radiation exposure. Similarly, materials 4-6 demonstrated T1 and T2 relaxation times within the range of MRI properties for fat over time and after-radiation exposure.

Table 4-3 provides detailed statistical results, including t-values, p-values, mean difference, and 95% confidence intervals. PVA based materials (1-3) demonstrated statistically significant change over time for T1 relaxation time and CT number, furthermore material 3 demonstrated a statistically significant change for T2 relaxation time as well. Plastic based materials (4-6) only showed statistically significant changes in T2 relaxation times over time compared to the baseline.

Table 4-3 One-sample t-test and discrepancy analysis results for imaging properties across materials over time. The level of significance was set at α = 0.05. Statistically significant changes are highlighted in bold.

Sample reference number	imaging property	One sample t test		Discrepancy	
		t	P value	mean difference	95% confidence interval
1	T1	5.91	**<0.001**	-50.37 ms	-69.13 to -31.62
	T2	1.95	0.08	-0.60 ms	-1.27 to 0.08
	CT	2.76	**0.02**	1.07 HU	0.22 to 1.93
2	T1	7.03	**<0.001**	-54.98 ms	-72.19 to -37.76
	T2	1.26	0.23	-0.42 ms	-1.16 to 0.32
	CT	4.78	**<0.001**	2.88 HU	1.55 to 4.21
3	T1	6.99	**<0.001**	-47.23 ms	-62.08 to -32.37
	T2	4.21	**0.002**	-2.83 ms	-4.312 to -1.353
	CT	5.13	**<0.001**	3.01 HU	1.717 to 4.294
4	T1	1.00	0.34	2.80 ms	-3.35 to 8.94
	T2	2.71	**0.02**	-1.25 ms	-2.27 to -0.23
	CT	1.91	0.08	-1.05 HU	-2.27 to 0.16
5	T1	1.18	0.26	3.30 ms	-2.88 to 9.47
	T2	6.28	**<0.001**	-4.28 ms	-5.78 to -2.78
	CT	2.12	0.06	0.68 HU	-0.03 to 1.38
6	T1	2.07	0.06	5.00 ms	-0.32 to 10.32
	T2	4.5	**<0.001**	-2.81 ms	-4.18 to -1.44
	CT	1.65	0.13	0.67 HU	-0.22 to 1.55

Table 4-4 presents the linear regression equations, r^2 values, and P-values for Materials 1-6, showing the relationship between radiation dose and imaging properties. For PVA based materials the only statistically significant changes after-radiation was found in material 2 for the T1 relaxation time. Whereas for the plastic based materials (4-6) statistically significant changes after-radiation were found for all materials and imaging properties, except for CT for material 5 and T2 relaxation time for material 6.

Table 4-4 Linear regression equations and r² analysing the link between the radiation dose and changing imaging properties. The level of significance was set at α = 0.05. Statistically significant changes are highlighted in bold.

Sample reference number	imaging property	Regression equation (where D = dose in Gy)	Coefficient of determination (r^2)	P value
1	T1	T1 (ms) = 0.012*D + 1134	0.29	0.35
	T2	T2 (ms) = 0.002*D + 95.96	0.24	0.40
	CT	CT (HU) = -0.00*D + 36.46	0.02	0.83
2	T1	T1 (ms) = 0.033*D + 1028	0.76	**0.05**
	T2	T2 (ms) = -0.001*D + 82.43	0.08	0.64
	CT	CT (HU) = 0.002*D + 33.76	0.53	0.16
3	T1	T1 (ms) = 0.011*D + 927.1	0.22	0.42
	T2	T2 (ms) = -0.003*D + 70.16	0.37	0.28
	CT	CT (HU) = -0.002*D + 41.31	0.24	0.40
4	T1	T1 (ms) = 0.021*D + 305.7	0.95	**0.01**
	T2	T2 (ms) = 0.004*D + 55.55	0.96	**<0.001**
	CT	CT (HU) = 0.004*D + 49.78	0.76	**0.05**
5	T1	T1 (ms) = 0.022*D + 326.6	0.95	**0.01**
	T2	T2 (ms) = 0.005*D + 72.79	0.99	**<0.001**
	CT	CT (HU) = 0.002*D + 14.21	0.42	0.23
6	T1	T1 (ms) = 0.023*D + 312.0	0.97	**<0.001**
	T2	T2 (ms) = 0.002*D + 63.39	0.64	0.11
	CT	CT (HU) = 0.004*D + 32.51	0.95	**<0.001**

4.3.2 Factors that could affect quantitative measurements

Figure 4-10 depicts the temperature read from the thermometer strip on the tank.

All measurements were performed at temperatures between 22 and 25°C.
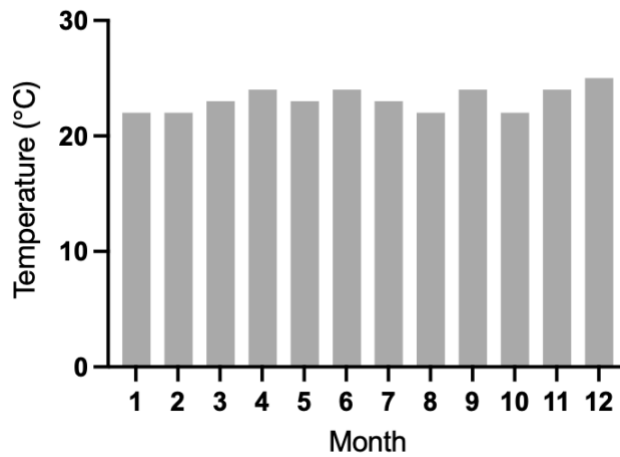
Figure 4-10 temperature during MRI sessions

Figure 4-11 illustrates the mean and SD of the T1 and T2 relaxation times for the central tube in the T1MES phantom and CT numbers of the water within the tank obtained over time. The MRI relaxation times for the rest of the tubes in the T1MES phantom are included in appendix 2.
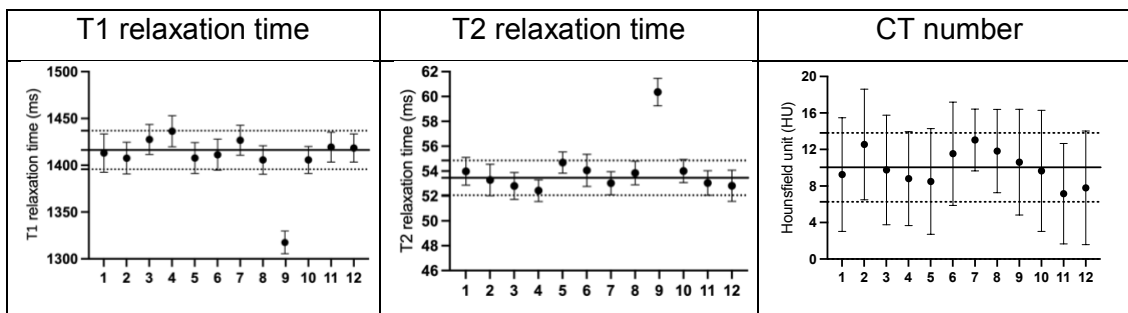
Figure 4-11 Mean T1 and T2 relaxation times and CT number (circle) and standard deviations (error bars) from the regions of interest within the central tube in the T1MES phantom and the water in the tank over time. Solid lines denote the mean of the mean values over time. Dashed black lines are ± 2 SD. Magnetic resonance imaging relaxation times for Month 9 are provided; however, they were excluded from calculating the overall mean of T1 and T2 relaxation times over 12 months and the SD because they are outliers.

The ROUT test demonstrated that the T1 and T2 relaxation times in month 9 were outliers and therefore these were removed from further statistical analysis. Once these points were removed the Shapiro–Wilk test demonstrated the data was normally distributed for all measurements. As summarized in Table 4-5, the one-

sample t-test results confirmed no statistically significant changes over time, indicating stability in the MRI and CT scanners.

Table 4-5 One-sample t-test and discrepancy analysis results assessing the stability of MRI and CT scanners over time. The level of significance was set at α = 0.05.

Image property	One sample t test		Discrepancy	
	t	P value	mean difference	95% confidence interval
T1	1.070	0.3096	3.326	-3.598 to 10.25
T2	2.109	0.0611	-0.4396	-0.9041 to 0.02483
CT	3.631	0.1742	0.7911	-0.4076 to 1.990

4.4 Discussion

Previous studies have indicated the promise of materials for use in anthropomorphic phantoms suitable for MRI or CT. However, there has been a lack of comprehensive data on material suitability for tissue equivalence for both modalities, as well as their stability over time and after-radiation exposure which are critical for RT applications. This study fills that gap by identifying 23 candidate materials for this application and then providing the first longitudinal data on the stability of these materials' imaging properties over time and after-radiation exposure as well as assessment of their multi-modality tissue equivalence. Notably, only one material met all criteria for both suitability and stability, underscoring the need for further research to identify or develop additional materials that can meet these criteria.

The T1 and T2 relaxation time mapping protocol described in this chapter was designed to balance accuracy and practical scan times. The chosen inversion times (TI = 83, 400, 1500, 2890 ms) for T1 mapping and echo times (TEs = 12.4 to 396.8 ms in 32 intervals) were selected to provide reasonable coverage of a

broad range of expected relaxation times for the materials under investigation. For T1 mapping, the protocol is expected to perform well for materials with relaxation times of ~100–2000 ms, typical of biological tissues. However, very short T1 values (<100 ms) or very long T1 values (>2000 ms) may not be optimally captured due to the absence of very short or sufficiently long TIs. Similarly, for T2 mapping, the selected TEs are suitable for T2 values of ~10–300 ms, covering most soft tissues, but very short T2 values (<10 ms) or very long T2 values (>300 ms) may not be adequately sampled. The lack of prior knowledge about the materials required compromises in parameter selection, potentially limiting the protocol's applicability to extreme cases. Future studies could refine the protocol through preliminary investigations, but it remains a practical framework for most relevant materials.

Statistical methods were combined with practical interpretation to evaluate the stability of material properties over time. Although statistically significant differences were identified at certain time points, these differences were assessed against established clinical parameter ranges for the corresponding tissues. This ensured that statistical significance was not confused with clinically relevant changes. The suitability and stability of 10% PVA-c for mimicking brain grey matter in both MRI and CT is highly important, indicating its potential utility for multimodality (MRI/CT) phantoms for RT purposes. Increasing the PVA concentration resulted in no appreciable change to CT number and a decrease in T1 and T2 relaxation times, consistent with the literature (170, 171). For example, a 14.3% concentration of PVA-c (material 3) demonstrated MRI properties suitable for brain white matter, which have shorter MRI relaxation times than brain grey matter, however this material did not have suitable CT properties so would only be suitable for an anthropomorphic phantom for MRI. This indicates

that while altering PVA concentration may help in identifying materials with suitable MRI properties for tissues with short relaxation times, such as fat, it is not a suitable method for altering CT properties.

Regarding the stability of PVA-c materials after-radiation exposure, no significant changes to materials were found, except for the T1 relaxation time for one material. Over time, some statistically significant changes in imaging properties were observed. This is potentially due to water absorption, which will replace air for water in the material (increasing CT number) while increasing the bound water content in the material, thus decreasing T1 relaxation time due to the restricted molecular motion of bound water facilitating faster energy exchange (189, 190). Although statistically significant changes to imaging properties were found, material 1 maintained grey matter-like properties over 1 year and up to 1000 Gy, indicating any statistically significant changes were not clinically significant. However, for QA tests comparing the baseline with subsequent measurements, any small changes to imaging properties could affect the results.

Surry et al. (169) developed 10% PVA-c using four FTCs, similar to this study's method but with differing FTC durations (12 h freezing and 8-9 h thawing). They reported T1 and T2 of 740 ms and 108 ms, respectively at 1.5T, whereas this study found 1180 ms and 99 ms at 3T. T1 generally increases with higher magnetic field strength (191), while T2 changes are negligible (192), but the observed 59.4% difference in T1 exceeds the typical 20-40% variation reported between 1.5T and 3T in biological tissues (192). This could be due to the differing FTC duration or differences in the field strength response of PVA-c T1 compared to those tissues. Further experiments using 1.5T scanners and varying FTC durations could explore this hypothesis.

This study found that plastic-based materials, while having suitable MRI properties for white matter and fat, were unsuitable for CT due to their CT numbers. Accurate CT information is crucial for RT planning, which these materials did not provide, although they remain viable for MRI phantoms. Regarding the stability of the plastic materials, over time only their T2 relaxation times significantly decreased. Furthermore significant relationships were found between radiation dose and their imaging properties, except for the CT number for material 5 and the T2 relaxation time for material 6. This is potentially due to radiation causing cross-linking (193) and shrinkage, increasing material density and causing the environment to become more restricted affecting both CT and MRI properties (194).

Chemical shift artifacts were noted for a wide range of materials, with them being largest on the synthetic gelatin and silicone based materials. This was expected for silicone, with the chemical shift of similar materials in implants widely known to cause pronounced artifacts (195, 196). These materials were deemed unsuitable for phantoms in terms of their MRI and CT properties. For materials with suitable MRI and/or CT properties, the plastic based materials 4-6 demonstrated chemical shift of 260 Hz at 3T, less than the 420 Hz shift between fat and water at 3T (197), suggesting that materials 4-6 could play a role mimicking fat in MRI phantoms. In addition to chemical shift artifacts, this study has not yet explored geometric distortions from magnetic susceptibility differences and material inhomogeneities, nor compared these with those in human tissues. Further research is needed to fully understand these factors.

Small differences in CT numbers for some materials compared to literature values were observed, notably for Dragon Skin™ 30 which has a reported CT number

of 294 HU (15), compared to 246 HU measured in this study. These small discrepancies may be due to variations in manufacturing processes.

The temperature during MRI sessions remained stable, with minor variations that are unlikely to significantly affect the material properties. Such small changes are not expected to significantly affect relaxation times. According to Tsukiashi et al. (198), a 1°C increase is expected to increase T1 by about 5.8 ms and T2 by about 1.2 ms. Perfect stability of MRI relaxation times or CT numbers is not the goal, as anthropomorphic phantoms in RT are not typically used to evaluate changes in T1 and T2 or CT numbers. However, the anthropomorphic phantoms must still fall within the limits of the human tissues they are designed to simulate.

For the after-radiation assessment, materials received their radiation dose in a single session, rather than in fractionated doses as is clinically standard for H&N cancer patients and routinely in phantoms. While this approach does result in a more immediate deposition of energy, the associated temperature rise is expected to be very limited and unlikely to affect the material.

During the monthly sample evaluations, the MRI relaxation times were measured using the T1MES phantom to ensure that any changes in the MRI relaxation times for the materials were not due to a defect in the MRI scanner. The statistical analysis proved that the MRI relaxation times for the T1MES phantom at Month 9 were outliers and did not correspond to any notable change in the T1 and T2 relaxation times of the materials themselves. This can be a possible random error in these readings, perhaps due to magnetic field inhomogeneities (the shimming was poor) during the scan. Furthermore, the measured MRI relaxation times of the T1MES phantom and the CT numbers recorded using the CT scanner were stable over time, indicating consistent scanner performance.

sCT images from MRI is crucial for MR-only workflows in RT, as it requires accurate MR properties to ensure reliable electron density representation for dose calculations. Variations in MR signal properties can lead to deviations in the predicted sCT, potentially compromising treatment accuracy. While anthropomorphic phantoms are valuable for QA and training artificial intelligence (AI) algorithms, they inherently fall short in replicating the complexity and variability of human tissues, such as heterogeneity and anatomical irregularities.

Limitations of the study include the use of small test tubes, selected for measurement efficiency but which may have affected measurement precision due to limited number of voxels, and the one-year study duration, whereas phantoms are typically used for five years or more (199). Future studies should consider longer evaluation periods and larger samples for more robust data. Additionally, liquid crystal thermometers, though MRI-compatible, are less precise than digital or mercury thermometers, suggesting the need for more accurate temperature measurements in future studies.

This study relies on a single sample for stability testing, which limits the generalizability of the findings. A single sample may not capture variability due to potential defects in material preparation or anomalies during testing, potentially leading to the rejection of an otherwise ideal material or overestimation of performance. Future studies should include multiple samples to ensure reproducibility and robustness of the conclusions.

This study evaluated candidate materials for MR/CT multimodal phantoms, identifying few suitable options for developing anthropomorphic phantoms. Specifically, a 10% concentration of PVA-c shows promise as a suitable material for brain grey matter for MRI and CT, and multiple materials were appropriate for

white matter and fat on MRI only. Collaboration between materials science and medical imaging experts is crucial for further advancing the development of suitable materials for multimodality imaging phantoms.

4.5 Conclusion

A literature search identified 23 materials in the literature as candidate tissue substitutes suitable for developing multimodality (MRI/CT) anthropomorphic phantoms for the H&N for RT purposes. This study assessed the MRI and CT properties of all 23 materials over a year and after radiation exposure up to 1000 Gy. The results indicate that there are currently insufficient materials to mimic all human H&N tissues accurately in both MRI and CT scans. However, the study found that a concentration of 10% PVA-c is a viable substitute for brain grey matter in these imaging modalities.

Over a one-year period and after exposure to radiation doses up to 1000 Gy, the imaging properties of 10% PVA-c remained stable, demonstrating its potential for long-term use in phantom development. Despite this success, the findings highlight the need for further research and development to identify additional candidate materials capable of accurately simulating a wider range of human tissues. Such advancements are crucial for the future development of comprehensive multimodality anthropomorphic phantoms for medical imaging and RT planning.

Chapter 5 Assessing if a Multimodality Anthropomorphic Phantom Enhances Compliance with Quality Assurance Guidelines for MRI in Radiotherapy

5.1 Introduction

MRI has evolved from a diagnostic tool to a critical component in RT treatment planning, improving tumor targeting. Historically, MRI QA protocols (200-202) focused on diagnostic applications. These protocols are insufficient for RT applications, which demand precise geometric fidelity, and accurate radiation dose evaluations. In response, both the IPEM (16) and the AAPM (17) have developed guidelines for using MRI simulation in RT. These guidelines include comprehensive recommendations for QA tests specifically designed to assess MRI's suitability in RT applications. These guidelines encompass traditional diagnostic QA procedures and introduce new tests critical for MRI in RT addressing aspects such as informatics/connectivity/data transfer, MRI-CT registration, comprehensive end-to-end processes, RT accessories QA, and geometric distortion over large fields of view.

There are different types of phantoms specified for different tests. Homogeneous phantoms containing a single uniform substance such as those provided by medical imaging vendors (200, 201). They are typically used to assess image quality and uniformity (203). Geometric phantoms containing specific geometric features such as grids, ramps, and wedges. Geometric phantoms are primarily used for evaluating spatial resolution, image distortion, and the geometric fidelity of MRI images (201). A key example of a geometric phantoms used in MRI is the American College of Radiology (ACR) large MRI phantom, which is a short, hollow acrylic cylinder, sealed at both ends (201). To simulate biological conductivity, the phantom is filled with 10 millimolar (mmol) nickel chloride

solution containing sodium chloride (45 mmol) (201). This phantom contains different structures to evaluate seven measures: geometric accuracy, high-contrast spatial resolution, slice-thickness accuracy, slice-position accuracy, image intensity uniformity, percent signal ghosting and low-contrast object detectability.

Anthropomorphic phantoms are those that have been developed to mimic the human anatomy and tissue composition. One such example is the anthropomorphic multimodal H&N phantom that was developed by the University of Leeds, Leeds Test Objects (LTO) Ltd. (Boroughbridge, UK) and the Leeds Teaching Hospitals NHS Trust (LTHT) collaboration (13).

In RT, single modality CT anthropomorphic phantoms have been in use for a long time in dosimetric audits (204, 205). Multimodal anthropomorphic phantoms are rarely available commercially or even developed in-house. Only a few institutions have created such phantoms for CT/MRI applications (138, 140), mainly for end-to-end tests in MRI for RT which is a process that verifies the accuracy and safety of the entire treatment process from simulation to dose delivery. Anthropomorphic phantoms have the advantage that they can be used to mimic a human workflow (206) and, when used for RT purposes, provide more accurate and representative data on radiation dose absorption in the human body (207).

Although interest in such phantoms has increased, there is still a lack of detailed studies comparing their effectiveness against other phantoms in real clinical settings. Followill et al. (208) suggest that standard homogeneous phantoms may miss patient-specific complexities, making anthropomorphic phantoms more suitable for advanced RT. Hazelaar et al (209) stated that it is hard to predict how an imaging system tested on homogeneous or geometric phantoms will perform on humans. Adjeiwaah et al. (210) evaluated the ACR MRI QA phantom and a

large FOV geometric phantom for detecting MRI image quality issues in RT. Their findings suggest that this combination is effective. However, their study focused solely on image quality, whereas the guidelines for using MRI in RT (16, 17) included more comprehensive tests than just ensuring image quality. Adjeiwaah et al. (210) also emphasize the need to develop dedicated QA protocols and phantoms specifically designed for MRI systems used in RT.

Lewis et al. (211) compared the QUASAR™ magnetic resonance-guided radiotherapy (MRgRT) Insight Phantom (Modus Medical Devices Inc.; London, Ontario, Canada), which is a geometric phantom for a large FOV, with an ACR phantom. They found that MRgRT Insight phantom is effective for MRI image quality assessment, providing easier setup and reliable imaging over a larger area compared to the ACR phantom. To further enhance our understanding of phantom performance in QA tests in MRI for RT, there is a need to expand the scope of evaluation to include anthropomorphic phantoms, comparing them with geometric phantoms like the ACR. Such a comparative study is essential to comprehensively understand the potential of various phantom types in MRI QA processes for RT.

To the best of the author's knowledge, there has not yet been a comprehensive evaluation of the use of anthropomorphic phantoms for conducting the QA tests recommended in international guidelines for MR in RT QA (16, 17). The hypothesis for this research was that anthropomorphic phantoms, due to their more realistic representation of clinical scenarios of a patient compared to geometric phantoms, could specifically enhance the effectiveness and accuracy of certain QA tests in MRI for RT. This research aims to identify and assess which particular QA tests would most benefit from the application of anthropomorphic phantoms, by comparing these results with those obtained using geometric or

homogeneous phantom. This comparison aims to provide increased confidence in the use of MRI for RT.

5.2 Methods

Three phantoms were compared in this work: Firstly, an ACR large MRI phantom (201). Secondly, the anthropomorphic multimodal H&N phantom developed in earlier work conducted in Leeds (13) henceforth referred to as 'anthropomorphic phantom'. The brain in the phantom is composed of 10% PVA-C, which was evaluated in the previous chapter for its tissue-mimicking properties. Thirdly, the Siemens MRI QA phantom 5300ml, which is a cylinder containing a homogeneous solution (per 1000g H_2O dist.: 3.75g $NiSO_4$ x $6H_2O$ + 5g NaCl) referred to as the 'homogeneous phantom'.

All QA tests that require a phantom as recommended in the guidelines for using MRI in RT (16, 17) have been reviewed. These tests were categorized based on the suitability of the anthropomorphic phantom. Table 5-1 lists the QA tests for which the anthropomorphic phantom is not suitable, along with the specific reasons for its unsuitability.

Table 5-1 List of QA tests that the anthropomorphic phantom is not suitable to perform, and the reasons why it is unsuitable (16, 17).

Test	Reason
Determine or verify external laser offset from MR isocentre	The anthropomorphic phantom does not have suitable internal markers.
Magnetic field homogeneity (B_0)	Inhomogeneities in the anthropomorphic phantom itself might be mistaken for magnetic field inhomogeneities and using a heterogeneous phantom would be complex. A spherical homogeneous phantom is recommended (17).
Characterisation of residual gradient nonlinearity (GNL)	The anthropomorphic phantom does not cover more than 80% of the usable FOV (17).
Table alignment with B_0	This test cannot be performed with the anthropomorphic phantom because it lacks the precise reference points required, and a grid phantom is recommended (17).
Motion verification	The anthropomorphic phantom is not a motion phantom.
Geometric accuracy	This test cannot be performed with the anthropomorphic phantom, as it requires a phantom with a diameter/width greater than 30 cm.
High-contrast spatial resolution	This test cannot be performed using the anthropomorphic phantom; since it contains no appropriate internal markers.
Low contrast detectability	This test cannot be performed using the anthropomorphic phantom; since it contains no appropriate internal markers.
Laser alignment with imaging isocentre	There are no internal landmarks that can be used to perform this test with the anthropomorphic phantom.
External laser agreement with imaging plane	There are no internal landmarks that can be used to perform this test with the anthropomorphic phantom.
High performance imaging	The anthropomorphic phantom is unsuitable for this test as it is recommended to use phantoms with known diffusion properties, like ice water-based DWI or QIBA DWI phantoms (212).

The anthropomorphic phantom is suitable for the remainder of the QA tests recommended in the guidelines. Table 5-2 shows these QA tests and their tolerance.

Table 5-2 List of QA tests, and their tolerances, recommended by AAPM and IPEM guidelines that can be performed using the anthropomorphic phantom (16, 17).

Test number	Test	tolerance
1	Magnetic Field Drift Test	Should not exceed 1 part per million (ppm)/day during acceptance testing or 0.25 ppm/day for the first one to two months of operation (17).
2	Transmitter and Gain Calibration	The manually determined transmit gain values should fall within ±5% of those determined automatically (17).
3	Radiofrequency Coil Evaluation	SNR action limit set at ± one standard deviation by a medical physicist/MRI scientist, based on baseline measurements. Head coil Percent Image Uniformity (PIU) should be 82% or more for 3T systems and ghosting ratios less than 2.5% in T1-weighted spin-echo head scans (17).
4	Artefact evaluation	No obvious image artifacts and phantom appearing circular with a diameter within ±2 mm of true values (16, 17)
5	QA of RT accessories	Clinical decision on SNR and image quality (16).
6	Informatics, connectivity and data transfer	Ensure scanner is interfaced to required DICOM locations (e.g., Treatment Planning System, PACS and archive) (16, 17).
7	QA for MRI-CT registration using physical phantom	Mean Distance to Agreement (MDA) > 2-3 mm and/or Dice Similarity Coefficient (DSC) < 0.9 (16).
8	End-to-end QA	For most RT applications, the advised tolerance is 2 mm in positioning and dose delivery, with stricter values for certain applications (16, 17). The dose delivered to the phantom should be within ±3% of the prescribed dose (213).

The main comparison in the study was between the anthropomorphic phantom and ACR phantom, with the ACR phantom being widely used and well-trusted clinically for MRI in RT purposes (214, 215). Additionally, in instances where guidelines recommend the use of a homogeneous phantom, it was employed as

the gold standard for comparison with the other phantoms. Tests 1-5 were performed with all three phantoms, tests 6-8 were performed only with the ACR and anthropomorphic phantoms because homogeneous phantom lacks the internal details crucial for these tests and is not recommended by the guidelines (16, 17).

A 3T Siemens Prisma MRI scanner (Siemens Healthineers, Erlangen, Germany) was employed for all QA tests. When CT images were required, a Philips Brilliance Big Bore CT scanner (Philips Medical Systems, The Netherlands) was used. For the end-to-end test, an Elekta Versa HD linear accelerator (Linac) (Elekta Oncology Systems Ltd, Crawley, UK) was used. For tests requiring a treatment planning system (TPS) RayStation version 13.1 (RaySearch Labs, Stockholm, Sweden) was used.

5.2.1 Magnetic Field Drift Test

The Magnetic Field Drift test aims to evaluate and verify the long-term stability of the MRI scanner's magnetic field. This assessment was conducted using three phantoms, all positioned within the 20-channel H&N coil. The ACR phantom was positioned head-first supine (HFS) with the NOSE end facing anteriorly and the CHIN end inferiorly. Graticule markers were aligned with the MRI scanner's lasers, following ACR guidelines (201), with foam pads and spirit levels ensuring precise alignment across all axes (Figure 5-1).
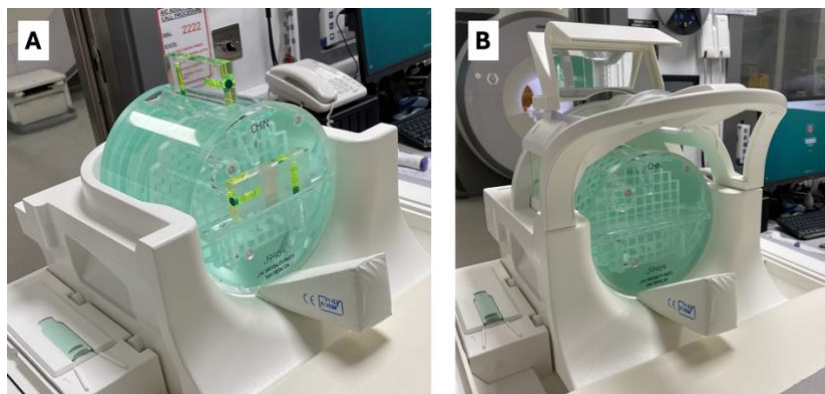
Figure 5-1 ACR phantom on the MRI table the 20-channel H&N coil. A) Before closing the coil, two spirit levels are shown, and B) after closing the coil.

For the anthropomorphic phantom, cross marks were drawn on its surface to ensure reproducibility (Figure 5-2), and it was positioned HFS in the coil, with the marks aligned to the lasers.

Figure 5-2 Anthropomorphic phantom with temporary marks.

The homogeneous phantom was placed in a dedicated holder at the centre of the coil, using the manufacturer's label with a horizontal line for laser alignment (Figure 5-3).
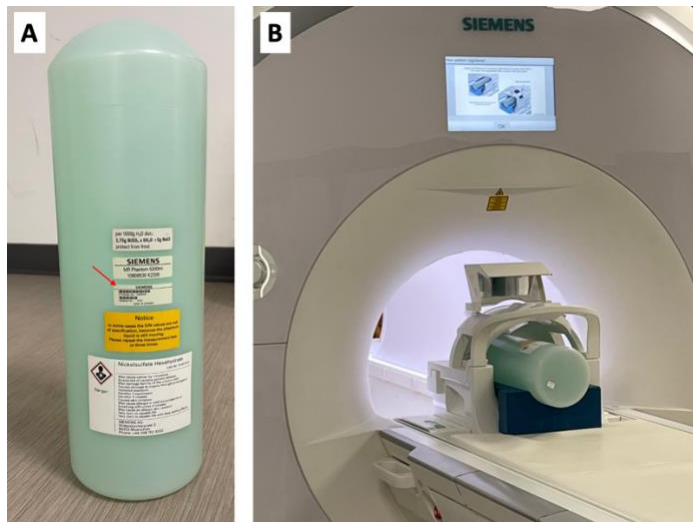
Figure 5-3 Homogeneous phantom. A) the phantom and the red arrow indicates the mark chosen to align the phantom. B) the phantom on the MRI table in the coil.

For each phantom, a local shim box was applied to the localizer images to encompass a specific region of interest (ROI) (see Figure 5-4). During a single session, three consecutive prescans were conducted without altering the phantom setup to assess equipment-associated variation. To evaluate the sensitivity of the measurements to changes in phantom setup, two additional prescans were performed, with the phantom being removed from and repositioned on the MRI table between each scan.
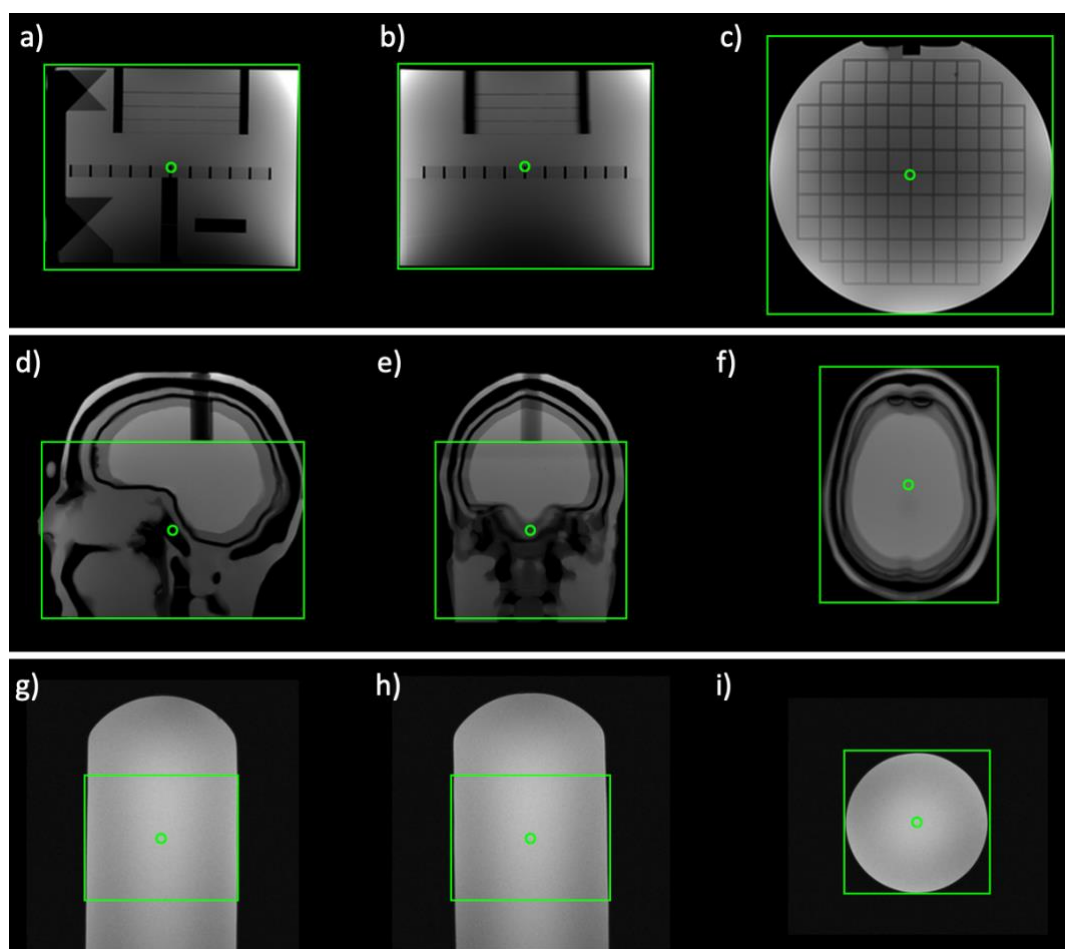
Figure 5-4 Localized MRI scans with shim boxes. a-c) ACR phantom: a) sagittal, b) coronal, and c) axial views. d-f) Anthropomorphic phantom: d) sagittal, e) coronal, and f) axial views. g-i) Homogeneous phantom: g) sagittal, h) coronal, and i) axial views.

The central frequency value, measured in Hertz (Hz), was obtained directly from the scanner console. For both the same and varying setup conditions, the mean and standard deviation of the central frequency values were calculated. From these the coefficient of variation (CoV) was calculated between repeat scans with the same setup and varying setups.

5.2.2 Transmitter and Gain Calibration

The objective of this test is to ensure the MRI scanner's gain are accurately calibrated for optimal image quality. This test was conducted using three phantoms. Each phantom was positioned within the 20-channel H&N coil as

described in Section 5.2.1. A prescan was performed for each phantom, and the value of the automatically determined transmitter gain was recorded.

To manually define the correct gain, six images of a homogeneous region were taken from each phantom. Images were acquired using different gain values: X-5%, X-10%, X, X+5%, X+10%, and X+15%, where X is the automatically determined gain. The images were obtained using the T1 gradient-echo sequence, with the acquisition parameters outlined in Table 5-3. The repetition time (TR) was set to at least 5 times longer than the T1 relaxation time of the phantom solution which was 149 ms for the ACR phantom (216), 1200 ms for the anthropomorphic phantom (13), and 107 ms for the homogeneous phantom (217).

Table 5-3 Scanning parameters of sequences used in this study

Test	Phantom	Sequence type	TR (ms)	TE (ms)	FOV (mm)	number of slices	Slice thickness (mm)	Slacing between slices / slice gap (mm)	Number of Excitations (NEX)	Matrix	Scan time (seconds)
Transmitter and Gain Calibration	ACR	T1-weighted gradient-echo	1000								8
	Anthropomorphic	T1-weighted gradient-echo	7500	2.9	256×256	1	5	N/A	1	64×64	360
	Homogeneous	T1-weighted gradient-echo	1000								8
Radiofrequency Coil Evaluation	All phantoms	T1-weighted Spin Echo	500	20	256×256	11	5	5 / 0	1	256×256	127.8
Informatics, connectivity, and data transfer		T1-weighted Turbo Spin Echo	405	12	256×256	11	5	10 / 5	1	128×128	3
QA for MRI-CT registration		T1-weighted Spin Echo	565	8.9	250×203	66	2	2 / 0	1	512×416	94.2
		T2-weighted Turbo Spin Echo	8730	116	250×203	85	2	2 / 0	1	512×416	150
QA of RT Accessories		T2-weighted Turbo Spin Echo	8730	116	250×203	85	2	2 / 0	1	512×416	150

Each phantom underwent three prescans with the same setups and followed by two additional prescans with varying setups, to automatically determine the transmitter gain. The correct gain was manually determined in three experiments with same setups and two additional experiments with varying setups, applied to both the ACR and homogeneous phantoms. However, due to the fact that acquiring a single image of the anthropomorphic phantom requires approximately 6 minutes, conducting one experiment involving six different gain values would take around 36 minutes. Extending this procedure to five experiments would have required approximately 3 hours. Due to the limited availability of MRI scanner time, the study was restricted to a single experiment.

For each phantom, a circular ROI was centrally drawn on an image using FIJI (ImageJ2) software (version 2.14.0/1.54f) and then this ROI was consistently replicated across all other images of the same phantom. The ROIs' sizes were proportionate to the phantoms' cross-sectional areas: 28.32 cm² (10.16% of 278.56 cm²) for ACR, 23.36 cm² (10.77% of 216.96 cm²) for anthropomorphic, and 15.52 cm² (11.00% of 141.12 cm²) for homogeneous (see Figure 5-5).
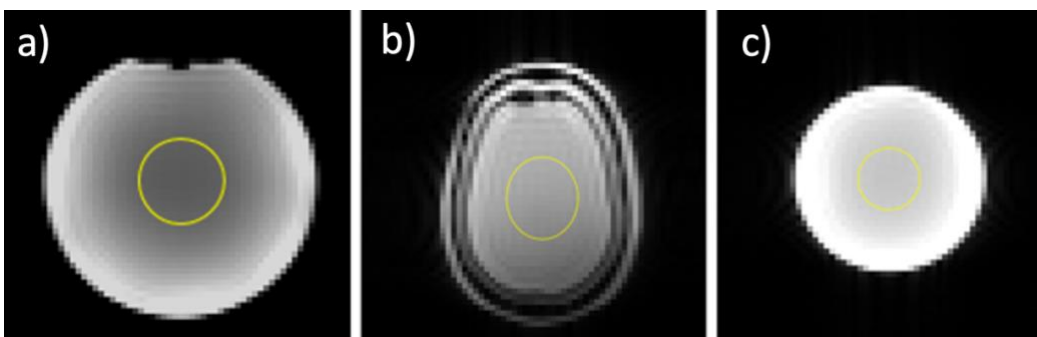
Figure 5-5 An example of a ROI drawn in the centre of the phantom to calculate the mean signal intensity. A) ACR Phantom. B) Anthropomorphic phantom and C) homogeneous phantom.

The mean signal intensity from each image's ROI was calculated and plotted against the gain using in-house written Matlab code (The MathWorks Inc., Natick, USA). A sinusoidal function was employed to model the relationship between the transmit gain and the resulting signal intensity. This function is reflective of the expected periodic behavior of signal response due to changes in nutation angle induced by varying transmit gains. The transmit gain corresponding to the peak of the fitted sinusoidal curve was extracted as the optimal gain value. This value represents the gain setting at which the signal intensity is maximized at 90° flip angle.

The manually determined transmitter gain values were then compared with those obtained through automatic measurements. The mean and standard deviation of transmitter gains from auto-prescan experiments were calculated for both the same setup and varying setup experiments. The CoV for each setup type was independently calculated.

5.2.3 Radiofrequency Coil Evaluation

In the same position and setting as described in Section 5.2.1, data were acquired for all phantoms using the T1 spin echo sequence, with parameters recommended by the ACR (201) as listed in Table 5-3.

For the ACR phantom, a high-quality sagittal localizer image was first acquired to ensure precise positioning in the slice direction. The acquisition parameters were as follows: TR = 200 ms, Echo Time (TE) = 20 ms, FOV = 250 mm, slice thickness = 20 mm, Number of Excitations (NEX) = 1, Matrix = 256×256, and scan time = 51.2 seconds. Using localizer images, 11 axial slices were selected, with slices 1 and 11 aligned with cross wedges following the recommendations of the ACR (201). Slice 7 recommended by the ACR (201) as the uniform slice was used for analysis.

For the anthropomorphic phantom, 11 axial slices were selected in a reproducible manner using the localizer images, with the central slice aligned with the air void visible in the sagittal image. Figure 5-6 shows the slices obtained from the anthropomorphic phantom. Slice number 10 was selected for analysis as it contained the largest homogeneous region within the brain.
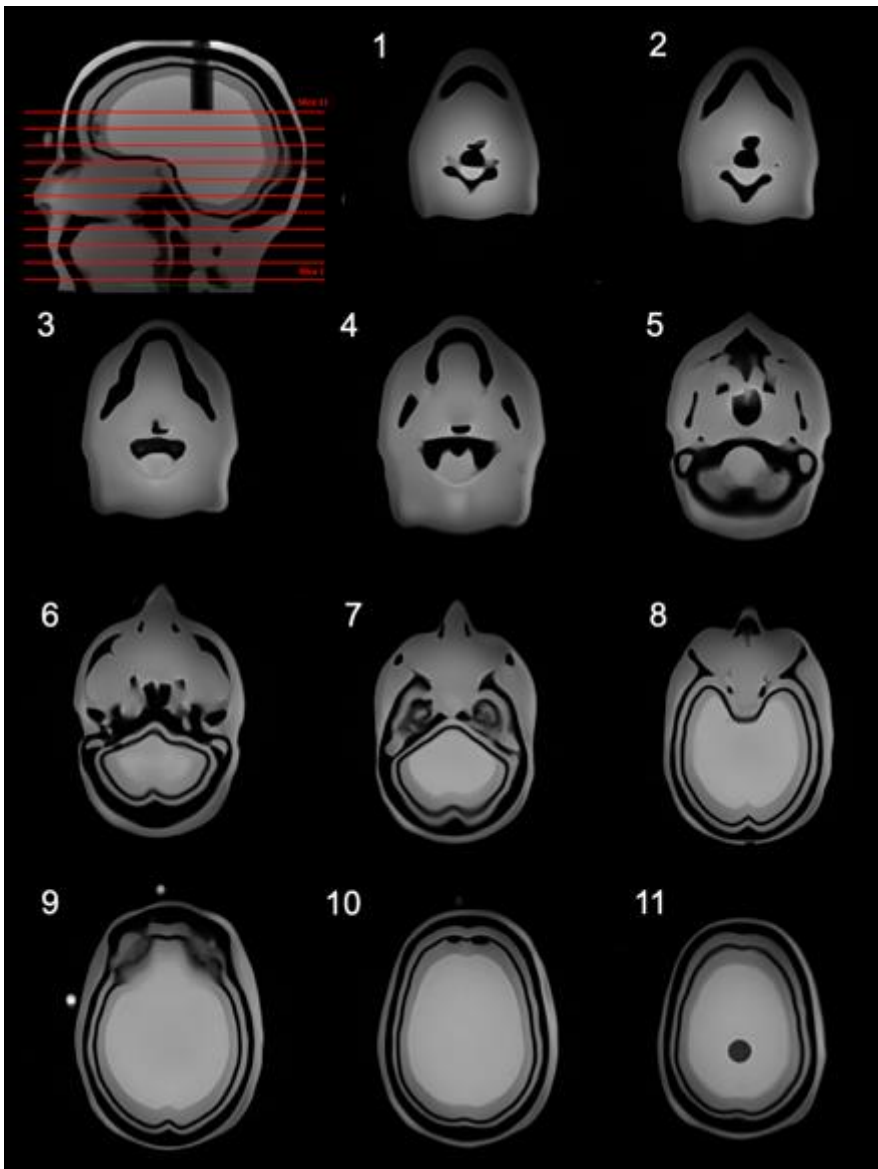
Figure 5-6 shows the sagittal localizer and the eleven axial slices obtained from the anthropomorphic phantom.

For the homogeneous phantom, 11 axial slices were selected based on the localizer images, with the central slice aligned with the mid-coronal image from the localizer. Analysis was performed on Slice 6 as the middle image.

In a single session, each phantom underwent three scans with the same setup and two additional scans with a varying setup. According to the guidelines (16, 17), it is recommended to perform this test using all coils employed in RT. However, for the purposes of this comparison, the test was conducted exclusively with the 20-channel H&N coil. Fiji software was used to display and analyze the images for each phantom. Signal-to-Noise Ratio (SNR), Percent Image Uniformity (PIU), and Percent Signal Ghosting (PSG) were calculated in accordance with the ACR Quality Control Manual (201).

For SNR, a ROI was centrally drawn within the phantom to measure the signal intensity. The initial ROI encircled the phantom's periphery and was then reduced to avoid edge effects. For the homogeneous and ACR phantoms, the circular ROI was scaled down, while for the anthropomorphic phantom, a brain-sized ROI was used. For the ACR phantom SNR, a signal ROI was defined as a circle covering 62.4% of the phantom's area on that slice to avoid edge effects. This is smaller than the recommended 75% (201) due to a plastic bar at the top of the phantom. The mean signal intensity within this ROI was calculated, along with the standard deviation, which was derived from two additional ROIs positioned outside the object, one above and one below the phantom (see Figure 5-7).
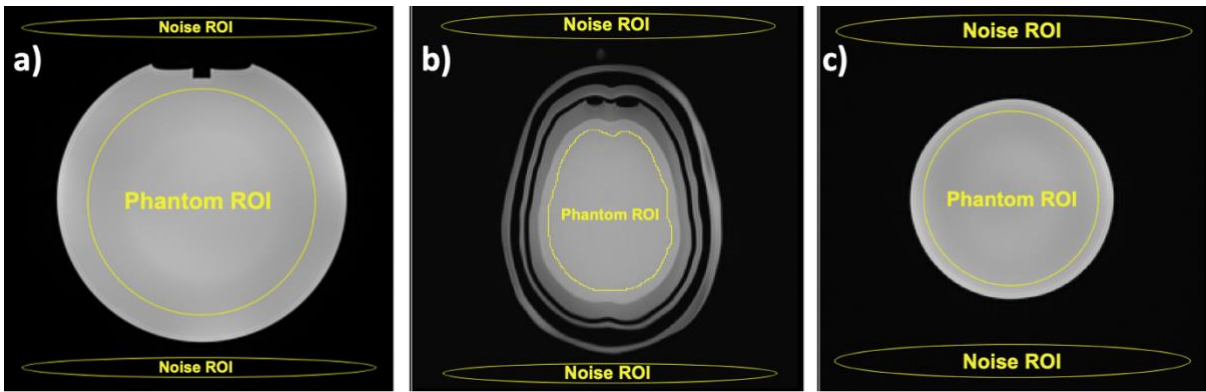
Figure 5-7 Axial images of the phantoms with ROIs drawn for SNR measurement. Central ROI for signal and Upper/Lower ROIs for noise calculation. A) ACR Phantom. B) Anthropomorphic phantom and C) homogeneous phantom

PIU was assessed by adjusting the window level to highlight a sparse number of the brightest pixels. The window level was then decreased to isolate a minimal number of the darkest pixels. Maximum and minimum intensity values were derived from two ROIs, which encompassed the bright and dark pixels following the window and level adjustments (see Figure 5-8).
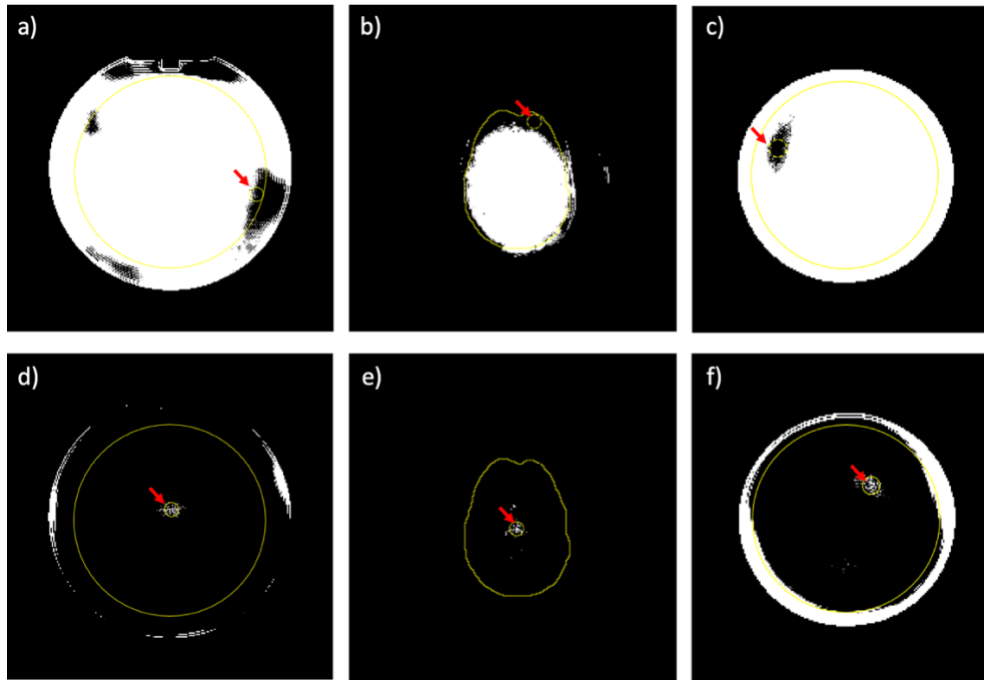
Figure 5-8 Axial images of the phantoms with ROIs drawn for PIU measurement. An ACR phantom (a, d), an anthropomorphic phantom (b, e), and a homogeneous phantom (c, f). The window and level settings are adjusted to reveal minimum signal areas as dark pixels (a-c) and maximum signal areas as bright pixels (d-f).

To measure PSG, four ROIs were outlined around the phantom (see Figure 5-9).

Table 5-4 shows all information related to the ROI sizes for SNR, PIU and PSG.
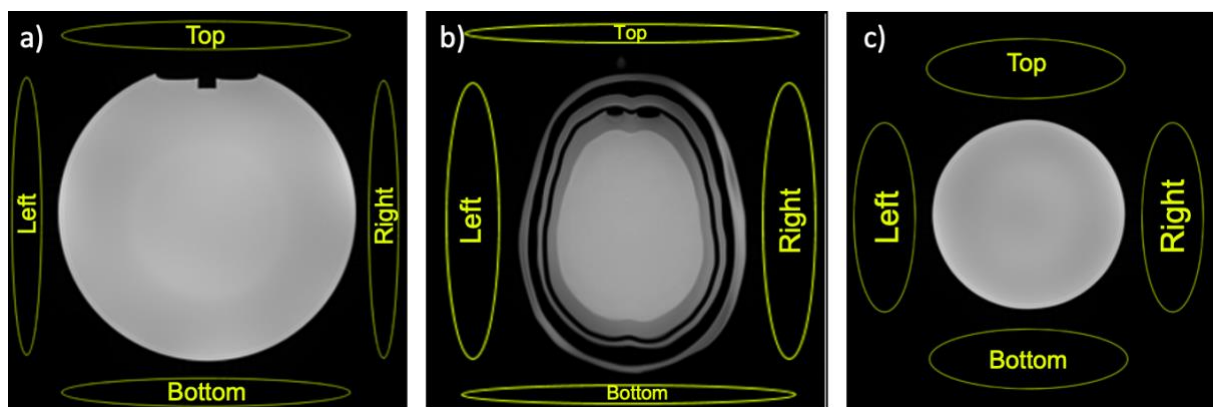
Figure 5-9 The four ROIs have been drawn around the phantom to calculate the PSG. A) ACR Phantom. B) Anthropomorphic phantom and C) homogeneous phantom

Table 5-4 methods used to delineate ROI on ACR, Anthropomorphic, and Homogeneous phantoms for the evaluation of MRI Quality Assurance parameters.

QA parameters		Phantoms		
		ACR	Anthro.	Homog.
Signal measurement	Region of interest centered on the phantom (cm²)	176.9	70.2	108.5
	Size of the phantom's cross-sectional area (cm²)	283.6	93.3	138.9
	proportion of the ROI to the phantom's cross-sectional (%)	62.4%	75.3%	76.2%
Standard deviation in the background measurement	Above (cm²)	23.8	22.8	40.88
	Below (cm²)	23.8	29.7	40.88
PIU measurement	Max and min ROI (cm²)	0.97		
	FOV area (cm²)	655.4		
	ROI coverage of the FOV (%)	0.15%		
PSG - ROIs were outlined around the phantom (cm²)	Top (cm²)	26.3	20.4	45.9
	Bottom (cm²)	26.3	20.4	45.9
	Left (cm²)	26.7	47.6	45.0
	Right (cm²)	26.7	47.6	45.0

Using information obtained from ROIs, the SNR, PIU and PSG were then calculated using Equation 5-1, Equation 5-2 and Equation 5-3 respectively.

$$SNR = \frac{\mu_{ROI}}{\sigma_{background}}$$

Equation 5-1

μ_{ROI} = the mean pixel value of region of interest (ROI) in the phantom

$\sigma_{background}$ = standard deviation of signal across voxels in the background ROI.

$$PIU = 100 \times \left(1 - \frac{S_{max} - S_{min}}{S_{max} + S_{min}}\right)$$

Equation 5-2

S_{max} and S_{min} = The maximum and minimum signal intensities, respectively.

$$PSG = 100 \times \left| \frac{(S_L + S_R) - (S_T + S_B)}{2S} \right|$$ **Equation 5-3**

S_L, S_R, S_T, and S_B = Signal intensities in the Left, Right, Top, and Bottom of an image's background, respectively

S = phantom signal intensity.

SNR, PIU and PSG were calculated for all 5 images for each phantom in each setup position. From these the coefficient of variation (CoV) was calculated between repeat scans with the same setup and varying setups using Equation 5-4 .

$$CoV = \frac{Standard\ Deviation\ (SD)}{Mean} \times 100$$ **Equation 5-4**

5.2.4 Artefact evaluation

The objective of artifact evaluation is to detect any anomalies in MRI images that could signify a degradation in the performance of the MRI system. Five scans per phantom obtained in Section 5.2.3, were used for this test. The images were analyzed according to the ACR guidelines (201). Display settings were adjusted for enhanced clarity, after which a bright area, distinguished by its higher pixel intensity, was chosen for small ROI measurement on each slice. Subsequently, the display window was set to this value, and the display level was adjusted to half of that value. Visual inspection of the images was performed to confirm the absence of ghost images, streaks, artefactual anomalies, and any new or unusual features.

Following the ACR guidelines (201), the circularity of the ACR and homogeneous phantoms was verified, excluding elliptical or other distortions. This procedure was not applicable to the anthropomorphic phantom due to its non-circular shape. Diameter measurements within phantoms were conducted using Fiji software.

Vertical, horizontal, and diagonal lines were drawn to intersect at the centre of the homogeneous phantom. For the ACR Phantom, the black area (air bubble) at the top prevented the vertical line from being drawn; therefore, only horizontal and diagonal lines were drawn (see Figure 5-10).
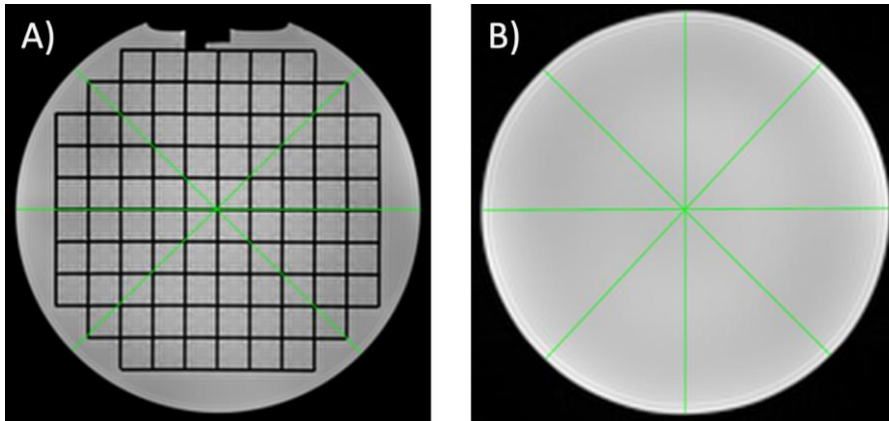
Figure 5-10 Lines drawn to evaluate the circularity of the phantom in the image A) Axial slice of ACR phantom shows the geometric accuracy grid with arrows indicating the three measured distances. B) slice number 6 of the homogeneous phantom with arrows indicating the four measured distances.

5.2.5 QA of RT accessories

The guidelines (16) recommend comparing the same sequence acquired both with and without RT accessories. However, the test's scope was broadened to compare RT and diagnostic radiology setups for brain/head anatomy to compare these two situations using the acquisition parameters in Table 5-3.

For all phantoms, the radiology setup is the same as discussed in section 5.2.1. For RT setup, an 18-channel flex coil was used due to its compatibility with RT accessories, and a flat couch was utilized. The ACR phantom was positioned with the NOSE facing anteriorly and the CHIN directed inferiorly, aligning it with the MRI scanner's lasers according to ACR guidelines (201). For the anthropomorphic phantom, the image acquisition was performed using a thermoplastic mask and headrest, with its graticules aligned to the MRI scanner's

lasers. For the homogeneous phantom, foam pads were used to ensure the phantom remained stable on the flat couch. The coil was then placed on the phantom, and the manufacturer's label was used as a marker for aligning the horizontal line with the MRI scanner's lasers.

Scans of both phantoms at each position were acquired three times with the same setup (Scans 1, 2, and 3), and two additional times with a varying setup (Scans 4 and 5). All images were imported into ImageJ2 (218) and both SNR and Percent PIU were calculated (201).

The images were analyzed as outlined in Section 5.2.3. Table 5-5 shows all information related to the ROI sizes for SNR and PIU.

Table 5-5 Methods used to delineate ROI on ACR, Anthropomorphic, and Homogeneous phantoms for the evaluation of SNR and PIU.

QA parameters		Phantoms		
		ACR	Anthro.	Homog.
Signal measurement	Region of interest centered on the phantom (cm²)	178.0	70.10	104.8
	Size of the phantom's cross-sectional area (cm²)	283.6	93.26	138.9
	proportion of the ROI to the phantom's cross-sectional (%)	63.5%	75.10%	75.4%
Standard deviation in the background measurement	Above (cm²)	29.3	21.5	65.8
	Below (cm²)	29.3	10.4	65.8
PIU measurement	Max and min ROI (cm²)	0.78		
	FOV area (cm²)	507.8		
	ROI coverage of the FOV (%)	0.15%		

SNR and PIU were calculated for all 5 images for each phantom in each setup position in the methods outlined in Section 5.2.3. From these the CoV was calculated between repeat scans with the same setup and varying setups.

5.2.6 Informatics, connectivity, and data transfer

This tests connectivity and data transfer to a TPS and a Picture Archiving and Communication System (PACS) ensuring error-free transmission of Digital Imaging and Communications in Medicine (DICOM) data. A turbo spin echo T1-weighted sequence, chosen for its short acquisition time, was acquired of ACR and anthropomorphic phantoms using the parameters in Table 5-3. The ACR phantom was positioned within a 20-channel H&N coil following ACR guidelines (201). The anthropomorphic phantom was positioned under an 18-channel flex coil aligning its graticules with the MRI scanner's lasers. An MRI-visible marker was positioned on the anthropomorphic phantom's right side for orientation identification. Following the IPEM guidelines (16), images were acquired for both phantoms with the patient orientation altered physically and on the MRI console as: head-first supine (HFS), feet-first supine, head-first prone and feet-first prone. DICOM data from all scans were imported into the TPS and PACS and both image orientation and DICOM tag accuracy, such as patient orientation, image acquisition parameters, and demographics, were manually verified against original acquisition data.

5.2.7 QA for MRI-CT registration

T1- and T2-weighted MRI images were acquired of ACR and anthropomorphic phantoms using parameters in Table 5-3. The T1-weighted image was acquired of the ACR phantom HFS under an 18-channel flex coil, on a flat couch with the NOSE anteriorly and CHIN inferiorly, with the MRI scanners lasers using the ACR guidelines (201). The 18-channel flex coil was chosen because it is compatible with RT accessories. IPEM guidelines (16) recommend testing both rotation and translation for registration effectiveness. They specify rotating the phantom up to 45 degrees but do not mention a range for translation. In this study, two T2-

weighted images were acquired, one with a 4 mm lateral left shift of the phantom and the other with a 32 degree right rotation. The anthropomorphic phantom T1-weighted image was acquired HFS under an 18-channel flex coil, on a flat couch with a thermoplastic mask and head rest aligning its graticules with the MRI scanner's lasers. For the T2-weighted acquisitions, the thermoplastic mask was used but released from the flat couch for the rotational adjustment. Two T2-weighted images were acquired, one with a 5 mm lateral left shift of the phantom and the other with a 10 degree right rotation. CT scans were acquired of both phantoms HFS with 120 kV, using 104 milliampere-seconds (mAs), with a resolution of 1.17×1.17×2 mm³ and a FOV of 600 mm as per Leeds Cancer Centre (LCC)'s clinical practice for treatment planning in H&N patients.

All CT/MRI datasets were imported into the TPS. The MRI was registered to CT using automatic rigid registration, with accuracy verified visually and quantitatively using Target Registration Error (TRE) and Dice Similarity Coefficient (DSC). Landmarks for TRE calculations were manually identified on the pre-registered MRI and CT scans, chosen for their visibility in both modalities (see Figure 5-11 and Figure 5-12). Post-registration, the MRI landmarks were transposed onto CT and TRE was calculated using Equation 5-5.

$$TRE = \sqrt{(X_{MRI\,to\,CT} - X_{CT})^2 + (Y_{MRI\,to\,CT} - Y_{CT})^2 + (Z_{MRI\,to\,CT} - Z_{CT})^2} \qquad \textbf{Equation 5-5}$$

$X_{MRI\,to\,CT}$, $Y_{MRI\,to\,CT}$, $Z_{MRI\,to\,CT}$ = The coordinates of the landmarks in the MRI after they have been transformed to align with CT images.

X_{CT}, Y_{CT}, Z_{CT} = The coordinates of the landmarks in the CT image dataset.

For DSC analysis, a cylindrical ROI on the ACR phantom and a whole-brain ROI on the anthropomorphic phantom were contoured on both CT and the laterally shifted MRI (Figure 5-11 and Figure 5-12). Structures were not contoured on the

rotated MRI because with a large rotation the structures appear notably different, making it challenging to accurately delineate specific ROIs. Post-registration, MRI contours were transposed onto CT and DSC was calculated using Equation 5-6.

$$DSC = \frac{2 \times |A \cap B|}{|A| + |B|}$$ **Equation 5-6**

A and B = The binary segmentation masks of the same structure in the MRI and CT images.
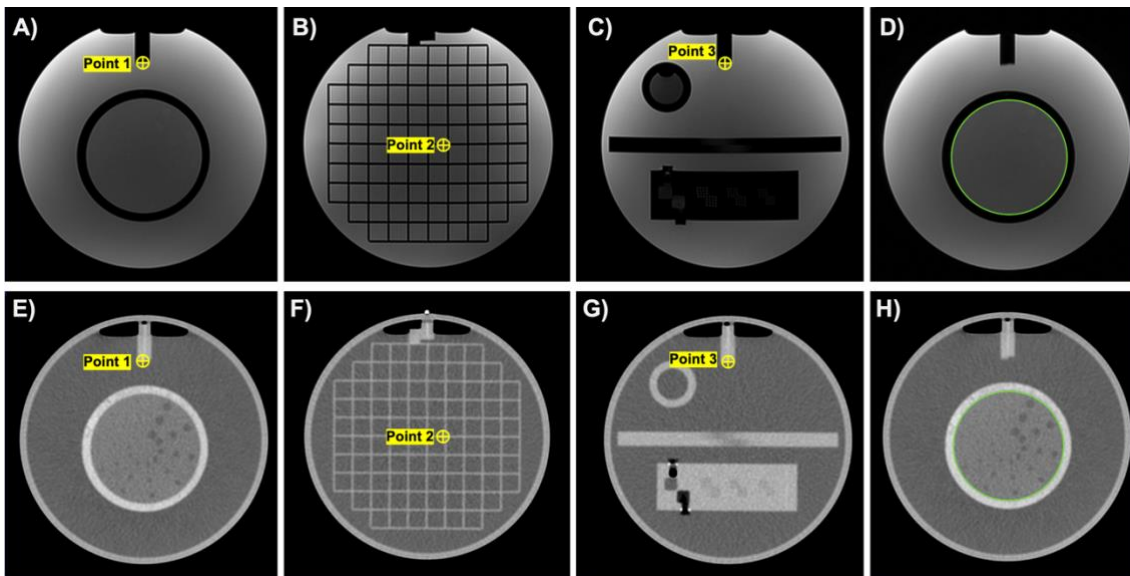
Figure 5-11 Evaluation of Imaging Registration Using ACR phantom. (A-D) MRI images: (A-C) highlighting landmarks used for TRE and (D) shows the ROI used for DSC. (E-H) Corresponding CT slices of MRI: (E-G) display landmarks used for TRE, and (H) shows the ROI used for DSC.
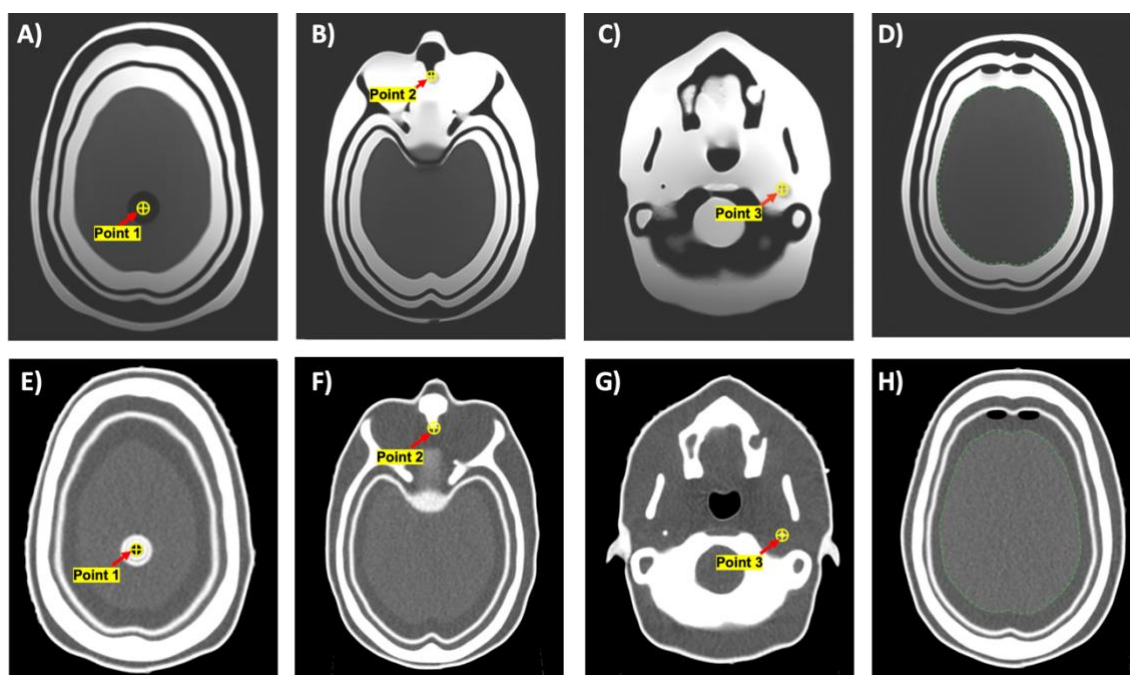
Figure 5-12 Evaluation of Imaging Registration Using Anthropomorphic phantom. (A-D) MRI images: (A-C) highlighting landmarks used for TRE and (D) shows the ROI used for DSC. (E-H) Corresponding CT slices of MRI: (E-G) display landmarks used for TRE, and (H) shows the ROI used for DSC

5.2.8 End-to-end QA

For both ACR and anthropomorphic phantoms a GTV was defined as the cylinders shown in Figure 5-13 on the T2-weighted MRI acquired in section 5.2.7. In the anthropomorphic phantom, the GTV was contoured around the ionization chamber space. For the ACR phantom, it was contoured within a clearly visible circular structure in the phantom. These GTVs were grown to a CTV and Planning Target Volume (PTV) following our local H&N protocol. Organs at risk (OARs) were not outlined on the ACR phantom because it lacks human-like structures, making it impossible to approximate the location of these organs. For the anthropomorphic phantom OARs (eyes and brainstem) were contoured as the phantom's human-like design allowed for their estimation. All structures contoured on MRI were copied onto the relevant CT scans.
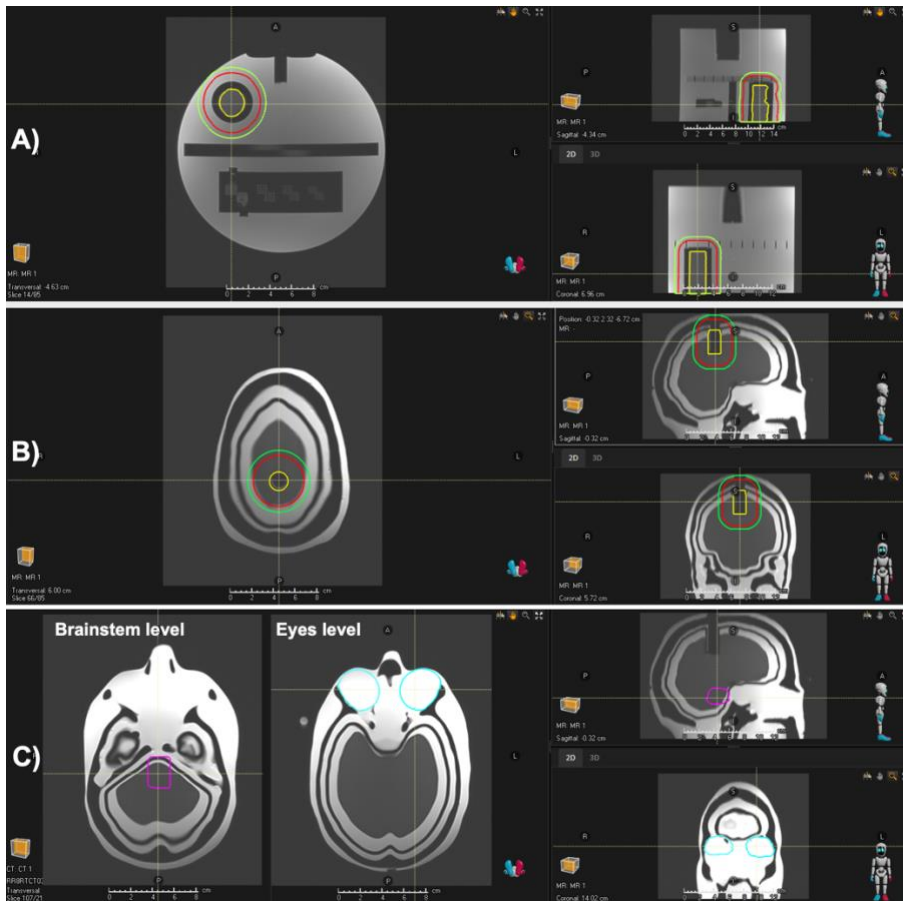
Figure 5-13 T2-Weighted MRI Imaging and ROI Visualization for Treatment Planning. A) ACR phantom, B) anthropomorphic phantom, both with outlined target areas: Gross Tumour Volume (GTV) (yellow), Clinical Target Volume (CTV) (red), and planning target volume (PTV) (green). C) The same anthropomorphic phantom highlighting OARs; the eyes (light blue), and the brainstem (purple).

For both phantoms a 6MV flattening filter-free plan was produced using our local treatment planning protocol. A single 360 degree arc Volumetric Modulated Arc Therapy (VMAT) plan was created, prescribing 2 Gy to the PTV in 1 fraction. Table 5-6 shows the summary dose statistics for target volumes (GTV, CTV, and PTV) and external contours within the ACR and anthropomorphic phantoms, along with the dose to OARs in anthropomorphic phantom. The plans and contours were reviewed by a Medical Physics Expert (MPE).

Table 5-6 Comprehensive Dose Distribution for targets (GTV, CTV, and PTV) and external contours of the ACR and the anthropomorphic phantom, including OARs (left and right eyes, and brain stem) for the anthropomorphic phantom.

Phantom	ROI	Dose (Gy)						
		D99	D98	D95	Mean	D50	D2	D1
ACR	GTV	1.98	1.98	1.99	2.01	2.01	2.03	2.03
	CTV	1.97	1.98	1.98	2.00	2.00	2.03	2.03
	PTV	1.93	1.95	1.97	2.00	2.00	2.04	2.04
	External	0	0	0	0.28	0.14	1.99	2.01
Anthro	GTV	2.00	2.01	2.01	2.03	2.03	2.05	2.06
	CTV	1.97	1.98	1.98	2.01	2.01	2.06	2.06
	PTV	1.93	1.94	1.96	2.00	2.00	2.05	2.06
	Left eye	0.03	0.03	0.03	0.04	0.04	0.06	0.06
	Right eye	0.03	0.03	0.03	0.04	0.04	0.06	0.06
	Brain stem	0.03	0.03	0.03	0.04	0.04	0.07	0.07
	External	0.03	0.03	0.03	0.04	0.04	0.06	0.06

Treatment plans, structures and CT scans were exported to Mosaiq version 2.81 (Elekta, Stockholm, Sweden). Both phantoms were setup on a linac using the methodology described in section 5.2.7. A CBCT scan was acquired with Elekta XVI (Elekta, Stockholm, Sweden) with parameters: 120 kV, 1x1x1 mm³ resolution, a S20 kV collimator and 20 second exposure time with an X-ray tube current of 20 mA. An automated rigid registration of CBCT to reference CT images was performed and qualitatively assessed by an MPE specialising in RT imaging. Assessment focused on alignment of external structures and the internal grid of the ACR phantom, and on bony landmarks for the anthropomorphic phantom.

The test ended here for the ACR phantom due to the inability to measure radiation dose. For the anthropomorphic phantom the treatment plan was delivered with a TW31010 semiflex ionization chamber (PTW, Freiburg, Germany) with a sensitive volume of 0.125 cm³ positioned within the phantom. The charge

collected in the chamber was measured with a UNIDOS electrometer (PTW, Freiburg, Germany). The calibration factor, determined to be 3.446 nC/Gy accounting for radiation energy, environmental conditions, and the characteristics of the chamber used. The collected charge was then converted into absorbed dose. In the plan, a volume of the same size as the chamber was created to calculate the mean calculated dose, which was compared to the measured dose.

To further investigate the discrepancy between the planning and delivery of RT, the mass densities of the materials used in the phantom were independently measured and compared to the mass densities predicted by the CT-to-mass density conversion curve used by the TPS to evaluate the curve's applicability for the materials used in the anthropomorphic phantom. Five cubic samples (2×2×2 cm³) of lung and bone materials, as well as three irregularly shaped samples of brain material, were produced. The mass of each sample was measured using a balance, and the mass density was calculated by dividing the measured mass by the sample volume. For all materials, the mean mass density of the samples was calculated and then compared to the densities predicted by the CT-to-mass density conversion curve.

5.3 Results

5.3.1 Magnetic Field Drift Test

Figure 5-14 shows the mean and standard deviation of the central frequency in the experiments carried out with all the phantoms.
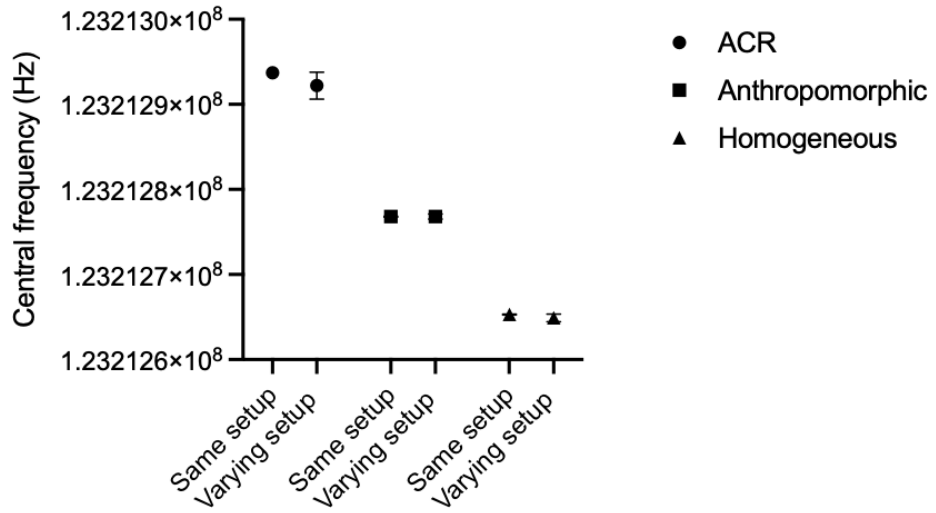
Figure 5-14 The mean central frequency values (in Hz) and their standard deviations for all phantoms under both same setup and varying setup conditions.

Figure 5-15 shows the CoV between the central frequency values obtained within each phantom. The CoV for the ACR phantom is higher than those for both the anthropomorphic and homogeneous phantoms in both the same and varying setups.
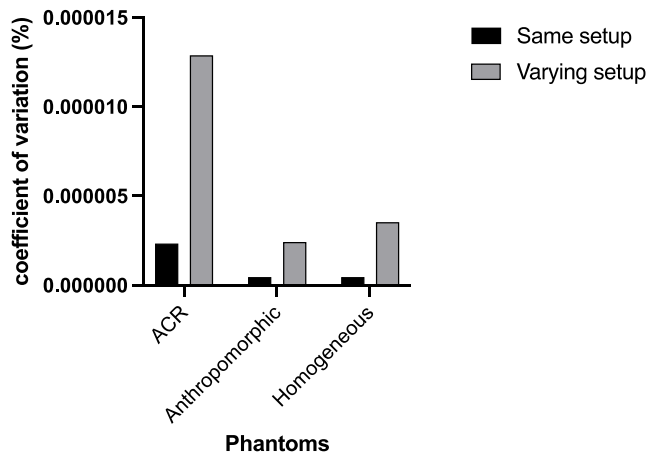
Figure 5-15 The CoV between the central frequency values obtained from each phantom.

5.3.2 Transmitter and Gain Calibration

Figure 5-16 shows the mean and standard deviation of the transmitter gain values determined automatically in the experiments carried out with all the phantoms.
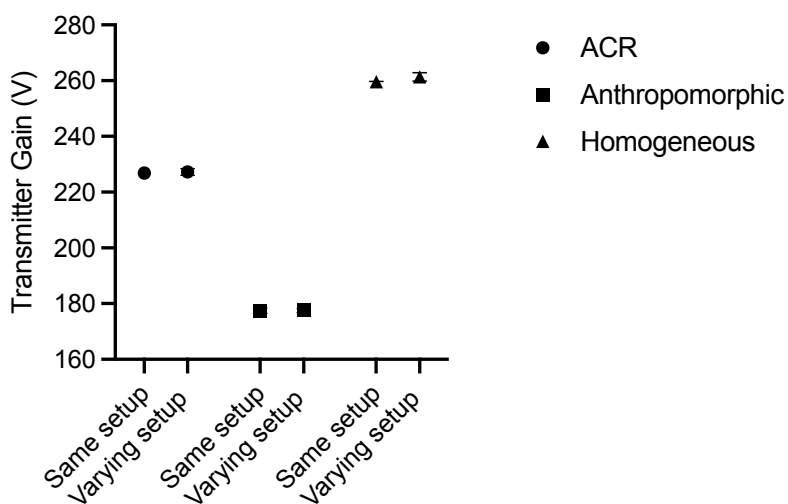
Figure 5-16 The mean transmitter gain values and their standard deviations for all phantoms, under both same setup and varying setup conditions.

Figure 5-17 shows the CoV between the transmitter gain values determined automatically obtained from each phantom. Under the same setup, the anthropomorphic phantom displays a higher CoV for Transmitter Gain than the ACR and homogeneous phantoms.
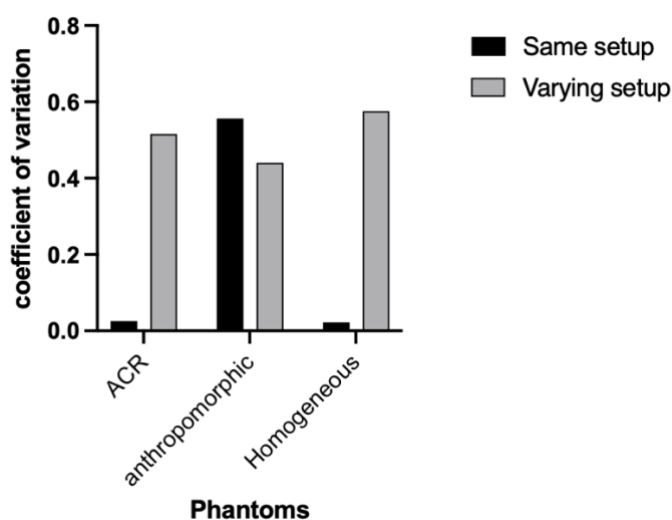
Figure 5-17 The CoV between the Transmitter Gain values obtained within each phantom.

Table 5-7 shows a comparison between automatic transmitter gain and manual transmitter gain obtained within each phantom. Only the homogeneous phantom's results were within the defined action limit ±5%, while the ACR and anthropomorphic phantoms show deviations that exceed the acceptable range indicating their unsuitability for clinical applications.

Table 5-7 Automated and manual transmitter gain values and the percentage difference between them for all phantoms (Experiment with anthropomorphic phantom conducted once only for feasibility due to lengthy procedure).

Phantom	Gain	Same setup			Varying setup	
		1	2	3	4	5
Homogeneous	Auto transmitter gain	259.6	259.7	259.7	262.1	262.3
	Manual transmitter gain	263.2	263.5	263.5	264.8	263.0
	Difference	**1.4%**	**1.5%**	**1.5%**	**1%**	**0.3%**
ACR	Auto transmitter gain	226.8	226.9	226.8	226.4	228.6
	Manual transmitter gain	240.3	240.2	240.0	240.5	240.3
	Difference	**6%**	**5.6%**	**5.8%**	**6%**	**5.1%**
anthropomorphic	Auto transmitter gain	177.9				
	Manual transmitter gain	195.5				
	Difference	**9.4%**				

5.3.3 Radiofrequency Coil Evaluation

Table 5-8 shows the SNR, PIU, and PSG for all phantoms in the same setup and varying setup. To determine whether a SNR value is acceptable, it must be compared to the established action limits. PIU values for all phantoms were greater than 82%, and PSG values for all phantoms were less than 2.5% and therefore, the results for all phantoms fall within the acceptable range.

Table 5-8 MRI image parameter measurements (SNR, PIU, and PSG) for three phantoms (ACR, anthropomorphic and homogeneous) under same setup and varying setup conditions.

Phantom	scan		SNR	PIU (%)	PSG (%)
ACR	Same setup	1	996.0	92.3	0.074
		2	966.0	92.4	0.068
		3	1001.2	92.4	0.076
	Varying setup	4	941.1	92.7	0.090
		5	956.1	92.6	0.077
anthropomorphic	Same setup	1	1215.5	94.6	0.095
		2	1175.9	94.6	0.090
		3	1200.2	94.6	0.093
	Varying setup	4	1221.9	94.2	0.090
		5	1228.2	94.4	0.090
homogeneous	Same setup	1	1121.8	94.7	0.026
		2	1116.2	94.6	0.020
		3	1118.0	94.7	0.018
	Varying setup	4	1145.1	94.7	0.025
		5	1104.9	94.7	0.020

Figure 5-18 illustrates the CoV in the results of SNR, PIU, and PSG for each phantom under same setup and varying setup conditions. The anthropomorphic phantom generally has a lower CoV compared to the ACR phantom across SNR, PIU, and PSG measurements.
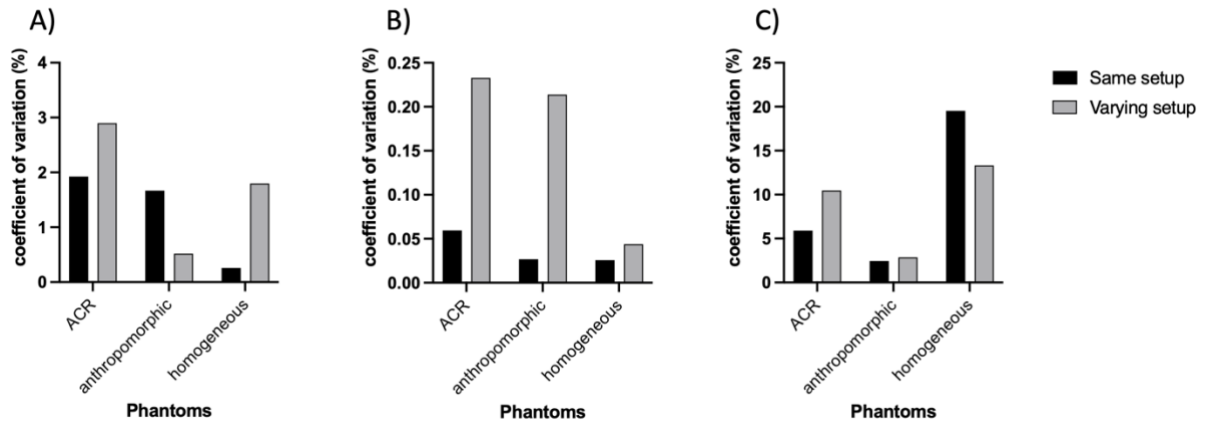
Figure 5-18 The CoV between the results of the A) SNR, B) PIU and C) PSG of each phantom.

5.3.4 Artefact evaluation

Figure 5-19 shows images of the phantoms used in this study conforming to ACR guidelines (201). The images clearly depict the phantoms maintaining their shapes without distortion. Free from any ghosting, overlaying effects, streaks, artifactual brightness or darkness, and anomalous features.
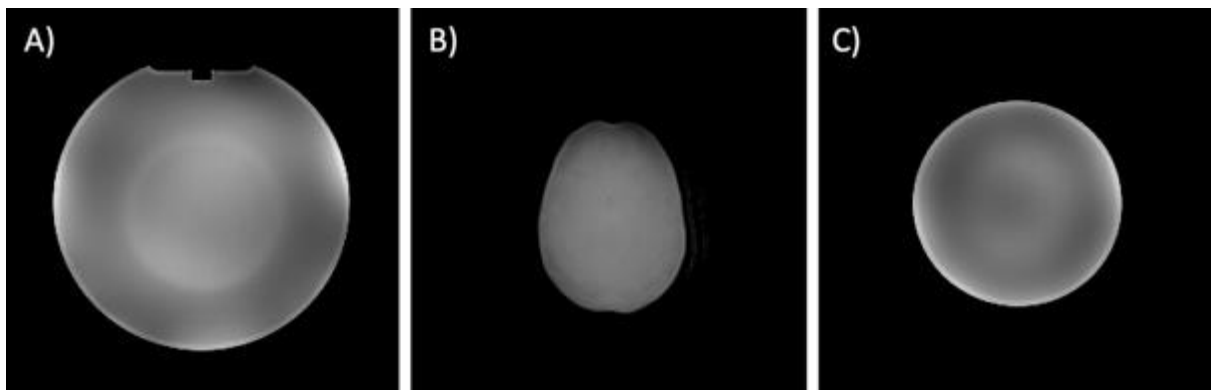
Figure 5-19 Phantom images of A) ACR, B) anthropomorphic and C) Homogeneous phantoms after adjusting the image display according to the recommendations of the ACR in order to assess for artefact.

Table 5-9 details the dimensions of the ACR and Homogeneous phantoms. Measurements are considered acceptable when they fall within ±2 mm of the actual values (201). The measurements for the ACR phantom range from 190.4

to 190.6 mm, and for the Homogeneous phantom from 133.1 to 134.0 mm, suggesting circularity within these tolerances.

Table 5-9 Measurements of different oriented lines in ACR and Homogeneous phantom

Phantom setup	Experiment number	Lines measurement (mm)							
		horizontal		vertical		diagonal (top right to bottom left)		diagonal (top left to bottom right)	
		ACR	Homo.	ACR	Homo.	ACR	Homo.	ACR	Homo.
Same setup	1	190.5	133.6	Not measured	133.3	190.4	133.7	190.4	133.4
	2	190.6	133.7		133.2	190.6	133.3	190.4	133.9
	3	190.4	134.0		133.1	190.4	133.6	190.5	133.3
Varying setup	4	190.4	133.9		133.5	190.5	133.6	190.6	133.7
	5	190.4	134.0		133.1	190.4	133.5	190.5	133.4

5.3.5 QA of RT accessories

Table 5-10 shows the SNR and PIU obtained from scans of three phantoms. Each phantom was evaluated using both an 'RT setup' and a 'Diagnostic Radiology setup'.

Table 5-10 Image Quality parameters (SNR and PIU) for ACR, anthropomorphic and Homogeneous phantoms measured both with and without RT accessories. Each phantom was scanned using both a 'Same setup' and a 'Varying setup'. The difference columns provide a comparison between the values obtained with and without the use of accessories.

Phantom	scan		SNR			PIU		
			Radiology setup	RT setup	Difference (%)	Radiology setup	RT setup	Difference (%)
ACR	Same setup	1	188.9	152.3	-19.4	69.2	62.3	-10.0
		2	189.1	149.5	-20.9	69.1	62.2	-10.0
		3	185.4	149.9	-19.1	69.2	62.1	-10.3
	Varying setup	4	184.8	146.6	-20.7	69.5	64.4	-7.3
		5	184.0	147.2	-20.0	69.0	62.0	-10.1
anthropomorphic	Same setup	1	177.6	131.5	-26.0	93.6	66.4	-29.1
		2	179.0	133.5	-25.4	93.5	66.5	-28.9
		3	176.8	133.4	-24.5	93.5	66.3	-29.1
	Varying setup	4	180.0	127.6	-29.1	93.6	72.2	-22.9
		5	177.2	115.7	-34.7	94.0	70.8	-24.7
Homogeneous	Same setup	1	111.0	106.2	-4.3	79.7	51.6	-35.3
		2	111.0	104.5	-5.9	79.5	52.0	-34.6
		3	111.3	104.1	-6.5	79.0	51.6	-34.7
	Varying setup	4	111.4	106.7	-4.2	78.4	51.2	-34.7
		5	111.7	106.7	-4.5	79.0	52.0	-34.2

Figure 5-20 shows the CoV between the results for SNR and PIU for each phantom using RT setup and radiology setup under same setup and varying setup conditions. The anthropomorphic phantom demonstrates a lower CoV in the SNR and PIU measurements compared to the ACR phantom, in both the same and varying setups using radiology setup. Moreover, it also shows a lower CoV in these measurements in the same setup using the RT setup. The CoV for the homogeneous phantom's SNR measurements using the RT setup was higher in the same setup than in varying setups.
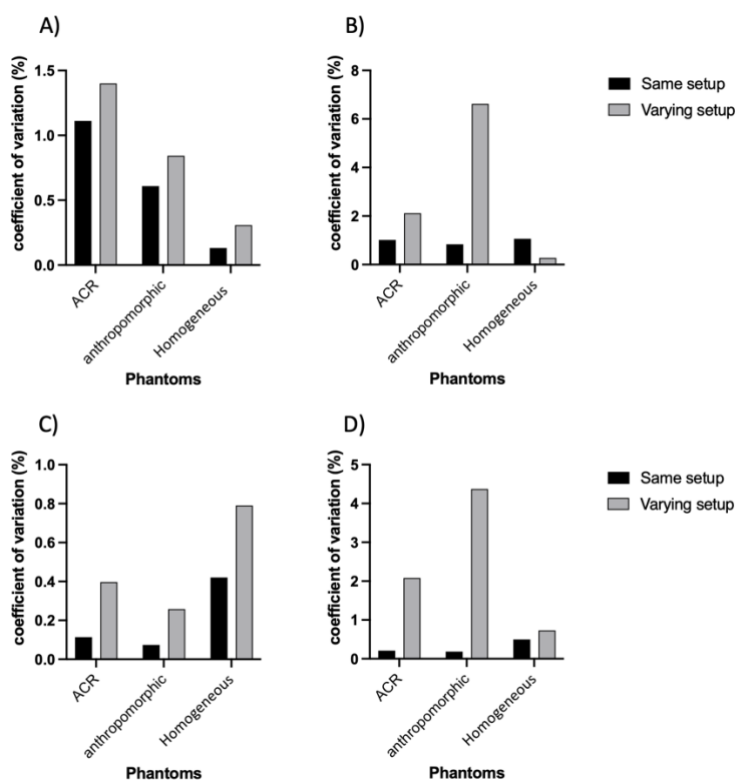
Figure 5-20 The CoV between the results. (A-B) The CoV of SNR: (A) without RT accessories and (B) using RT accessories. (C-D) The CoV for the PIU: (C) without RT accessories, and (D) using RT accessories.

5.3.6 Informatics, connectivity and data transfer

The test for DICOM data transfer using ACR and anthropomorphic phantoms showed successful results. Both phantoms' orientation were accurately identified in the TPS and PACS, with DICOM tags consistent across all orientations. This confirms the accuracy of the data transfer process in clinical applications.

5.3.7 QA for MRI-CT registration

Image registration quality was assessed visually and no registration errors were observed. The anthropomorphic phantom had limited structures/landmarks for quantitative assessments compared to the ACR phantom. Table 5-11 shows the TRE results, all results were less than the minimum voxel dimension, approximately 0.97 mm. This means that the image registrations for both phantoms were acceptable according to the guidelines [4]. DSC values were all

greater than 0.9 (see Table 5-11), which made registration acceptable according

to the guidelines (16).

Table 5-11 Target registration error (TRE) for the three points and the mean value, as well as Dice Similarity Coefficient (DSC) for American College of Radiology (ACR) and anthropomorphic phantoms.

Phantom	Sequence	TRE for the three points in (mm)			mean of TRE	DSC
		1	2	3		
ACR	T1	0.08	0.13	0.11	0.11	0.94
	T2 with 4mm left shift	0.08	0.15	0.15	0.12	0.94
	T2 with 32° rotation	0.10	0.20	0.20	0.17	-
Anthro	T1	0.09	0.11	0.12	0.11	0.96
	T2 with 5mm left shift	0.10	0.13	0.12	0.12	0.95
	T2 with 10° rotation	0.10	0.18	0.02	0.10	-

5.3.8 End-to-end QA

The CBCT images showed that the positions of the ACR and anthropomorphic

phantoms aligned well with their planned treatment setups, all within clinically

acceptable tolerances based on standard qualitative assessment criteria used in

the clinic. The anthropomorphic phantom enabled radiation dose measurements.

The dose measured in the semiflex chamber was 1.994 Gy, compared to the

calculated mean dose of 2.01 Gy, indicates a dose difference of -0.8%.

Table 5-12 shows the CT numbers, CT-derived mass densities, and measured

mass densities for the brain, bone, and lung materials used in the

anthropomorphic phantom. These results suggest that the CT calibration curve

is applicable for the materials used in the anthropomorphic phantom as the

predicted and measured mass densities for brain, bone, and lung closely align.

Table 5-12 Comparison of CT-derived mass densities and measured mass densities for materials used in the anthropomorphic phantom.

Material	CT number (HU)	CT-derived mass density (g/cm³)	Measured Mass Density (g/cm³)
Brain	32	1.022	1.020
Bone	509	1.356	1.353
Lung	-765	0.235	0.235

5.4 Discussion

This study represents the first evaluation of a multimodality anthropomorphic phantom for the QA tests for MRI in RT proposed by the AAPM and IPEM guidelines (16, 17), comparing its performance with the well-established ACR phantom. The hypothesis was that anthropomorphic phantoms, due to them being more representative of clinical scenarios, could enhance the accuracy and effectiveness of QA tests compared to other phantoms. The following sections will critically evaluate each MRI QA test, focusing on the efficacy of anthropomorphic phantoms in RT contexts. Each test will be discussed in turn, concluding with an overall findings section that includes some recommendations.

5.4.1 Magnetic Field Drift Test

In principle, acceptance testing is recommended at installation, followed by re-testing after 1–2 months (17). General acceptance testing data for the scanner are stored, but data for this specific test methodology were not available, particularly with the use of all three phantoms under the described methods. The primary objective of this study was to evaluate the phantom by measuring the absolute central frequency (Hz) and CoV to assess variability, rather than to assess scanner performance. If baseline acceptance-testing data specific to this methodology were available, central frequency deviation (in ppm) could have been calculated using Equation 5-7

$$Central\ frequency\ deviation\ (ppm)$$
$$= \frac{central\ frequency\ (Hz) - initial\ frequency\ (Hz)}{Larmor\ frequency\ (MHz)}$$

Equation 5-7

It was possible to measure the central frequency value of the anthropomorphic phantom. In terms of the CoV, the anthropomorphic phantom performed as well as the homogeneous phantom and better than the ACR phantom. The ACR phantom is more complex and contains more structures used for various QA tests compared to the homogeneous and anthropomorphic phantoms. This may have led to a slightly different susceptibility across the phantom, leading to small shifts in the resonance frequency of hydrogen atoms thus the strength of the magnetic field (219).

5.4.2 Transmitter and Gain Calibration

A failed Transmitter Gain test can cause artifacts like "zipper" or ghost images, reduce SNR, create non-uniform signals, and lead to inaccurate flip angles, negatively affecting image quality and advanced imaging techniques (200). The ACR and anthropomorphic phantoms exhibited inadequate performance in the transmitter and gain calibration QA test. According to guidelines (17, 200) the difference between the auto transmitter gain and the manual transmitter gain must be within ±5%. Only the homogeneous phantom demonstrated a difference within ±5% between the automatic and manual transmitter gains, whereas the differences for the other two phantoms exceeded this range. Since the homogeneous phantom is the recommended one by guidelines and considered the gold standard for this test, its results are deemed more reliable. The prolonged T1 relaxation time in the anthropomorphic phantom contributes to extended test durations. In conclusion, the ACR and anthropomorphic phantoms

are deemed suboptimal for this QA test, with the homogeneous phantom emerging as a more reliable choice.

To determine the gain, the adjustment volumes used encompassed a large part of the ACR and anthropomorphic phantoms. This means they included structures made of different materials in each phantom. It is possible that choosing only a uniform area for shimming in the ACR phantom and anthropomorphic phantom could have led to results similar to those obtained with the homogeneous phantom.

5.4.3 Radiofrequency Coil Evaluation

The anthropomorphic phantom appears to be suitable for SNR, PIU, and PSG tests. However, drawing ROIs for the ACR and the homogeneous phantom is relatively straightforward, typically involving basic shapes like circles. In contrast, the anthropomorphic phantom, embodying the complexity of the human anatomy, necessitates a more intricate approach for ROI delineation especially for accurately contouring a large proportion of the brain's area in for SNR analysis as recommended for other phantoms (200). Automating the analysis process by writing a script that automatically generates structures can solve this issue, making the phantom image analysis more objective, repeatable, and time-efficient.

The results of the CoV showed that the anthropomorphic phantom demonstrates slightly lower variability compared to the ACR phantom across all experiments. This suggests that the anthropomorphic phantom's performance is comparable to that of the ACR phantom. However, it is essential to recognize that changes in imaging properties of phantom material over time and after radiation exposure can impact MRI image quality parameters. Therefore, assessing their long-term and post-radiation stability is necessary. The stability of the polyvinyl alcohol

cryogel (PVA-c) material, from which the brain in the anthropomorphic phantom is made, was evaluated in Chapter 4.

The CoV results showed that the anthropomorphic and homogeneous phantom were more consistent at measuring the SNR and PSG respectively in varying setups than at measuring them in the same setup. Although these results may seem unexpected, it is important to acknowledge that the observed discrepancies in SNR and PSG measurements obtained from the phantoms were minimal. These slight variations could be attributed to experimental variability and the limited sample size, both of which may have influenced the outcomes.

In slice 7 of the ACR phantom, a black rectangular structure used for supporting slice positioning wedges hinders the drawing of a circle that covers 75% of the volume for SNR measurement, as recommended by ACR. This is because the structure, or at least its edge effects, cannot be excluded without positioning the ROI off-centre.

5.4.4 Artefact evaluation

No artifacts were observed with any of the phantoms. The ACR phantom requires evaluation of whether it appears circular and not distorted by geometric distortion. It was not possible to do this with the anthropomorphic phantom because it is not circular. However, for RT purposes this requirement can be waived as there is a comprehensive test for geometric distortion which none of these phantoms are optimised for. It is hypothesized that the use of an anthropomorphic phantom may be more appropriate for assessing artefacts. The rationale behind this hypothesis is that the anthropomorphic phantom could mimic artefacts produced as a result of the human body's characteristics, such as the presence of an air cavity and susceptibility artifacts (220). However, the findings from this study do not definitively establish the superiority of the anthropomorphic phantom in this test.

5.4.5 QA of RT accessories

The difference in SNR and PIU between the RT setup with accessories and the diagnostic radiology setup was evaluated using both phantoms. The ACR phantom, due to its cylindrical design, is incompatible with RT accessories like the thermoplastic mask and headrest, which are designed for human anatomical contours. Thus, the anthropomorphic phantom results give a more representative result of the patient situation when performing QA of RT accessories, compared to the ACR phantom.

The percentage differences in SNR and PIU varied depending on the phantom used and whether acquisition where in the radiology or RT setup. This variation is likely due to changes in coil setup, differences in phantom size and FOV, and the type of material scanned. The anthropomorphic phantom, designed to closely mimic human anatomy, offers a more realistic assessment of how RT accessories impact MRI imaging across different tissue types, including both soft tissues and bone. The CoV of percentage differences for SNR and PIU between scans with and without RT accessories showed that the ACR phantom was more consistent in measuring these metrics across varying setups. Considering absolute numbers, these differences were negligible.

In this study, the difference in SNR between RT and diagnostic radiology setups in the ACR phantom ranged from 19.1 to 21.0%, and the anthropomorphic phantom varied from 24.6% to 34.7%. The difference in SNR between RT and diagnostic radiology setups arises primarily from the setup differences. Specifically, in RT setups, the coil is positioned further from the phantom or patient to accommodate RT accessories, leading to a reduction in SNR. Regarding the differences between the ACR phantom and the anthropomorphic phantom, the variability in SNR is due to the differing properties of the phantoms.

Winter et al. (221) analyzed MRI SNR in head-and-neck cancer patients, finding a 26.2% reduction in SNR in the RT setup compared to the diagnostic radiology setup. Therefore, the anthropomorphic phantom's results in this study were most similar to the reduction published in patients' data. A further benefit of the anthropomorphic phantom for assessing RT accessories is that it allows the localisation of differences to be represented in an anatomical meaningful way. Whereas assessing the localisation of these differences on the ACR phantom is more abstract from patients' anatomy.

5.4.6 Informatics, connectivity and data transfer

Both phantoms were suitable for assessing connectivity and data transfer. However, while the ACR phantom has distinct internal structures to identify the left and right sides, the anthropomorphic phantom required an external marker for this purpose. However, the anthropomorphic phantom's human-like appearance simplifies determining its orientation.

5.4.7 QA for MRI-CT registration

Image registration quality was assessed both qualitatively and quantitatively. Qualitatively, the process was similar for both phantoms with no notable differences. Quantitatively, the ACR phantom has numerous points and structures that are visible in both MRI and CT images, facilitating the measurement of TRE and DSC, compared to the anthropomorphic phantom. The CIRS model 603A phantom (Norfolk, VA, USA) is an anthropomorphic skull phantom that can be imaged with CT and MRI (126) imaging, it assesses MRI distortion and verifies image registration algorithms. Though not anatomically accurate, a 3D grid inside the cranium helps evaluate spatial distortion in MR images. The presence of non-human anatomical features in the ACR and model 603A phantoms provides evenly distributed landmarks that do not reflect the

natural variability found in clinical anatomy. In real-world scenarios, anatomical structures are irregular and less uniformly distributed, which makes image registration more challenging. The simplified, regular features of these phantoms make the registration task easier and do not fully capture the complexities of actual patient imaging (222)

5.4.8 End-to-end QA

The anthropomorphic phantom provided a more representative basis for treatment planning, allowing for more appropriate simulated treatment targets and OARs, which was challenging with the ACR phantom. It also enabled a comparison between planned and measured doses. In this study, the difference between the calculated and measured dose in the anthropomorphic phantom was -0.8%, within the acceptable range of ±3% set out in the AAPM's TG-218 report (213).

One potential hypothesis for this discrepancy was that the CT calibration curve may not be applicable to the materials in the phantom. However, this hypothesis was ruled out based on the close alignment between the predicted and measured mass densities. Discrepancies can arise from calibration errors, phantom setup, detector response, and environmental conditions (223). Further work is needed to assess reproducibility. It is recommended that the phantom be tested multiple times across different linacs with various treatment plans to analyse result consistency and determine if any systematic errors are present.

Three commercially available multimodality phantoms were identified for end-to-end testing: the Stereotactic End-to-End Verification Phantom (STEEV) (CIRS Inc., Norfolk, VA, USA) (130), the LUCY™ MR phantom (Standard Imaging, Middleton, WI, USA) (134), and the Prime head phantom (RTsafe, Artotinis, Greece) (135). While the STEEV phantom is MRI-compatible for assessing

geometric distortion and image registration, parts like the brain do not produce realistic signals. LUCY™ MR images show the brain and soft tissues as a single structure, unlike the distinct separation seen in human imaging. Although the Prime head phantom has an anthropomorphic external shape, its internal structure lacks detailed features, such as air spaces and vertebrae.

5.4.9 Overall Findings

This study highlights that multimodality anthropomorphic phantoms are crucial for comprehensive end-to-end testing, offering advantages over the ACR phantom. While the ACR phantom is generally considered suitable for tasks such as QA of RT accessories, informatics, connectivity and data transfer, artefact evaluation, and QA for MRI-CT registration, the anthropomorphic phantom, owing to its more human-like structure, is more appropriate for all of these tasks. However, for magnetic field drift and radiofrequency coil evaluation, the anthropomorphic phantom does not offer any added benefits over the ACR phantom. Furthermore, both the ACR and the anthropomorphic phantom is not suitable for transmitter and gain calibration, as evidenced by the experimental data.

One limitation of this study is the variability among anthropomorphic phantoms, phantoms may represent different anatomies, be designed or printed based on data from different patients or have varying levels of anatomical realism. This variation makes standardization of QA challenging and complicates the generalizability of results. Commercial solutions could standardize anthropomorphic phantoms, mitigating these challenges.

To evaluate the effectiveness of registration software in processing images with unintentional shifts, the phantoms were subjected to different amounts of lateral shifts, the anthropomorphic phantom by 5 mm and the ACR phantom by 4 mm. Although the difference in shift is minor, identical movement for both phantoms

would have enhanced study consistency. Additionally, IPEM guidelines (16) recommend acquiring MRI images with the phantom oriented at angles up to 45 degrees. In this study, the ACR phantom was rotated 32 degrees and the anthropomorphic phantom 10 degrees, the latter being the maximum rotation physically achievable. Ideally, both phantoms should have been tested with a consistent angle for a more uniform evaluation.

The phantom used in this study is not a commercial solution and has some limitations that future phantoms could improve upon. Current radiation dose measurements are confined to a single location within the brain, adding measurement capability in the neck would increase the utility of the phantom to include end-to-end testing for H&N cancers. Redesigning the phantom's brain to better mirror human complexity by creating distinct regions of white and gray matter could increase confidence of image registration QA for the clinical scenario. However, the latter would compromise performance in other QA tests requiring homogeneous material.

5.5 Conclusion

This study assessed the suitability of a multimodality anthropomorphic phantom, compared to other types of phantoms, for QA specific to MRI use in RT for the first time. The anthropomorphic phantom, with its more human-like design, is recommended for end-to-end QA, QA of RT accessories, the assessing connectivity and data transfer, artefact evaluation, and QA for MRI-CT registration. The anthropomorphic phantom matches other phantoms in magnetic field drift test and radiofrequency coil evaluation. However, for transmitter and gain calibration, a homogeneous phantom is recommended over the

anthropomorphic and ACR phantoms. However, a phantom with appropriate features such as ACR phantom is essential for certain QA tests unachievable by the anthropomorphic phantom, particularly in areas like high-contrast spatial resolution and low-contrast detectability. Meanwhile, the anthropomorphic phantom plays a significant role in various MRI-related QA procedures for RT and serves as a valuable complement to the ACR phantom. For thorough QA in MRI for RT, it is essential to use homogeneous, geometric, and anthropomorphic phantoms.

Chapter 6 Optimisation of cone beam CT radiotherapy imaging protocols using a 3D printed head and neck anthropomorphic phantom

6.1 Introduction

Currently, most linear accelerators used for RT are equipped with kV CBCT imaging systems. CBCT represents a modality for acquiring three-dimensional (3D) representations of patient anatomies, commonly employed for precise patient alignment during RT interventions (224, 225). This is particularly important in the context of H&N cancers due to the proximity of the treatment volume to critical organ at risk (OAR) such as the salivary glands, spinal cord, brainstem, eyes and optical nerves. This proximity can lead to challenges in producing a radiotherapy treatment plan that sufficiently treats the target, whilst minimizing dose to healthy OARs. Although CBCT allows an accurate way of ensuring the planned radiotherapy matches the treatment, the utilization of CBCT results in additional ionizing radiation dose, which increases the risk of developing secondary cancers (226, 227). The cumulative radiation exposure associated with high-dose CBCT protocols over the course of a H&N radiotherapy treatment lasting several weeks can be equivalent to the radiation delivered during a single therapeutic radiotherapy dose (228-230).

Linear accelerator-based CBCT devices are equipped with pre-set scanning parameters which include kV of the X-ray energy and milliampere-seconds (mAs) for photon output and radiation dose, as well as gantry speed for controlling the number of acquisitions used to generate images. However, these pre-sets may not always be optimised for the best image quality or to minimise radiation exposure (230).

A recent international survey found that the majority of centres use vendor-supplied CBCT pre-set protocols and that fewer than half adapt these protocols for individual patients (231). It is hypothesized that this may be due to limitations in resources, such as a lack of an appropriate phantom, which is essential for optimising CBCT protocols. CBCT systems do not typically incorporate automatic exposure control (AEC) adjustment like diagnostic imaging scanners do (232). Consequently, it is important to adjust CBCT protocols to ensure that radiation exposure is minimized while still producing sufficient image quality for their intended purpose (233). For conventional RT, CBCT image quality is defined as sufficient if the registration between CBCT-computed tomography (CT) is accurate enough to setup the patient reproducibility for each image acquisition. However, the required image quality can vary depending on the intended purpose: lower image quality may suffice for boney registration, while higher image quality is necessary for soft tissue registration, which demands clearer differentiation between different soft tissues.

ART involves the modification of RT plans to accommodate variations in patient anatomy throughout the treatment course (234-236). However, a primary limitation preventing CBCTs direct use for dose calculations in ART arises from the inherent inaccuracies and artifacts present in CBCT images, notably in terms of HU representation (237, 238). Consequently, two principal approaches are commonly employed to surmount this challenge: deformable registration of the initial planning CT scan onto CBCT images, or generation of synthetic CT images from CBCT data. Therefore, for ART CBCT image quality must be higher than for conventional radiotherapy, and it is preferable for HU values assessed on CBCT to match CT, in order to allow accurate deformable registration or synthetic CT generation (239, 240).

Scatter correction algorithms play a crucial role in enhancing the quality of CBCT images by addressing the detrimental effects of scattered radiation. The Uniform Scatter Correction method, a proprietary technique developed by Elekta (241), applies a uniform correction factor throughout the image. The scatter correction parameter value representing the ratio of scattered radiation to primary radiation per pixel. Its value can range from 0-1 with a value of 1 representing 100% scattered radiation. The optimisation of this parameter holds promise for enhancing the image quality of CBCT imaging.

Quantitative evaluation of CBCT image quality often involves the assessment of noise levels and contrast-to-noise ratios (CNR), typically conducted using either phantom studies or analysis of patient images. While numerous investigations have reported CBCT image quality based on phantom measurements, a notable gap persists regarding the impact of optimised images on the capability of therapeutic radiographers to perform online image registration during treatment (230, 242). Additionally, the minimum acceptable imaging dose level in a clinical setting can vary depending on the specific task or imaging needs (243). As such, evaluation of image quality alone may not be sufficient, and user experience for the specific task must also be considered.

It would not be ethical to expose patients to more ionizing radiation than necessary, therefore optimisation of CBCT is challenging in vivo. One solution to this is using anthropomorphic phantoms. In studies employing anthropomorphic phantoms, the Alderson Rando phantoms have conventionally served as the preferred choice (244-248). However, these phantoms, comprised of multiple slices of tissue-equivalent materials with deliberately incorporated holes for dosimeters and inter-slice spaces, introduce variations that compromise their capacity to replicate human anatomy. Additionally, discrepancies in tissue

equivalence between the Alderson phantom and actual human tissue in CBCT applications have been reported, Specifically, the phantom's material under-attenuates X-rays at lower energies typical of diagnostic procedures, reducing the accuracy in simulating human tissue (18). Recent advancements in 3D printing technology have facilitated the development of phantoms that more accurately mimic human anatomy (122).

The primary aim of this work was to optimise CBCT acquisition protocols for H&N patients, with a particular emphasis on facilitating precise patient positioning in conventional radiotherapy and ART. This was achieved through systematic adjustments of scan acquisition and scatter correction parameters to create a variety of imaging protocols. These imaging protocols were assessed on a 3D-printed H&N anthropomorphic phantom allowing assessment of all protocols in order to provide recommendations for clinical practice. Furthermore, the dose delivered from each imaging protocol was measured and taken into account in these recommendations.

6.2 Methods

6.2.1 Phantom

This work utilized a 3D-printed H&N anthropomorphic phantom developed in Leeds (13).

6.2.2 CT scan acquisition

A CT scan of the anthropomorphic phantom was acquired as a reference image for registration purposes and to serve as the benchmark for CT number comparison with CBCT. The CT scan was acquired using a Philips Brilliance Big Bore CT scanner (Philips Medical Systems, The Netherlands) with 120 kV, 104

mAs, and spatial resolution of 1.17 × 1.17 × 2 mm. The phantom was immobilized in a 5-point head-neck mask in the head-first supine orientation on the CT couch. The phantom was setup using an external lasers (LAP, Lüneburg, Germany) utilizing reference marks on the mask that mimic our local clinical protocol for H&N patients. In all CT images presented in this paper, the window level (WL) was set to 60 and the window width (WW) to 400.

6.2.3 CBCT Image protocol optimisation

The current CBCT scanning parameters employed for H&N patients at LCC was defined as the baseline imaging protocol. This baseline protocol uses a tube voltage of 120 kV with the S20 collimator, the F1 filter, and a gantry speed of 180 degrees/minute. In addition to the baseline protocol, nine additional protocols were devised by adjusting the nominal milliamperage (mA) per frame, nominal milliseconds (ms) per frame, in accordance with Elekta's permissible values.

The additional protocols were categorized into two exposure groups: the lower exposure group and the higher exposure group, as detailed in Table 6-1. To ensure comprehensive exploration of the parameter space while avoiding redundancy, unique ms and mA per frame pairings were employed to generate distinct protocols. The mAs per frame, a product of mA and ms per frame, directly influences the radiation dose and image quality. Higher mAs per frame typically results in a higher radiation dose, which can enhance image quality by reducing noise.

Protocols with mAs per frame exceeding 0.8 were excluded from consideration, as 0.8 mAs per frame was set as the upper limit, representing twice the value used in the current protocol (Protocol 7), which utilizes 0.4 mAs per frame. Protocols 1-6, designated as the lower exposure group, were deliberately formulated to minimize radiation exposure with the aim of assessing the

degradation of image quality. Conversely, protocols 8-10, classified as the higher exposure group, were specifically designed to increase dose allowing the assessment of the expected enhancement of image quality. These protocols encompassed the upper limits of the permissible values, within the 0.8 mAs per frame limit.

Table 6-1 Protocols for CBCT optimisation. Details of the baseline protocol and the 9 adjusted protocols divided into lower and higher exposure groups

Protocol		mA/frame	ms/frame	mAs/frame
The lower exposure protocols	1	10	10	0.10
	2	12	10	0.12
	3	16	10	0.16
	4	10	20	0.20
	5	12	20	0.24
	6	16	20	0.32
Standard	7	20	20	0.40
The higher exposure protocols	8	25	20	0.50
	9	32	20	0.64
	10	40	20	0.80

6.2.4 CBCT acquisition, dose measurement and reconstruction

The phantom was scanned using each of the 10 imaging protocols discussed in Table 6-1 utilizing an Elekta Versa HD XVI scanner (Elekta, Stockholm, Sweden). The phantom was setup on the linac couch in the same way described for the CT couch in section 6.2.2. To quantify the radiation dose, a TW31010 Semiflex 0.125 cm³ ionization chamber (PTW, Freiburg, Germany) was inserted into the designated dosimeter compartment in the cranium and connected to a UNIDOS electrometer (PTW, Freiburg, Germany). During each imaging protocol

acquisition the resultant charge measured in the semi-flex ionization chamber was measured in picocoulombs (pC) and used as radiation dose assessment, relative to the baseline protocol.

Subsequently, reconstruction of acquired data was performed offline utilizing Elekta XVI release 5.0.4 b44 software. Reconstruction procedures adhered to the clinical protocol employed at LCC, incorporating a scatter correction parameter value set to 0.24 and a spatial resolution of $0.5 \times 0.5 \times 1$ mm. These images are referred to as imaging protocols 1-10 (standard scatter correction).

To assess the influence of varying the scatter correction parameter value on the quality of images, this parameter was systematic varied between 0.04-0.94 in steps of 0.1 to reconstruct images using all 10 image protocols. These images are referred to as imaging protocols 1-10 (varying scatter correction).

6.2.5 Quantitative image assessment

Three distinct regions of interest (ROIs), representative of brain tissue, bone structures, and soft tissue, were manually delineated on CT images using 3D Slicer (version 4.5.0; contributors of 3D Slicer; www.slicer.org). The edges of structures were avoided to mitigating partial volume artifacts, thereby ensuring precise mean CT number and standard deviation measurements, see Figure 6-1. The brain, bone and soft tissue ROIs had a volumes of 58 cm³, 13.2 cm³ and 48.9 cm³ respectively. Subsequently, a manual rigid registration was used to align the CT reference image and each corresponding CBCT reconstruction. The delineated ROIs were transferred from the CT image to each of the varying scatter correction CBCT images using this rigid registration pathway. Within each ROI, on both CT and all CBCT images, mean and standard deviation (SD) values of CT numbers were measured in order to compare each CBCT imaging protocol to the CT benchmark. 2D heat maps were created to visualize the deviations in

CBCT numbers from reference CT numbers across various imaging protocols and scatter correction parameters. These maps help identify optimal settings for brain, bone, and soft tissue. Additionally, the CNR for Brain/Soft tissue, Bone/Soft tissue and Brain/Bone was calculated for protocols 1-10 (standard scatter correction) to further evaluate the imaging quality.
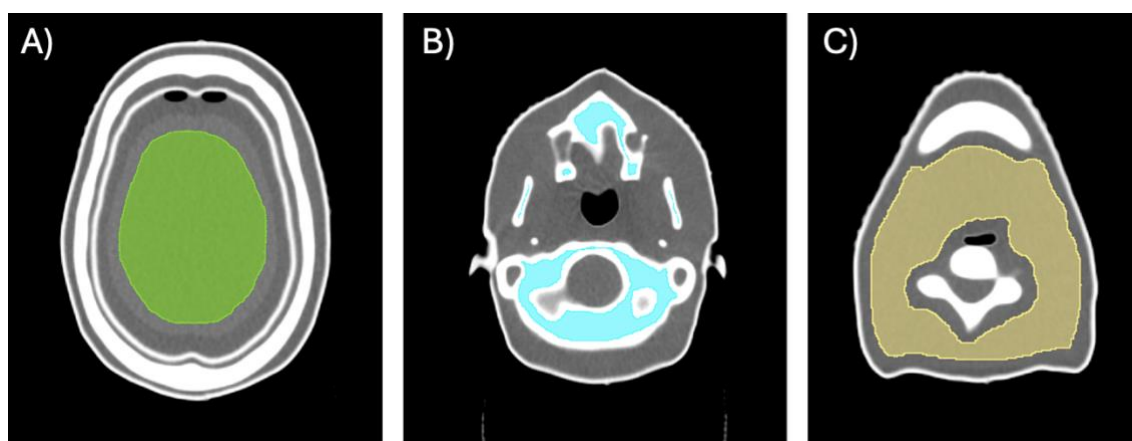
Figure 6-1 Examples of manually drawn regions of interest (ROIs). A) Brain ROI in green. B) Bone ROI in blue. C) Soft tissue ROI in yellow

6.2.6 Qualitative image assessment

In order to assess the CBCT image quality and clinical usability in a patient setup pathway, three Clinical Medical Scientists specializing in radiotherapy imaging conducted independent manual registrations of all of the standard scatter correction CBCT images onto the reference CT scan in Elekta XVI release 5.0.4 b44. They evaluated each registration using a Likert scoring system, a method for subjective assessment that assigns numerical values to qualitative judgments, adapted from the study by Agnew et al. (242) consisting of five points: 5 = Easy to Use; 4 = Okay to Use; 3 = Challenging; 2 = Barely Usable; 1 = Not Usable. To mitigate against potential bias, the Clinical Scientists were blinded to the specific CBCT imaging protocol settings during the evaluation process, and images were

assessed in a random order. This approach ensured an objective assessment of image quality and clinical usability across the diverse range of CBCT protocols.

To assess the feasibility of implementing each of the CBCT imaging protocols in a clinical setting, the Clinical Scientists were timed performing the CBCT registration using the software that would be used clinically. The timing commenced when the image became visible on the software and concluded upon the completion of manual adjustments. This time provided a valuable insight into the practicality and efficiency of each CBCT imaging protocol within a clinical workflow.

The manual registration served as a baseline for each Clinical Scientist to perform a subsequent automated grey value rigid registration, which aligns the images by comparing intensity values (grey levels) between corresponding regions and applying rigid transformations (translation and rotation) (109). After both the manual and automatic rigid registration steps, the table corrections in the lateral, longitudinal and vertical directions reported in the XVI software were recorded.

6.2.7 Qualitative image assessment

To assess the consistency of the qualitative evaluations regarding image quality and clinical usability among the three Clinical Scientists, Gwet's Agreement Coefficient 2 (Gwet's AC2) with its corresponding 95% confidence interval was used (249). Furthermore, to assess the impact of each imaging protocol on the variability of table correction values derived from both manual and automatic rigid registrations, the SD of table movements in three directions (lateral, longitudinal, and vertical) was calculated for each protocol. These calculations were based on

registrations performed by all Clinical Scientists and were performed independently for both manual and automatic registration.

The Shapiro-Wilk test was used to assess the normality of table correction values obtained independently from both manual and automatic rigid registrations for all protocols, as well as to evaluate the normality of registration times for manual registrations conducted by the Clinical Scientists. Given the presence of both normally and non-normally distributed datasets, the Kruskal-Wallis test, a non-parametric statistical method, was used to compare table correction values across different imaging protocols and to analyze registration times across various protocols and among different Clinical Scientists.

6.3 Results

All 10 imaging protocols were acquired on the H&N anthropomorphic phantom and for each the standard scatter correction and varying scatter correction images were reconstructed. Figure 6-2 shows an axial CT image and axial CBCT images from 10 different CBCT protocols at the same level from 10 different protocols (standard scatter correction), numbered 1 to 10, illustrating variations in image quality. Beam hardening artifacts are observed for protocols 9-10.
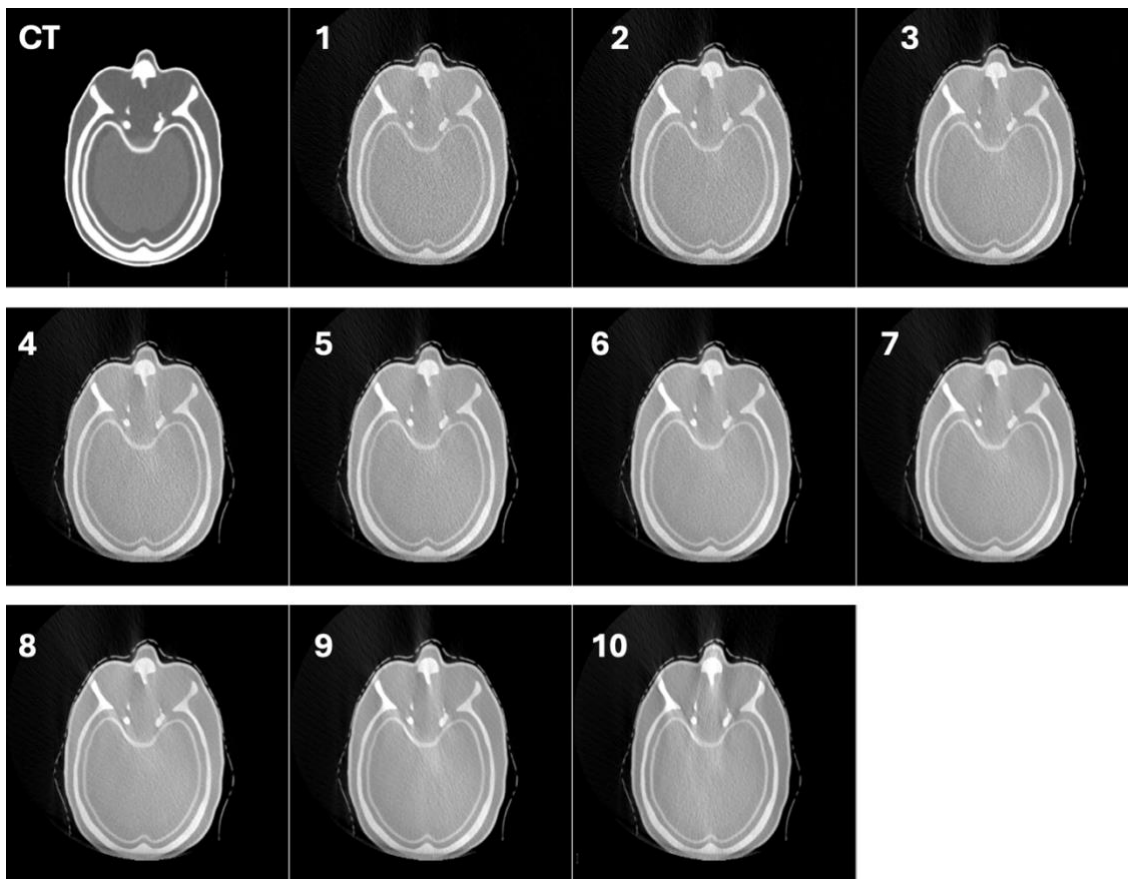
Figure 6-2 Axial CT image and axial CBCT images from 10 different CBCT protocols at the same level. The first image on the top left is a conventional axial CT scan, followed by axial CBCT images labeled 1 to 10, showing variations in image quality.

Figure 6-3 shows the impact of varying scatter correction parameters on axial CT and axial CBCT images for Protocol 7. When the scatter correction parameter is 0, no scatter correction is applied, resulting in images with artifacts. As the scatter correction parameter increases, notable improvements in image quality and artifact reduction can be observed, especially from 0.04 to 0.34. However, from 0.64 to 0.94, there seem to be noticeable artifacts reappearing.
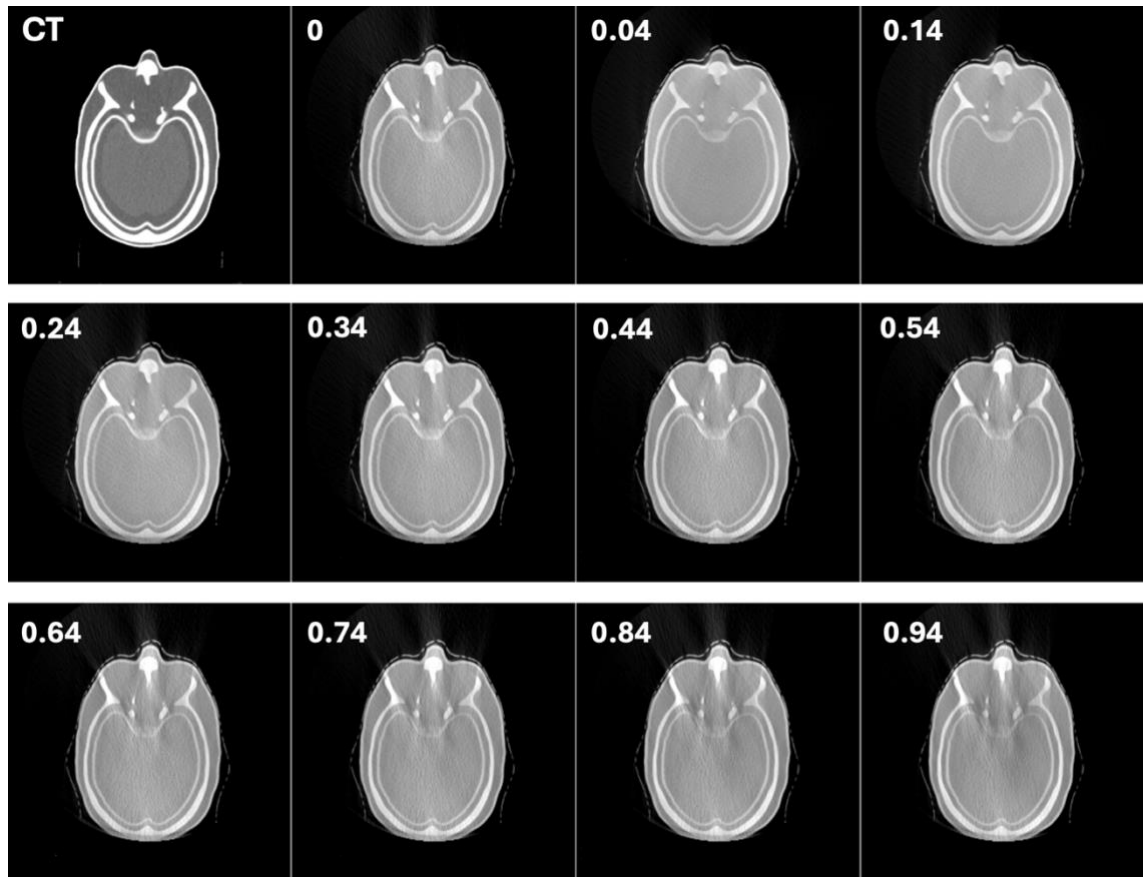
Figure 6-3 Axial CT image and axial CBCT images for Protocol 7 at the same level showing the effect of scatter correction parameters. The first image on the top left is a conventional axial CT scan, followed by CBCT images with scatter correction parameters ranging from 0 to 0.94.

The measured radiation dose from each protocol, relative to the baseline

protocol (protocol 7) is shown in Figure 6-4.
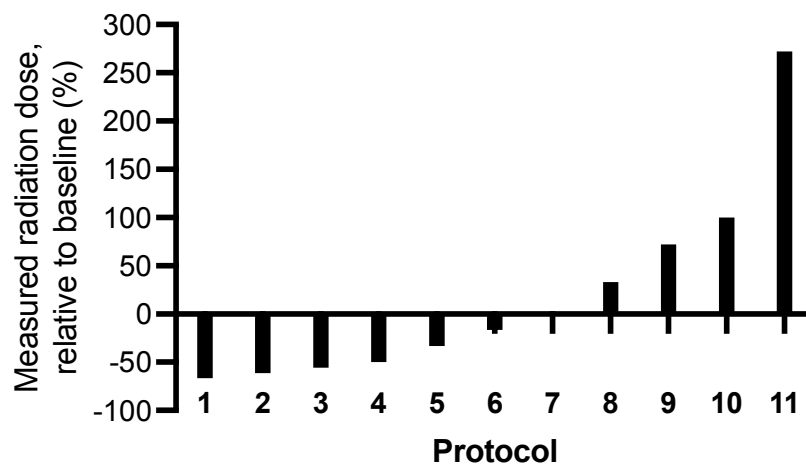
Figure 6-4 The measured radiation dose for each of the 10 CBCT imaging protocols, relative to the baseline protocol (protocol 7).

6.3.1 Quantitative image assessment

The mean and SD of CT numbers within the brain, bone and soft tissue ROIs were measured in the reference CT and the CBCT images reconstructed with varying scatter correction factors across all 10 imaging protocols. The heat maps illustrating the deviations in CBCT numbers from reference CT numbers across various imaging protocols and scatter correction parameters for brain, bone, and soft tissue are presented in (Figure 6-5). The yellow regions in the heat maps indicate minimal deviation from reference CT numbers. Protocols and scatter correction parameters that align closely with yellow regions are preferable for minimizing imaging discrepancies. No single protocol or scatter correction parameter yields the best results for brain, bone, and soft tissue simultaneously. For brain, the protocols that demonstrate the smallest differences are Protocol 3 with a scatter correction parameter of 0 or 0.54. For bone and soft tissue, the optimal protocol and scatter correction parameter combination is Protocol 10 with a scatter correction parameter of 0.24. This necessitates a compromise in the selection process to balance accuracy across different tissues.
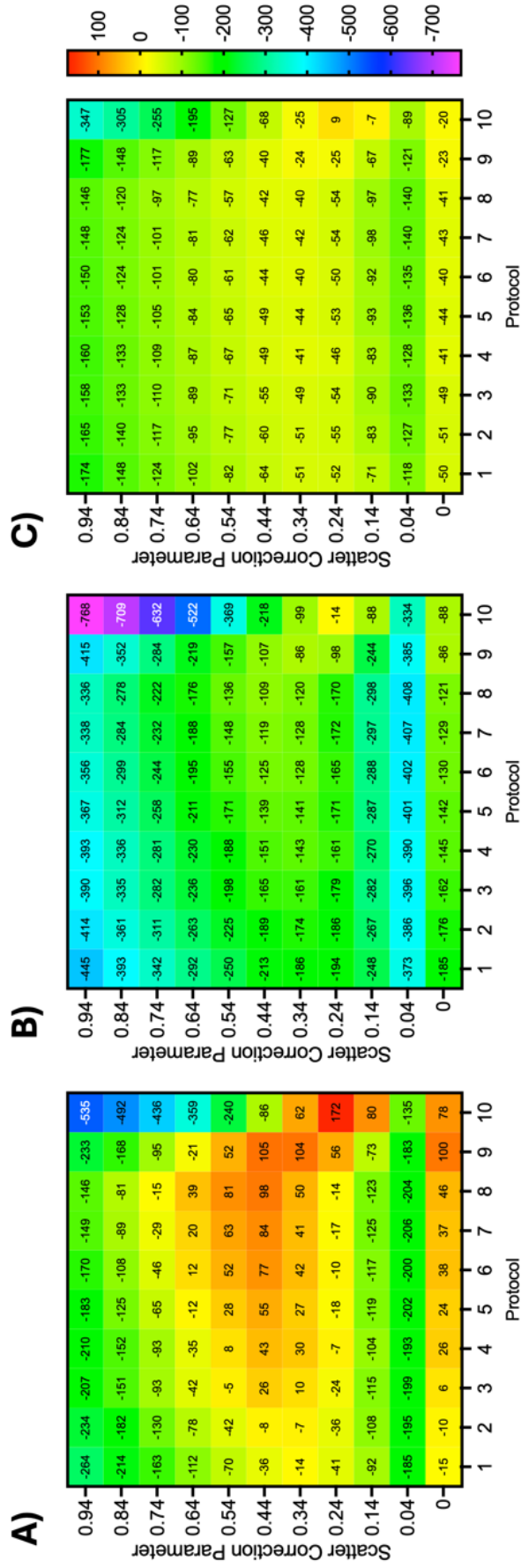
Figure 6-5 Heat maps showing the differences in CBCT numbers compared to reference CT numbers across various imaging protocols and scatter correction. A) Brain, B) Bone, and C) Soft Tissue

Results for all protocols with scatter correction factors of 0.24 (standard scatter correction) are shown in Figure 6-6. Between protocols 1 and 8, minimal variation in mean CT numbers is observed. Specifically, bone exhibits a mean of 333.4 ± 10.4 HU, brain exhibits 5.1 ± 11.2 HU, and soft tissue exhibits -48.8 ± 2.7 HU across these protocols. Regarding SD, it is noted that the SD for soft tissue, brain, and bone decreases, as expected, with an increase in radiation dose. However, at protocols 9 and 10, the SD for bone and brain tissues begins to increase, indicating a departure from this trend.
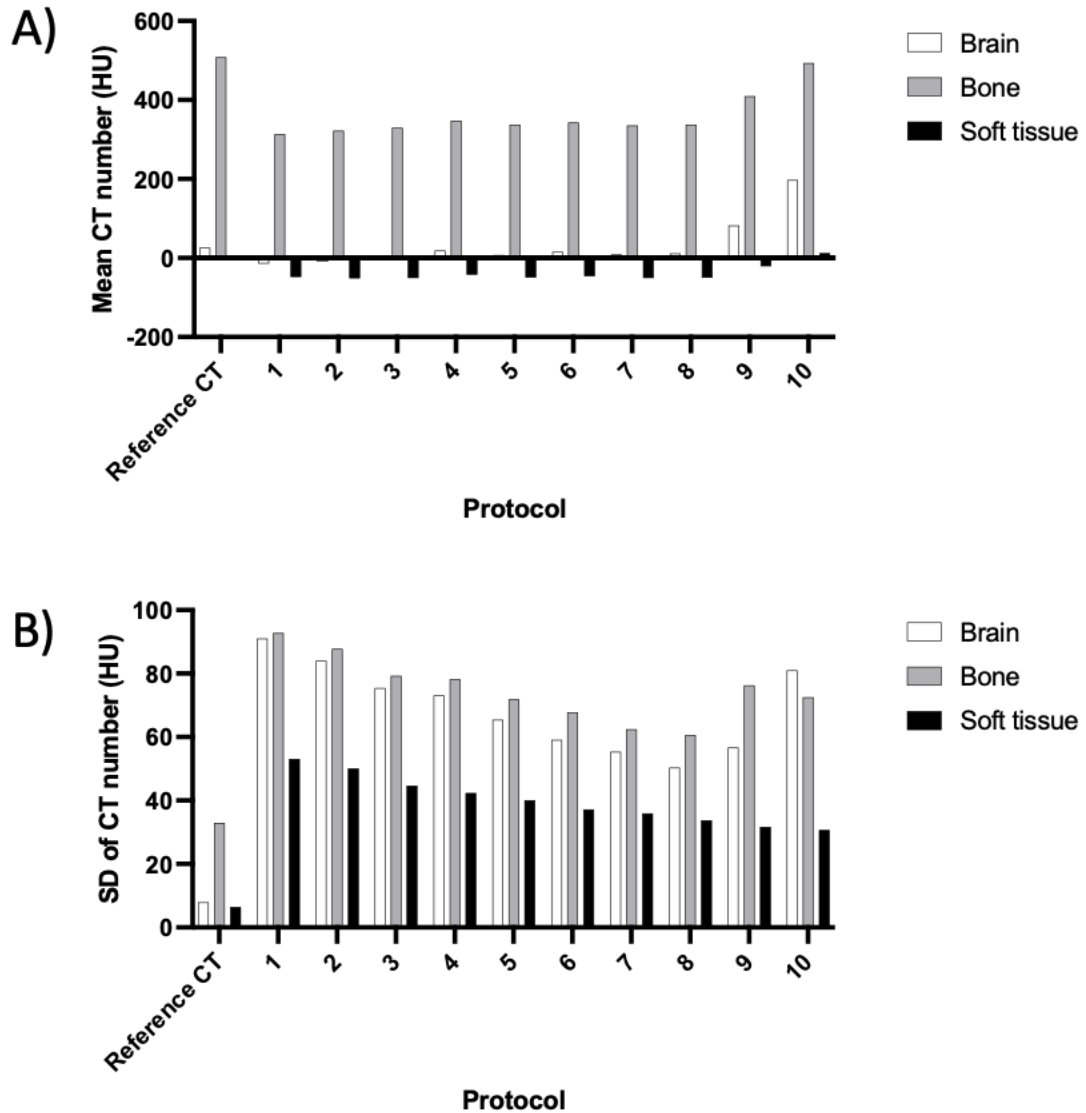
Figure 6-6 The A) Mean and B) Standard Deviation (SD) of CT Numbers for the brain, soft tissue, and bone ROIs for reference CT and all 10 CBCT scan protocols reconstructed with a scatter correction factor = 0.24.

The effect of varying the scatter correction factor for the baseline CBCT protocol (protocol 7) on the mean and SD of CT numbers is shown in Figure 6-7. Detailed results for similar analyses conducted on Protocols 1-6 and 8-10 are provided in appendix 3. As the scatter correction parameter is increased from 0.04 to 0.44, there is a noticeable increase in HU values for all materials within the phantom. This upward trend reaches its peak at a scatter correction parameter of 0.44. However, beyond this point, the HU values begin to decrease.

Regarding the SD of CT numbers, an increase was observed for bone as the scatter correction parameters increased. In the brain, there was an initial increase in the SD of CT numbers with scatter correction parameters rising from 0.04 to 0.54, followed by a subsequent decrease. However, these values did not return to the lower levels observed with the initial scatter correction parameter. For soft tissue, the SD of CT numbers is relatively constant at scatter correction parameters of 0.34 and below, with a modest overall upward trend at scatter correction parameters above this value.
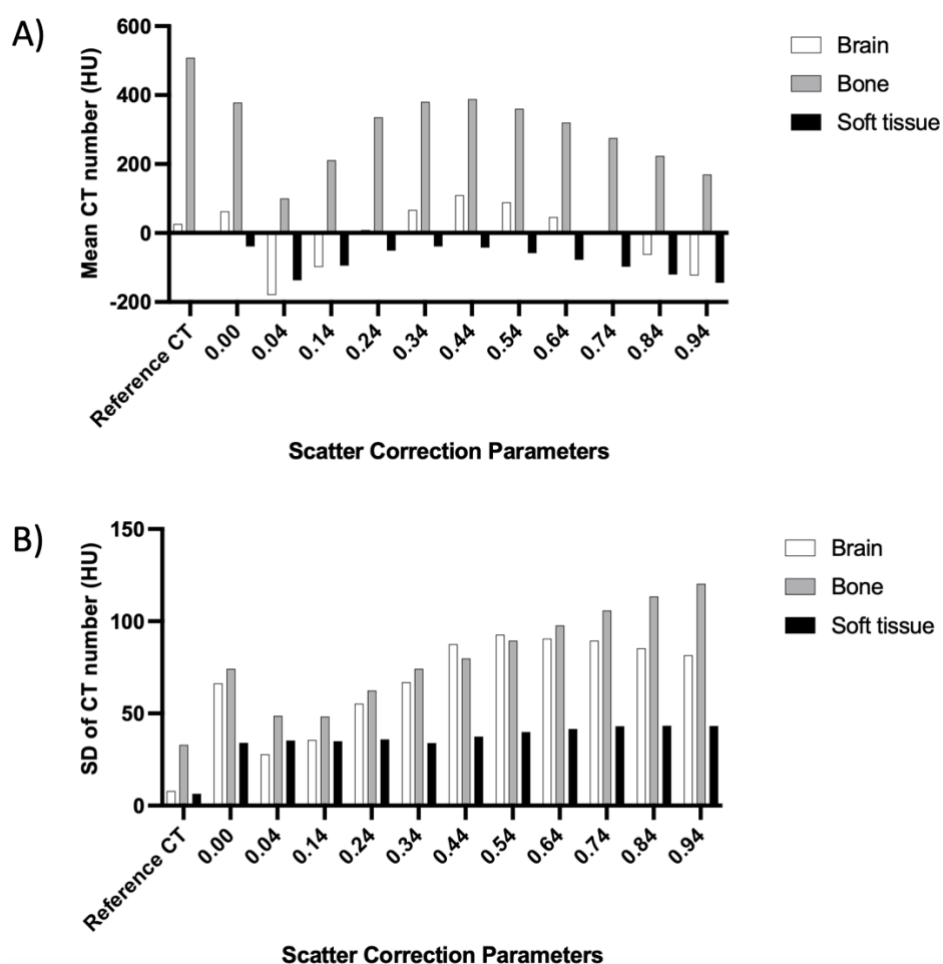
Figure 6-7 The A) Mean and B) Standard Deviation (SD) of CT Numbers within the brain, soft tissue, and bone ROIs for the reference CT the baseline CBCT imaging protocol (protocol 7) reconstructed with different scatter correction parameters.

The CNR for Brain/Soft tissue, Bone/Soft tissue and Brain/Bone for protocols 1-10 (standard scatter correction) are shown in Figure 6-8. There is a general increasing trend in CNR from Protocol 1 to Protocol 9 for all tissue comparisons. The CNR tends to peak around Protocol 9, then declines notably in Protocol 10 for both Bone/Soft tissue and Brain/Bone. For Brain/Soft tissue, the CNR decreases slightly but not sharply.
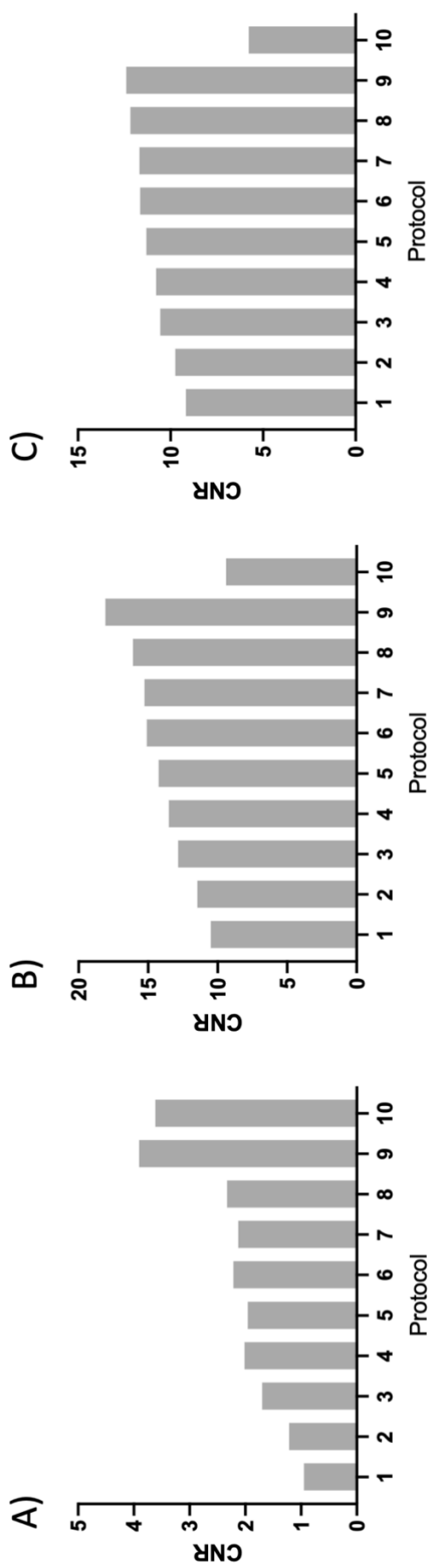
Figure 6-8 CNR for A) Brain/Soft tissue B) Bone/Soft tissue and C) Brain/Bone

6.3.2 Qualitative and quantitative image registration assessment

The Likert scoring given by three Clinical Scientists for all 10 CBCT imaging protocols with the standard scatter correction is shown in Figure 6-9. The Gwet's AC2 for inter-observer agreement was 0.18 demonstrating a slight agreement (250).

Evaluator B consistently assigned lower ratings compared to evaluators A and C, with mean scores of 3.8, 4.8, and 4.6, respectively. For the protocols with lower radiation doses (protocols 1 to 6), none received lower scores than the baseline protocol (protocol 7), except for evaluator A with protocol 4 and evaluator C with protocols 2 and 3 all scoring 4, below the baselines score of 5.
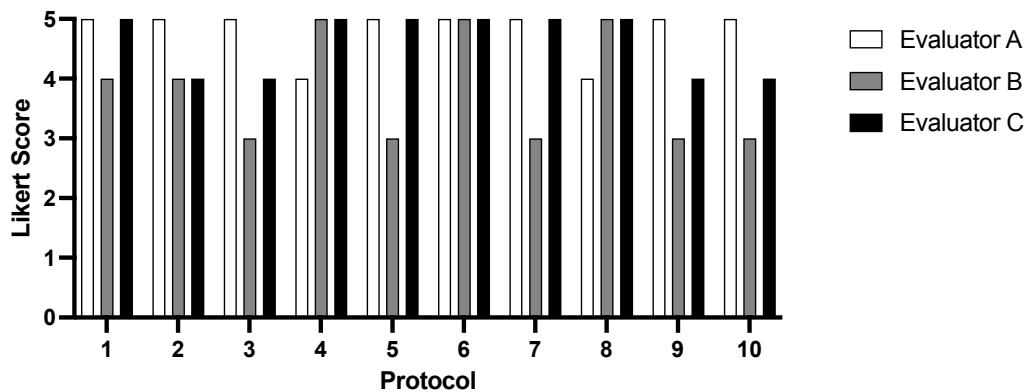
Figure 6-9 Likert scoring given by three Clinical Scientists for all 10 CBCT imaging protocols with the standard scatter correction.

The SDs of table corrections in the lateral, longitudinal, and vertical directions obtained from both manual and automatic registrations by the three Clinical Scientists are shown in Figure 6-10. Overall as expected, manual registration displayed higher standard deviations compared to automatic registration, indicating greater variability in manual adjustments. Specifically, the highest

standard deviation observed in table corrections was 0.08 cm, noted in protocol

7 and 9 using manual registration.
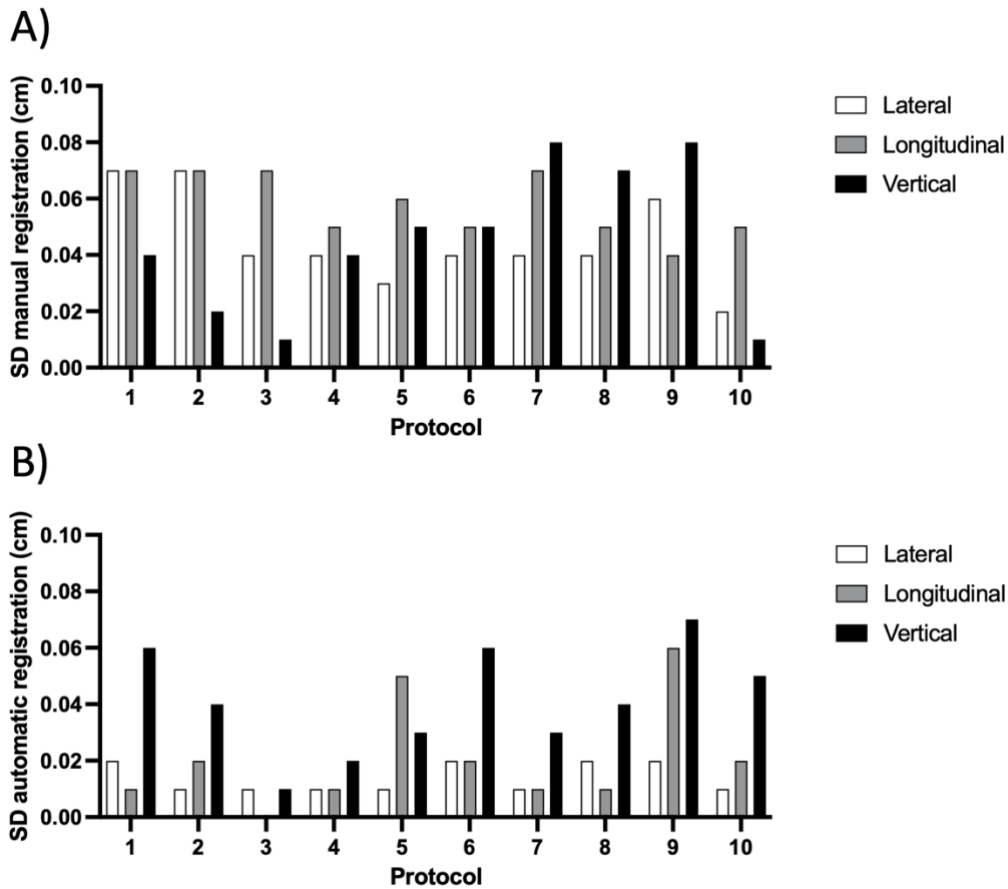
Figure 6-10 Standard Deviation (SD) of table correction measurements based on image registration by the three Clinical Scientists across all 10 protocols using: A) Manual registration and B) Automatic registration.

The Shapiro-Wilk test results for the table correction values demonstrated that

some of these table correction values are not normally distributed, as evidenced

by p-values <0.05. This indicates a significant departure from a normal

distribution in these table correction values, necessitating the use of the Kruskal-

Wallis test for all comparisons. The p-values resulting from the Kruskal-Wallis test

for table correction measurements obtained by three Clinical Scientists across

various protocols are all greater than 0.2 (see Table 6-2). This indicates that there

are no statistically significant differences in the measurements across different

protocols, whether using manual or automatic registrations.

Table 6-2 the P-values for the Kruskal-Wallis test assessing the differences in table correction measurements obtained by three Clinical Scientists across various protocols.

Directions	Manual	Automatic
Lateral	0.23	0.47
Longitudinal	0.24	0.33
Vertical	0.41	0.51

The time taken for manual registration for the 10 CBCT imaging protocols, for all 3 Clinical Scientists are shown in Figure 6-11.
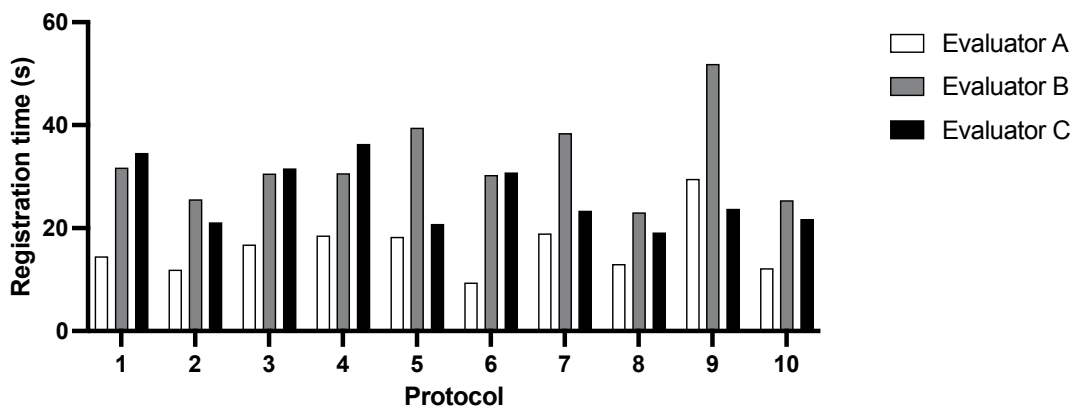
Figure 6-11 Comparison of the time taken for CBCT to planning CT manual rigid registration by Clinical Scientists A, B, and C across 10 different CBCT imaging protocols.

The Shapiro-Wilk test results for the time taken by the Clinical Scientists to perform image registration indicated that the data was not normally distributed for at least one of the protocols, as evidenced by p-values < 0.05. This indicates a significant departure from a normal distribution in these timing results, necessitating the use of the Kruskal-Wallis test for all comparisons. The Kruskal-Wallis test demonstrated a p-value of 0.87, indicating no significant statistical difference in the time taken for registrations performed by the Clinical Scientists across the different CBCT imaging protocols.

6.4 Discussion

To the best of the researcher's knowledge, this study represents the first effort to optimise CBCT protocols using a 3D printed H&N phantom, coupled with an evaluation of these protocols by Clincial Scientists. Moreover, this work used a novel methodology of assessing protocol optimisation using table correction variation measurements.

3D-printed phantoms have proven to be highly effective due to their anatomically accurate designs, which closely mimic various regions of the human body, such as the H&N. These anthropomorphic phantoms allow imaging protocols to be evaluated under realistic clinical conditions, providing a high level of precision in simulating human anatomy. Furthermore, their ability to replicate tissue responses to radiation enables accurate radiation dose measurements, making them valuable tools for optimising imaging techniques, radiotherapy protocols, and dosimetry practices (251, 252).

For ART, there is no single protocol optimal for all tissues. For brain, Protocol 3 with scatter corrections of 0 or 0.54 showed the smallest differences from the reference CT. For bone and soft tissue, Protocol 10 with a scatter correction of 0.24 was optimal. These findings highlight the necessity of tailoring scatter correction parameters to the specific requirements of different tissues. To determine if these protocols are suitable for ART, further studies including dose measurements using CBCT and comparisons with reference CT are required. This will help establish the optimal protocols for clinical use.

Quantitative analysis of CT numbers of different regions of the phantom demonstrated protocols 9-10 exhibited higher mean CT numbers for brain, bone,

and soft tissue compared to other protocols. Contrary to expectation, despite the utilization of higher radiation doses used in protocols 9-10, the SD for brain and bone measurements also increased. This unexpected outcome is hypothesized to be due to the influence of beam hardening effects, wherein an increase in photon count, while maintaining the same energy level, may lead to heightened noise and variations in CT numbers across protocols (253-255).

Exploring different scatter correction parameters revealed a trend wherein mean CT number values increased with scatter correction parameters ranging from 0.04 to 0.44 before beginning to decrease. It is hypothesized that at low scatter correction parameters (0.04 to 0.44), the algorithm may not be sufficiently correcting for scatter, gradually improving until 0.44, where it reaches optimal correction. Above this scatter correction value the algorithm may overestimate scatter, which could lead to an unnecessary reduction in HU values. This trend underscores the importance of selecting an appropriate scatter correction parameter to optimise CT number accuracy. Additionally, SD was observed to increase as scatter correction parameters rose for brain (up to a scatter correction factor of 0.54) and bone, but remained approximately constant for soft tissue, indicating a tissue-dependent relationship between scatter correction and CT number. This variation is likely due to differences in radiodensity, higher-density tissues like bone scatter more, increasing noise when corrected. Noise is expected to increase with the scatter correction parameter due to subtracting a denoised, low-frequency scatter signal from the original data, leaving high-frequency noise unaddressed in the corrected data (256).

The measurement results of the CNR indicate that this ratio decreases as the radiation dose decreases for both bone/soft tissue and brain/soft tissue. However, qualitative and quantitative assessments of image registration showed

that this decrease does not significantly affect bony registration. Therefore, lower-dose protocols can be selected for bony registration while still maintaining adequate SNR. In terms of soft-tissue registration, a phantom with more detailed soft tissue structures is needed to better evaluate the impact of radiation dose. However, the data shows that Protocol 9 has the highest CNR across assessments, making it a promising candidate for further investigation to enhance soft-tissue contrast and image quality.

Inter-observer agreement among Clinical Scientists was slight, as evidenced by a Gwet's AC2 value of 0.18 (250). This agreement may have been influenced by the limited number of evaluators and potential disparities in training or experience levels among them, or ambiguities in the Likert scoring system.

Regarding image registration, manual registration exhibited greater variability compared to automatic registration, highlighting the non-negligible contribution of human factors to registration inconsistency. Protocol 4 demonstrated improved consistency in both registration methods, emphasizing its potential suitability for clinical application due to reliable image alignment.

This study revealed no significant differences between low-dose protocols and the standard protocol, in terms of table corrections and manual registration times for bony registrations. This suggests that reducing the radiation dose by over 50% compared to the baseline protocol is feasible for patient positioning without compromising scan usability or efficiency. These findings align with existing literature, particularly with the study conducted by Agnew et al. (242), which evaluated the optimisation of Varian TrueBeam CBCT imaging protocols. Agnew et al. (242) evaluated the protocol optimisation of Varian TrueBeam CBCT patient images utilising qualitative scoring systems by therapeutic radiographers and

physicists. It was reported that adjusting protocol settings from the default parameters of 100 kV and 150 mAs to 125, 100, and 75 mAs did not significantly affect overall image quality. However, a discernible decrease in image quality was observed specifically in the shoulder region when utilizing the 75 mAs protocol.

Considering patient size in CBCT scan protocol optimisation is crucial, although for the H&N region, a single protocol for adults may suffice due to minimal variation in patient size (242). However, further optimisation of pediatric CBCT protocols would necessitate a phantom representing small patients.

Limitations of this study include its reliance on the perspectives of only three Clinical Scientists, potentially limiting the breadth of insights gained as therapeutic radiographers where not utilized. While Clincial Scientists are often involved in CBCT pathways, therapeutic radiographers are typically responsible for acquiring CBCT images and aligning them with reference CT scans. Additionally, the study's reliance on phantom experiments may not fully capture the complexities and variations present in real patient scenarios such as variability in tissue composition, blood flow, or patient movement during imaging. These factors could complicate image acquisition and interpretation, introducing variability that affects the generalisability of the results. Future research should aim to address these limitations by engaging therapeutic radiographers and extending findings to patient CBCT cases, thereby enhancing the applicability and validity of the study's conclusions. To implement the optimised CBCT protocols in clinical practice, a gradual approach is recommended. Trials should begin with protocols involving minimal dose reductions to assess their feasibility and image quality. Once validated, protocols with progressively greater dose reductions can be tested to determine the lowest dose that still provides adequate

clinical utility. This stepwise strategy ensures patient safety while optimising radiation exposure.

6.5 Conclusion

In conclusion, the optimisation of CBCT scan protocols for adult H&N patients was successfully achieved utilizing a 3D-printed H&N anthropomorphic phantom. This innovative 3D printed approach proved useful in overcoming the limitations associated with current commercial anthropomorphic phantoms and has been demonstrated to allow an assessment of CBCT imaging protocols.

The findings of this study demonstrated that a reduction in radiation dose by over 50%, compared to the current clinical baseline protocol used in LCC for bony registration, was achievable without compromising the efficacy of patient alignment. This substantial dose reduction aligns with the As Low As Reasonably Practicable (ALARP) principle and demonstrates the importance of CBCT protocol optimisation. Furthermore, it was also demonstrated that dose could be reduced from the baseline protocol, whilst giving more accurate CT numbers for brain, soft tissue, and bone which may have benefits for ART. Additionally, the improved CNR observed in Protocol 9 suggests significant potential for enhancing soft tissue matching. However, to better evaluate this, a phantom with more detailed soft tissue structures is needed.

Overall, this study highlights the potential of 3D-printed anthropomorphic phantoms as valuable tools in optimising imaging protocols and reducing the dose patients receive due to CBCT during their radiotherapy treatments.

Chapter 7 Discussion, Contributions, and Future Directions

7.1 Discussion

The aim of this PhD project was to evaluate anthropomorphic multimodality phantoms and explore ways to utilise them for RT purposes. The work presented in this project focused on three objectives. The first objective was to identify materials that mimic human tissue and organs in CT and MRI, are stable over time, and remain stable after exposure to radiation. The second objective was to evaluate the benefits of using anthropomorphic multimodal phantoms in QA tests recommended by international organizations for MRI use in RT planning. The third objective was to explore the possibility of using these phantoms to conduct clinical optimisation, such as optimising radiation exposure protocols to benefit patients.

The findings of this project suggest that anthropomorphic multimodal phantoms could play a valuable role in RT practices. This research identified 10% PVA-c as a promising simulant for brain grey matter in CT and MRI, stable over one year and after radiation exposure up to 1000 Gy.

One of the key findings of this project is the demonstration of an anthropomorphic H&N phantom's utility in QA of MRI for RT. The phantom offers several advantages over traditional QA tools, such as the ability to simulate real patient treatment plans and measure the delivered radiation dose. By enabling end-to-end testing that mirrors actual clinical scenarios, the use of anthropomorphic phantoms enhances the precision and reliability of RT planning. This could significantly improve the accuracy of treatments, leading to better patient outcomes.

Additionally, the project demonstrated the feasibility of using anthropomorphic phantoms to optimise CBCT protocols, reducing radiation doses for H&N treatments by over 50% without compromising treatment accuracy. This finding directly addresses concerns about excessive radiation exposure during imaging, aligning with the ALARP principle and contributing to safer patient care.

7.2 Novel Contribution

This research offers several contributions to the fields of RT by addressing gaps in the literature and exploring innovative approaches to support clinical practices. While prior research has identified potential materials for phantoms that mimic the properties of human tissue in MRI, CT, or both (13-15), many of these materials have only been evaluated for a single imaging modality. Furthermore, their long-term stability and performance following radiation exposure remain underexplored. This work addresses these gaps by investigating the multimodal suitability, long-term stability, and post-radiation performance of these materials. The results contribute to a better understanding of material suitability for extended clinical use.

This research is the first to systematically evaluate a multimodality anthropomorphic phantom against commercially available alternatives with the aim of meeting the QA standards outlined in the 2021 guidelines published by the IPEM and AAPM (16, 17). The findings provide actionable insights into the suitability of multimodal phantoms for clinical use in RT, specifically in the context of MRI simulation. By providing practical information to support phantom selection, this work aims to assist RT centres in enhancing compliance with QA protocols.

This research explores the use of a multimodal anthropomorphic phantom to optimise CBCT protocols, focusing on improvements in image quality and reductions in radiation dose. By addressing the limitations of commercial phantoms, this study achieved a measurable reduction in radiation dose compared to the currently used clinical baseline protocol without compromising patient alignment. This study highlights a potential application of phantoms beyond QA for MRI.

7.3 Reflections and lessons learned

If this project were to start anew with the benefit of hindsight, certain approaches might be reconsidered to enhance its outcomes. For example, greater emphasis could be placed on creating a more diverse set of tissue-mimicking materials earlier in the project by modifying the properties of some of the materials included in this study. Achieving this level of material customization would require collaboration with materials scientists from the very beginning of the project. Their expertise in designing and tailoring materials with specific properties could prove invaluable in addressing the challenge of accurately replicating a wider range of human tissues across multiple imaging modalities. Establishing such interdisciplinary partnerships early on might facilitate the integration of more advanced materials into the phantoms, thereby expanding their clinical relevance and applicability.

Equally important would be ensuring the use of robust validation methods to reduce uncertainties in material performance evaluations. For instance, multi-sample testing would be integral to capturing the inherent variability that could arise from differences in material preparation or potential anomalies during testing. Reliance on single-sample evaluations, while practical for initial

assessments, may overlook these variations and lead to overestimation of material performance or the rejection of an otherwise suitable material. Adopting a multi-sample approach would help to enhance the reliability and reproducibility of results, providing a stronger foundation for conclusions and broader generalizability of findings.

7.4 Future works

While this research has made significant strides in the development and evaluation of multimodality anthropomorphic phantoms for RT, certain limitations were identified throughout the study, many of which have been detailed in the preceding chapters. These limitations underscore both the challenges inherent in this field and the opportunities for future improvement.

The widespread adoption of anthropomorphic phantoms could significantly improve RT planning and delivery, making treatments safer and more accurate. The goal of this research is to see multimodality phantoms integrated into clinical practice. To achieve this, multi-institutional studies will be crucial to validate the performance of these phantoms across different clinical environments, ensuring their reliability and broad applicability. Such studies will provide the necessary data to support their wider adoption and standardisation. Once developed into commercial products, these phantoms could standardize QA protocols across radiotherapy centers, minimizing variability in treatment accuracy and patient outcomes. To ensure this, their use must be incorporated into international guidelines and recommendations to ensure consistency and reliability.

There is potential to develop new tissue-mimicking materials that can more accurately replicate human tissues across various imaging modalities like CT and MRI. While the 10% PVA-c identified in this project performs well for simulating

brain grey matter, expanding the range of materials to mimic other tissues and organs is crucial for broader clinical use. This potential lies in the development and application of advanced materials and contrast media that can selectively alter their CT numbers or modify T1 and T2 relaxation times, allowing for more precise simulation of different tissues. Collaboration between experts in medical physics and materials science will be essential to achieve these advancements. Ensuring the long-term stability of these materials, particularly beyond one year, remains a key challenge.

Designing anthropomorphic phantoms with interchangeable internal components could be beneficial. For example, in a H&N phantom, having a replaceable brain would offer numerous advantages. This feature would allow the brain to be replaced if aging or degradation begins to occur after the tested period (one year), potentially affecting its imaging properties. Additionally, it would enable the inclusion of various inserts for multiple purposes: measuring geometric distortion, measuring image quality, evaluating ART with inserts representing different tumour sizes, and enhancing dosimetry measurements through the use of various types of inserts designed for different dosimetry techniques.

It is recommended to provide the capability to measure radiation doses utilising a variety of techniques, such as film, thermoluminescent dosimeters (TLD), and 3D gels to enhance reliability and take advantage of each method's strengths. This flexibility allows for cross-verification of results and enables QA to be tailored to user preferences, whether they prefer the precision of TLDs, the detailed 3D mapping of gels, or the real-time feedback from ion chambers. In addition, there should be more than one place to measure the radiation dose using ionization chambers ensuring comprehensive evaluation of dose distribution across critical areas such as the neck.

The benefits of multimodal anthropomorphic phantoms can be enhanced by increasing their compatibility with more than two imaging modalities. For example, the current anthropomorphic H&N phantom could be made compatible with PET, in addition to CT and MRI.

With the advent of the magnetic resonance linear accelerator (MR-Linac), the demand for multimodality motion phantoms for RT purposes has increased. These phantoms hold potential for various applications, including QA, and research and development. Future efforts should concentrate on advancing and employing these phantoms to address the growing requirements of RT.

Future work could expand the development of anthropomorphic phantoms to other important anatomical sites beyond the H&N. Regions such as the thorax, abdomen, and pelvis present unique challenges in RT planning and QA, requiring tailored designs to accurately simulate their anatomical and tissue complexities. Developing phantoms for these areas would enhance their clinical utility and support broader standardization of QA protocols, ultimately improving treatment precision across a wider range of applications.

This project has demonstrated the opportunities available to exploit the potential of anthropomorphic phantoms in QA, clinical optimisation, and development. Beyond RT, these phantoms have promising applications across various areas of medicine, including diagnostic imaging, surgical planning, and medical device testing. It is recommended that future studies explore the application of these phantoms in education and training, where their potential remains largely untapped.

7.5 Conclusion

The work described in this PhD thesis contributes to the development and evaluation of multimodality anthropomorphic phantoms for H&N radiotherapy, focusing on material suitability and clinical application. It identified 10% PVA-c as a stable substitute for brain grey matter in MRI and CT, but also emphasized the need for further research to find materials that can accurately replicate a wider range of human tissues.

This thesis demonstrated the effectiveness of the anthropomorphic phantom in MRI-based QA for radiotherapy while highlighting the complementary role of homogeneous phantoms for specific tasks. In addition, the use of a 3D-printed phantom for optimising CBCT protocols successfully reduced radiation dose by over 50%, without compromising alignment accuracy, adhering to safety standards like the As Low As Reasonably Practicable (ALARP) principle.

Overall, this research highlights the potential of anthropomorphic phantoms to increase confidence in the use of MRI for radiotherapy, enhancing patient safety, and supporting more precise treatment planning. However, further development is needed to expand their capabilities and clinical relevance.

List of References

1. Kron, T., Fox, C., Ebert, M.A. and Thwaites, D. Quality management in radiotherapy treatment delivery. *Journal of Medical Imaging and Radiation Oncology.* 2022, **66**(2), pp.279-290.

2. Ferioli, M., Medici, F., Galietta, E., Forlani, L., Tagliaferri, L., Cilla, S., Cammelli, S., Morganti, A.G. and Buwenge, M. The role of training simulators in interventional radiation therapy (brachytherapy) training: A narrative review. *Journal of Contemporary Brachytherapy.* 2023, **15**(4), pp.290-295.

3. Tajik, M., Akhlaqi, M.M. and Gholami, S. Advances in anthropomorphic thorax phantoms for radiotherapy: a review. *Biomedical Physics & Engineering Express.* 2022, **8**(5), p.052001.

4. Nascimento, M.L.F. Brief history of X-ray tube patents. *World Patent Information.* 2014, **37**, pp.48-53.

5. Ashenafi, M., Jeong, S., Wancura, J.N., Gou, L., Webster, M.J. and Zheng, D. A quick guide on implementing and quality assuring 3D printing in radiation oncology. *Journal of Applied Clinical Medical Physics.* 2023, **24**(11), p.e14102.

6. Chandarana, H., Wang, H., Tijssen, R. and Das, I.J. Emerging role of MRI in radiation therapy. *Journal of Magnetic Resonance Imaging.* 2018, **48**(6), pp.1468-1478.

7. Palmér, E., Nordström, F., Karlsson, A., Petruson, K., Ljungberg, M. and Sohlin, M. Head and neck cancer patient positioning using synthetic CT data in MRI-only radiation therapy. *Journal of Applied Clinical Medical Physics.* 2022, **23**(4), p.e13525.

8. Den, R.B., Doemer, A., Kubicek, G., Bednarz, G., Galvin, J.M., Keane, W.M., Xiao, Y. and Machtay, M. Daily image guidance with cone-beam computed tomography for head-and-neck cancer intensity-modulated radiotherapy: a prospective study. *International Journal of Radiation Oncology* Biology* Physics.* 2010, **76**(5), pp.1353-1359.

9. Joint Head and Neck MRI-Radiotherapy Development Cooperative, Neck, M., Kiser, K., Meheissen, M.A., Mohamed, A.S., Kamal, M., Ng, S.P., Elhalawani, H., Jethanandani, A. and He, R. Prospective quantitative quality assurance and deformation estimation of MRI-CT image registration in simulation of head and neck radiotherapy patients. *Clinical and Translational Radiation Oncology.* 2019, **18**, pp.120-127.

10. Le Cornu, E., Murray, S., Brown, E., Bernard, A., Shih, F.J., Ferrari-Anderson, J. and Jenkins, M. Impact of technological and departmental changes on incident rates in radiation oncology over a seventeen-year period. *Journal of Medical Radiation Sciences.* 2021, **68**(4), pp.356-363.

11. Margalit, D.N., Chen, Y.-H., Catalano, P.J., Heckman, K., Vivenzio, T., Nissen, K., Wolfsberger, L.D., Cormack, R.A., Mauch, P. and Ng, A.K. Technological advancements and error rates in radiation therapy delivery. *International Journal of Radiation Oncology* Biology* Physics.* 2011, **81**(4), pp.e673-e679.

12. Goodman, K.A. *Quality assurance for radiotherapy: a priority for clinical trials.* Oxford University Press US. 2013, 105, pp.376-377.

13. Johnstone, E.R. *Automated MRI-based radiotherapy planning for brain tumours.* thesis, University of Leeds, 2019.

14. Hellerbach, A., Schuster, V., Jansen, A. and Sommer, J. MRI phantoms– are there alternatives to agar? *PloS one.* 2013, **8**(8), p.e70343.

15. Steinmann, A., Stafford, R.J., Sawakuchi, G., Wen, Z., Court, L., Fuller, C.D. and Followill, D. Developing and characterizing MR/CT-visible materials used in QA phantoms for MR g RT systems. *Medical Physics.* 2018, **45**(2), pp.773-782.

16. Speight, R., Dubec, M., Eccles, C.L., George, B., Henry, A., Herbert, T., Johnstone, R.I., Liney, G.P., McCallum, H. and Schmidt, M.A. IPEM topical report: guidance on the use of MRI for external beam radiotherapy treatment planning. *Physics in Medicine & Biology.* 2021, **66**(5), p.055025.

17. Glide-Hurst, C.K., Paulson, E.S., McGee, K., Tyagi, N., Hu, Y., Balter, J. and Bayouth, J. Task group 284 report: magnetic resonance imaging simulation in radiotherapy: considerations for clinical implementation, optimization, and quality assurance. *Medical Physics.* 2021, **48**(7), pp.e636-e670.

18. Shrimpton, P., Wall, B. and Fisher, E. The tissue-equivalence of the Alderson Rando anthropomorphic phantom for x-rays of diagnostic qualities. *Physics in Medicine & Biology.* 1981, **26**(1), p.133.

19. Sung, H., Ferlay, J., Siegel, R.L., Laversanne, M., Soerjomataram, I., Jemal, A. and Bray, F. Global cancer statistics 2020: GLOBOCAN estimates of incidence and mortality worldwide for 36 cancers in 185 countries. *CA: a cancer journal for clinicians.* 2021, **71**(3), pp.209-249.

20. Lee, N., Puri, D.R., Blanco, A.I. and Chao, K.C. Intensity-modulated radiation therapy in head and neck cancers: an update. *Head & Neck: Journal for the Sciences and Specialties of the Head and Neck.* 2007, **29**(4), pp.387-400.

21. Blanchard, P., Gunn, G.B., Lin, A., Foote, R.L., Lee, N.Y. and Frank, S.J. Proton therapy for head and neck cancers. In: *Seminars in radiation oncology*: Elsevier, 2018, pp.53-63.

22. Sroussi, H.Y., Epstein, J.B., Bensadoun, R.J., Saunders, D.P., Lalla, R.V., Migliorati, C.A., Heaivilin, N. and Zumsteg, Z.S. Common oral complications of head and neck cancer radiation therapy: mucositis, infections, saliva change, fibrosis, sensory dysfunctions, dental caries, periodontal disease, and osteoradionecrosis. *Cancer medicine.* 2017, **6**(12), pp.2918-2931.

23. Hutcheson, K.A., Lewin, J.S., Barringer, D.A., Lisec, A., Gunn, G.B., Moore, M.W. and Holsinger, F.C. Late dysphagia after radiotherapy-based treatment of head and neck cancer. *Cancer.* 2012, **118**(23), pp.5793-5799.

24. Newhauser, W.D., De Gonzalez, A.B., Schulte, R. and Lee, C. A review of radiotherapy-induced late effects research after advanced technology treatments. *Frontiers in oncology.* 2016, **6**, p.13.

25. Bratlund, C.V. and Nobriga, C.V. Movement trajectories during percutaneous stimulation at rest of the hyolaryngeal muscles in head and neck cancer patients treated with radiation therapy. *Dysphagia.* 2010, **25**.

26. Lo, A.C., Howard, A.F., Nichol, A., Sidhu, K., Abdulsatar, F., Hasan, H. and Goddard, K. Long-term outcomes and complications in patients with craniopharyngioma: the British Columbia Cancer Agency experience. *International Journal of Radiation Oncology* Biology* Physics.* 2014, **88**(5), pp.1011-1018.

27. Marur, S. and Forastiere, A.A. Head and neck cancer: changing epidemiology, diagnosis, and treatment. In: *Mayo Clinic Proceedings*: Elsevier, 2008, pp.489-501.

28. McDonald, B.A., Dal Bello, R., Fuller, C.D. and Balermpas, P. The use of MR-guided radiation therapy for head and neck cancer and recommended reporting guidance. In: *Seminars in radiation oncology*: Elsevier, 2024, pp.69-83.

29. Bhide, S.A., Davies, M., Burke, K., McNair, H.A., Hansen, V., Barbachano, Y., El-Hariry, I., Newbold, K., Harrington, K.J. and Nutting, C.M. Weekly volume and dosimetric changes during chemoradiotherapy with intensity-modulated radiation therapy for head and neck cancer: a prospective observational study. *International Journal of Radiation Oncology* Biology* Physics.* 2010, **76**(5), pp.1360-1368.

30. Nishi, T., Nishimura, Y., Shibata, T., Tamura, M., Nishigaito, N. and Okumura, M. Volume and dosimetric changes and initial clinical experience of a two-step adaptive intensity modulated radiation therapy (IMRT) scheme for head and neck cancer. *Radiotherapy and Oncology.* 2013, **106**(1), pp.85-89.

31. Duma, M., Kampfer, S., Schuster, T., Winkler, C. and Geinitz, H. Adaptive radiotherapy for soft tissue changes during helical tomotherapy for head and neck cancer. *Strahlentherapie und Onkologie.* 2012, **188**(3), p.243.

32. Noble, D.J., Yeap, P.-L., Seah, S.Y., Harrison, K., Shelley, L.E., Romanchikova, M., Bates, A.M., Zheng, Y., Barnett, G.C. and Benson, R.J. Anatomical change during radiotherapy for head and neck cancer, and its effect on delivered dose to the spinal cord. *Radiotherapy and Oncology.* 2019, **130**, pp.32-38.

33. Avkshtol, V., Meng, B., Shen, C., Choi, B.S., Okoroafor, C., Moon, D., Sher, D. and Lin, M.-H. Early Experience of Online Adaptive Radiation Therapy for Definitive Radiation of Patients With Head and Neck Cancer. *Advances in Radiation Oncology.* 2023, **8**(5), p.101256.

34. Moteabbed, M., Sharp, G., Wang, Y., Trofimov, A., Efstathiou, J.A. and Lu, H.M. Validation of a deformable image registration technique for cone beam CT-based dose verification. *Medical Physics.* 2015, **42**(1), pp.196-205.

35. Landry, G., Nijhuis, R., Dedes, G., Handrack, J., Thieke, C., Janssens, G., Orban de Xivry, J., Reiner, M., Kamp, F. and Wilkens, J.J. Investigating CT to CBCT image registration for head and neck proton therapy as a tool for daily dose recalculation. *Medical Physics.* 2015, **42**(3), pp.1354-1366.

36. Veiga, C., McClelland, J., Moinuddin, S., Lourenço, A., Ricketts, K., Annkah, J., Modat, M., Ourselin, S., D'Souza, D. and Royle, G. Toward adaptive radiotherapy for head and neck patients: feasibility study on using CT-to-CBCT deformable registration for "dose of the day" calculations. *Medical Physics.* 2014, **41**(3), p.031703.

37. Delaney, G., Jacob, S., Featherstone, C. and Barton, M. The role of radiotherapy in cancer treatment: estimating optimal utilization from a review of evidence-based clinical guidelines. *Cancer: Interdisciplinary International Journal of the American Cancer Society.* 2005, **104**(6), pp.1129-1137.

38. Barton, M.B., Jacob, S., Shafiq, J., Wong, K., Thompson, S.R., Hanna, T.P. and Delaney, G.P. Estimating the demand for radiotherapy from the evidence: a review of changes from 2003 to 2012. *Radiotherapy and Oncology.* 2014, **112**(1), pp.140-144.

39. Baskar, R., Lee, K.A., Yeo, R. and Yeoh, K.-W. Cancer and radiation therapy: current advances and future directions. *International journal of medical sciences.* 2012, **9**(3), p.193.

40. Vujošević, B. and Bokorov, B. Radiotherapy: past and present. *Archive of oncology.* 2010, **18**(4), pp.140-142.

41. Norlund, A. Costs of radiotherapy. *Acta Oncologica.* 2003, **42**(5-6), pp.411-415.

42. Cullen, J., Drabble, D., Castellanos, C. and Brissett, L. Recommendations for achieving a world-class radiotherapy service in the UK. *The Tavistock Institute.* 2019.

43. Washington, C.M. and Leaver, D.T. *Principles and practice of radiation therapy-e-book.* Elsevier Health Sciences, 2015.

44. Skliarenko, J. and Warde, P. Radiotherapy: practical applications and clinical aspects. *Medicine.* 2011, **39**(12), pp.705-710.

45. Valentini, V., Boldrini, L., Mariani, S. and Massaccesi, M. Role of radiation oncology in modern multidisciplinary cancer treatment. *Molecular Oncology.* 2020, **14**(7), pp.1431-1441.

46. Tsechanski, A., Bielajew, A., Archambault, J. and Mainegra-Hing, E. Electron accelerator-based production of molybdenum-99: Bremsstrahlung and photoneutron generation from molybdenum vs. tungsten. *Nuclear Instruments and Methods in Physics Research Section B: Beam Interactions with Materials and Atoms.* 2016, **366**, pp.124-139.

47. Chang, D.S., Lasley, F.D., Das, I.J., Mendonca, M.S. and Dynlacht, J.R. *Basic radiotherapy physics and biology.* Second Edition ed. Springer, 2021.

48. Shahid, W., Mukhtar, R., Rizvi, S.F.A., Shahid, S. and Iqbal, M.A. Evaluation and validation of tungsten fiducial marker-based image-guided radiotherapy. *Biomedical Physics & Engineering Express.* 2021, **7**(3), p.035014.

49. Cherry, P. and Duxbury, A.M. *Practical radiotherapy: physics and equipment.* John Wiley & Sons, 2019.

50. Veldeman, L., Madani, I., Hulstaert, F., De Meerleer, G., Mareel, M. and De Neve, W. Evidence behind use of intensity-modulated radiotherapy: a systematic review of comparative clinical studies. *The lancet oncology.* 2008, **9**(4), pp.367-375.

51. DiBartolo, D., Carpenter, T., Santoro, J.P., Lischalk, J.W., Ebling, D., Haas, J.A., Witten, M., Rybstein, M., Vaezi, A. and Repka, M.C. Novel VMAT planning technique improves dosimetry for head and neck cancer patients undergoing definitive chemoradiotherapy. *Acta Oncologica.* 2023, **62**(2), pp.189-193.

52. Palma, D.A., Verbakel, W.F., Otto, K. and Senan, S. New developments in arc radiation therapy: a review. *Cancer treatment reviews.* 2010, **36**(5), pp.393-399.

53. Lecchi, M., Fossati, P., Elisei, F., Orecchia, R. and Lucignani, G. Current concepts on imaging in radiotherapy. *European journal of nuclear medicine and molecular imaging.* 2008, **35**, pp.821-837.

54. García-Figueiras, R., Baleato-González, S., Luna, A., Padhani, A.R., Vilanova, J.C., Carballo-Castro, A.M., Oleaga-Zufiria, L., Vallejo-Casas, J.A., Marhuenda, A. and Gómez-Caamaño, A. How Imaging Advances Are Defining the Future of Precision Radiation Therapy. *Radiographics.* 2024, **44**(2), p.e230152.

55. Ash, D., Andrews, B. and Stubbs, B. A method for integrating computed tomography into radiotherapy planning and treatment. *Clinical Radiology.* 1983, **34**(1), pp.99-101.

56. Essers, M., Mesch, L., Beugeling, M., Dekker, J. and de Kruijf, W. Setup and intra-fractional motion measurements using surface scanning in head and neck cancer radiotherapy–A feasibility study. *Physics and imaging in radiation oncology.* 2024, **29**, p.100563.

57. Good, D., Lo, J., Lee, W.R., Wu, Q.J., Yin, F.-F. and Das, S.K. A knowledge-based approach to improving and homogenizing intensity modulated radiation therapy planning quality among treatment centers: an example application to prostate cancer planning. *International Journal of Radiation Oncology* Biology* Physics.* 2013, **87**(1), pp.176-181.

58. Jones, D. *ICRU report 50—prescribing, recording and reporting photon beam therapy*. Wiley Online Library. 1994.

59. Wambersie, A. ICRU report 62, prescribing, recording and reporting photon beam therapy (supplement to ICRU Report 50). *Icru News.* 1999.

60. Chavaudra, J. and Bridier, A. Definition of volumes in external radiotherapy: ICRU reports 50 and 62. *Cancer Radiotherapie: Journal de la Societe Francaise de Radiotherapie Oncologique.* 2001, **5**(5), pp.472-478.

61. Noël, G., Le Fèvre, C. and Antoni, D. Delineation of organs at risk. *Cancer/Radiothérapie.* 2022, **26**(1-2), pp.76-91.

62. ICRU. Prescribing, recording, and reporting photon-beam intensitymodulated radiation therapy (IMRT). ICRU Report 83. *Journal of the International Commission on Radiation Units and Measurements.* 2010, **10**(1), p.106.

63. Dionisi, F., Fiorica, F., D'Angelo, E., Maddalo, M., Giacomelli, I., Tornari, E., Rosca, A., Vigo, F., Romanello, D. and Cianchetti, M. Organs at risk's tolerance and dose limits for head and neck cancer re-irradiation: A literature review. *Oral oncology.* 2019, **98**, pp.35-47.

64. Brock, K.K. and Dawson, L.A. Point: principles of magnetic resonance imaging integration in a computed tomography–based radiotherapy workflow. In: *Seminars in radiation oncology*: Elsevier, 2014, pp.169-174.

65. Davis, A.T., Palmer, A.L. and Nisbet, A. Can CT scan protocols used for radiotherapy treatment planning be adjusted to optimize image quality and patient dose? A systematic review. *The British journal of radiology.* 2017, **90**(1076), p.20160406.

66. Simard, M., Bär, E., Blais, D. and Bouchard, H. Electron density and effective atomic number estimation in a maximum a posteriori framework for dual-energy computed tomography. *Medical Physics.* 2020, **47**(9), pp.4137-4149.

67. Nakao, M., Ozawa, S., Yogo, K., Miura, H., Yamada, K., Hosono, F., Hayata, M., Miki, K., Nakashima, T. and Ochi, Y. Tolerance levels of mass density for CT number calibration in photon radiation therapy. *Journal of Applied Clinical Medical Physics.* 2019, **20**(6), pp.45-52.

68. De Martino, F., Clemente, S., Graeff, C., Palma, G. and Cella, L. Dose calculation algorithms for external radiation therapy: an overview for practitioners. *Applied sciences.* 2021, **11**(15), p.6806.

69. Aisen, A.M., Martel, W., Braunstein, E.M., McMillin, K.I., Phillips, W.A. and Kling, T. MRI and CT evaluation of primary bone and soft-tissue tumors. *American Journal of Roentgenology.* 1986, **146**(4), pp.749-756.

70. Torresin, A., Brambilla, M.G., Monti, A.F., Moscato, A., Brockmann, M.A., Schad, L., Attenberger, U.I. and Lohr, F. Review of potential improvements using MRI in the radiotherapy workflow. *Zeitschrift für Medizinische Physik.* 2015, **25**(3), pp.210-220.

71. Gach, H.M., Curcuru, A.N., Mutic, S. and Kim, T. B0 field homogeneity recommendations, specifications, and measurement units for MRI in radiation therapy. *Medical Physics.* 2020, **47**(9), pp.4101-4114.

72. Rezaee, M. and Letourneau, D. Assessment of image quality and dosimetric performance of CT simulators. *Journal of medical imaging and radiation sciences.* 2019, **50**(2), pp.297-307.

73. Pereira, G.C., Traughber, M. and Muzic, R.F. The role of imaging in radiation therapy planning: past, present, and future. *BioMed research international.* 2014, **2014**.

74. Nhila, O., Talbi, M., El Mansouri, M.h., El Katib, M. and Chakir, E.M. Evaluation of CT acquisition protocols effect on hounsfield units and optimization of CT-RED calibration curve selection in radiotherapy treatment planning systems. *Moscow University Physics Bulletin.* 2022, **77**(4), pp.661-671.

75. Perez, J.R., Lee, S., Ybarra, N., Maria, O., Serban, M., Jeyaseelan, K., Wang, L.M., Seuntjens, J. and Naqa, I.E. A comparative analysis of longitudinal computed tomography and histopathology for evaluating the potential of mesenchymal stem cells in mitigating radiation-induced pulmonary fibrosis. *Scientific Reports.* 2017, **7**(1), p.9056.

76. Park, J.K. and Pope, W. Computed Tomography Imaging of Brain Tumors. *Multi-Detector CT Imaging: Principles, Head, Neck, and Vascular Systems.* 2013, p.173.

77. Srinivasan, K. and Kanakaraj, J. A review on potential issues and challenges in MR imaging. *The Scientific World Journal.* 2013, **2013**.

78. Serai, S.D. Basics of magnetic resonance imaging and quantitative parameters T1, T2, T2*, T1rho and diffusion-weighted imaging. *Pediatric Radiology.* 2022, **52**(2), pp.217-227.

79. Storey, P. Introduction to magnetic resonance imaging and spectroscopy. *Magnetic Resonance Imaging: Methods and Biologic Applications.* 2006, pp.3-57.

80. Hodgson, R.J. (v) The basic science of MRI. *Orthopaedics and Trauma.* 2011, **25**(2), pp.119-130.

81. Berger, A. How does it work?: Magnetic resonance imaging. *BMJ: British Medical Journal.* 2002, **324**(7328), p.35.

82. Hanson, L.G. *Introduction to magnetic resonance imaging techniques.* Danish Research Centre for Magnetic Resonance (DRCMR), 2009.

83. Westbrook, C. and Talbot, J. *MRI in Practice.* John Wiley & Sons, 2018.

84. Wehrli, F.W., Song, H.K., Saha, P.K. and Wright, A.C. Quantitative MRI for the assessment of bone structure and function. *NMR in Biomedicine: An International Journal Devoted to the Development and Application of Magnetic Resonance In vivo.* 2006, **19**(7), pp.731-764.

85. Fullerton, G.D. The magic angle effect in NMR and MRI of cartilage. 2016.

86. Zukauskaite, R., Rumley, C.N., Hansen, C.R., Jameson, M.G., Trada, Y., Johansen, J., Gyldenkerne, N., Eriksen, J.G., Aly, F. and Christensen, R.L. Delineation uncertainties of tumour volumes on MRI of head and neck cancer patients. *Clinical and Translational Radiation Oncology.* 2022, **36**, pp.121-126.

87. López, F., Mäkitie, A., de Bree, R., Franchi, A., de Graaf, P., Hernández-Prera, J.C., Strojan, P., Zidar, N., Strojan Fležar, M. and Rodrigo, J.P. Qualitative and quantitative diagnosis in head and neck cancer. *Diagnostics.* 2021, **11**(9), p.1526.

88. Mukherjee, S., Fischbein, N.J., Baugnon, K.L., Policeni, B.A. and Raghavan, P. Contemporary imaging and reporting strategies for head and neck cancer: MRI, FDG PET/MRI, NI-RADS, and carcinoma of unknown primary—AJR Expert Panel Narrative Review. *American Journal of Roentgenology.* 2023, **220**(2), pp.160-172.

89. Deoni, S.C., Rutt, B.K. and Peters, T.M. Rapid combined T1 and T2 mapping using gradient recalled acquisition in the steady state. *Magnetic Resonance in Medicine: An Official Journal of the International Society for Magnetic Resonance in Medicine.* 2003, **49**(3), pp.515-526.

90. Brateman, L. Chemical shift imaging: a review. *American Journal of Roentgenology.* 1986, **146**(5), pp.971-980.

91. Wei, D., Ahmad, S., Huo, J., Peng, W., Ge, Y., Xue, Z., Yap, P.-T., Li, W., Shen, D. and Wang, Q. Synthesis and inpainting-based mr-ct registration for image-guided thermal ablation of liver tumors. In: *Medical Image Computing and Computer Assisted Intervention–MICCAI 2019: 22nd International Conference, Shenzhen, China, October 13–17, 2019, Proceedings, Part V 22*: Springer, 2019, pp.512-520.

92. Rong, Y., Rosu-Bubulac, M., Benedict, S.H., Cui, Y., Ruo, R., Connell, T., Kashani, R., Latifi, K., Chen, Q. and Geng, H. Rigid and deformable image registration for radiation therapy: a self-study evaluation guide for NRG oncology clinical trial participation. *Practical Radiation Oncology.* 2021, **11**(4), pp.282-298.

93. Maya, A.T., Suryono, S. and Anam, C. Image contrast improvement in image fusion between CT and MRI images of brain cancer patients. *Int. J. Sci. Res. Sci. Technol.* 2021, **8**(1), pp.104-110.

94. Metcalfe, P., Liney, G., Holloway, L., Walker, A., Barton, M., Delaney, G., Vinod, S. and Tome, W. The potential for an enhanced role for MRI in radiation-therapy treatment planning. *Technology in cancer research & treatment.* 2013, **12**(5), pp.429-446.

95. Greer, P., Martin, J., Sidhom, M., Hunter, P., Pichler, P., Choi, J.H., Best, L., Smart, J., Young, T. and Jameson, M. A multi-center prospective study for implementation of an MRI-only prostate treatment planning workflow. *Frontiers in oncology.* 2019, **9**, p.826.

96. Yu, H., Oliver, M., Leszczynski, K., Lee, Y., Karam, I. and Sahgal, A. Tissue segmentation-based electron density mapping for MR-only radiotherapy treatment planning of brain using conventional T1-weighted MR images. *Journal of Applied Clinical Medical Physics.* 2019, **20**(8), pp.11-20.

97. Ilamurugu, A. and Chandrasekaran, A.R. The rationale for MR-only delineation and planning: retrospective CT–MR registration and target volume analysis for prostate radiotherapy. *Journal of Radiotherapy in Practice.* 2021, **20**(3), pp.265-272.

98. Johnstone, E., Wyatt, J.J., Henry, A.M., Short, S.C., Sebag-Montefiore, D., Murray, L., Kelly, C.G., McCallum, H.M. and Speight, R. Systematic review of synthetic computed tomography generation methodologies for use in magnetic resonance imaging–only radiation therapy. *International Journal of Radiation Oncology* Biology* Physics.* 2018, **100**(1), pp.199-217.

99. Gonzalez-Moya, A., Dufreneix, S., Ouyessad, N., Guilleriminet, C. and Autret, D. Evaluation of a commercial synthetic computed tomography generation solution for magnetic resonance imaging-only radiotherapy. *Journal of Applied Clinical Medical Physics.* 2021, **22**(6), pp.191-197.

100. Edmund, J.M. and Nyholm, T. A review of substitute CT generation for MRI-only radiation therapy. *Radiation Oncology.* 2017, **12**(1), p.28.

101. Jonsson, J., Nyholm, T. and Söderkvist, K. The rationale for MR-only treatment planning for external radiotherapy. *Clinical and Translational Radiation Oncology.* 2019, **18**, pp.60-65.

102. Owrangi, A.M., Greer, P.B. and Glide-Hurst, C.K. MRI-only treatment planning: benefits and challenges. *Physics in Medicine & Biology.* 2018, **63**(5), p.05TR01.

103. Wiesinger, F. and Ho, M.-L. Zero-TE MRI: principles and applications in the head and neck. *The British journal of radiology.* 2022, **95**(1136), p.20220059.

104. Dowling, J., O'Connor, L., Acosta, O., Raniga, P., de Crevoisier, R., Nunes, J.-C., Barateau, A., Chourak, H., Choi, J.H. and Greer, P. Image synthesis for MRI-only radiotherapy treatment planning. In: *Biomedical Image Synthesis and Simulation*.   Elsevier, 2022, pp.423-445.

105. Williams, J.P. and Newhauser, W. Normal tissue damage: its importance, history and challenges for the future. *The British journal of radiology.* 2018, **92**(1093), p.20180048.

106. Hawley, L. Principles of radiotherapy. *British Journal of Hospital Medicine.* 2013, **74**(Sup11), pp.C166-C169.

107. Lindegaard, A.M., Håkansson, K., Bernsdorf, M., Gothelf, A.B., Kristensen, C.A., Specht, L., Vogelius, I.R. and Friborg, J. A systematic review on clinical adaptive radiotherapy for head and neck cancer. *Acta Oncologica.* 2023, **62**(11), pp.1360-1368.

108. Pauwels, R., Araki, K., Siewerdsen, J. and Thongvigitmanee, S.S. Technical aspects of dental CBCT: state of the art. *Dentomaxillofacial Radiology.* 2015, **44**(1), p.20140224.

109. Elekta Solutions AB. *Elekta Medical Linear Accelerator Instructions for Use Volume 3 - XVI for: Elekta Synergy®, Elekta Infinity™, Versa HD™.* 2022.

110. Belotti, G., Fattori, G., Baroni, G. and Rit, S. Extension of the cone-beam CT field-of-view using two complementary short scans. *Medical Physics.* 2024, **51**(5), pp.3391-3404.

111. Irmak, S., Georg, D. and Lechner, W. Comparison of CBCT conversion methods for dose calculation in the head and neck region. *Zeitschrift für Medizinische Physik.* 2020, **30**(4), pp.289-299.

112. Siewerdsen, J.H. and Jaffray, D.A. Cone-beam computed tomography with a flat-panel imager: magnitude and effects of x-ray scatter. *Medical Physics.* 2001, **28**(2), pp.220-231.

113. Poludniowski, G.G., Evans, P.M. and Webb, S. Cone beam computed tomography number errors and consequences for radiotherapy planning: an investigation of correction methods. *International Journal of Radiation Oncology* Biology* Physics.* 2012, **84**(1), pp.e109-e114.

114. Montanari, D., Scolari, E., Silvestri, C., Graves, Y.J., Yan, H., Cervino, L., Rice, R., Jiang, S.B. and Jia, X. Comprehensive evaluations of cone-beam CT dose in image-guided radiation therapy via GPU-based Monte Carlo simulations. *Physics in Medicine & Biology.* 2014, **59**(5), p.1239.

115. World Health Organization (WHO). *Quality Assurance in Radiotherapy Geneva: WHO.* 1988.

116. Institute of Physical Sciences in Medicine. *IPEM report 54: Commissioning and Quality Assurance of Linear Accelerators.* 1988.

117. Papakostidi, A., Tolia, M. and Tsoukalas, N. Quality assurance in Health Services: the paradigm of radiotherapy. *J BUON.* 2014, **19**(1), pp.47-52.

118. Taneja, S., Barbee, D.L., Rea, A.J. and Malin, M. CBCT image quality QA: Establishing a quantitative program. *Journal of Applied Clinical Medical Physics.* 2020, **21**(11), pp.215-225.

119. Yea, J.W., Park, J.W., Kim, S.K., Kim, D.Y., Kim, J.G., Seo, C.Y., Jeong, W.H., Jeong, M.Y. and Oh, S.A. Feasibility of a 3D-printed anthropomorphic patient-specific head phantom for patient-specific quality assurance of intensity-modulated radiotherapy. *PloS one.* 2017, **12**(7), p.e0181560.

120. McGarry, C.K., Grattan, L.J., Ivory, A.M., Leek, F., Liney, G.P., Liu, Y., Miloro, P., Rai, R., Robinson, A.P. and Shih, A.J. Tissue mimicking materials for imaging and therapy phantoms: a review. *Physics in Medicine & Biology.* 2020, **65**(23), p.23TR01.

121. Gharzai, L.A., Rosen, B.S., Mittal, B., Mierzwa, M.L. and Yadav, P. Magnetic resonance guided radiotherapy for head and neck cancers. *Journal of Clinical Medicine.* 2022, **11**(5), p.1388.

122. Filippou, V. and Tsoumpas, C. Recent advances on the development of phantoms using 3D printing for imaging with CT, MRI, PET, SPECT, and ultrasound. *Medical Physics.* 2018, **45**(9), pp.e740-e760.

123. Tino, R., Yeo, A., Leary, M., Brandt, M. and Kron, T. A systematic review on 3D-printed imaging and dosimetry phantoms in radiation therapy. *Technology in cancer research & treatment.* 2019, **18**, p.1533033819870208.

124. Crasto, N., Kirubarajan, A. and Sussman, D. Anthropomorphic brain phantoms for use in MRI systems: a systematic review. *Magnetic Resonance Materials in Physics, Biology and Medicine.* 2022, **35**(2), pp.277-289.

125. White, D. The design and manufacture of anthropomorphic phantoms. *Radiation protection dosimetry.* 1993, **49**(1-3), pp.359-369.

126. CIRS. *MRI Distortion Phantom for SRS.* [Online]. 2014. [Accessed 08 Feb 2024]. Available from: http://www.cirsinc.com/wp-content/uploads/2020/07/603A-DS-072220.pdf

127. Hadi, I., Roengvoraphoj, O., Bodensohn, R., Hofmaier, J., Niyazi, M., Belka, C. and Nachbichler, S.B. Stereotactic radiosurgery combined with targeted/immunotherapy in patients with melanoma brain metastasis. *Radiation Oncology.* 2020, **15**(1), pp.1-11.

128. Price, R.G., Kim, J.P., Zheng, W., Chetty, I.J. and Glide-Hurst, C. Image guided radiation therapy using synthetic computed tomography images in brain cancer. *International Journal of Radiation Oncology* Biology* Physics.* 2016, **95**(4), pp.1281-1289.

129. Chung, H.T., Park, W.Y., Kim, T.H., Kim, Y.K. and Chun, K.J. Assessment of the accuracy and stability of frameless gamma knife radiosurgery. *Journal of Applied Clinical Medical Physics.* 2018, **19**(4), pp.148-154.

130. CIRS. *Phantom Patient for Stereotactic End-to-End Verification.* [Online]. 2013. [Accessed 05 Jan 2024]. Available from:

https://www.sunnuclear.com/uploads/documents/datasheets/038-PB-032423-2.pdf

131. Rousseau, A., Stien, C., Gouriou, J., Bordy, J.-M., Boissonnat, G., Chabert, I., Dufreneix, S. and Blideanu, V. End-to-end quality assurance for stereotactic radiotherapy with Fricke-Xylenol orange-Gelatin gel dosimeter and dual-wavelength cone-beam optical CT readout. *Physica Medica.* 2023, **113**, p.102656.

132. Standard Imaging. *MAX-HD.* [Online]. 2024. [Accessed 23 Jan 2024]. Available from: https://www.imtqa.com/products/max-hd

133. Standard Imaging. *MAX-HD 2.0.* [Online]. 2024. [Accessed 23 Jan 2024]. Available from: https://www.imtqa.com/products/max-hd-2-0

134. Standard Imaging. *LUCY™ MR MR-Guided SRS QA Phantom.* [Online]. 2024. [Accessed 27 July 2024]. Available from: https://www.standardimaging.com/products/lucy-mr#tab-5

135. RT Safe. *Prime End-to-End quality assurance of challenging SRS applications.* [Online]. 2020. [Accessed 02 August 2020]. Available from: https://rt-safe.com/wp-content/uploads/2020/12/Specs.pdf

136. Makris, D., Pappas, E., Zoros, E., Papanikolaou, N., Saenz, D., Kalaitzakis, G., Zourari, K., Efstathopoulos, E., Maris, T. and Pappas, E. Characterization of a novel 3D printed patient specific phantom for quality assurance in cranial stereotactic radiosurgery applications. *Physics in Medicine and Biology.* 2019, **64**(10), p.105009.

137. Chen, S.J.S., Hellier, P., Marchal, M., Gauvrit, J.Y., Carpentier, R., Morandi, X. and Collins, D.L. An anthropomorphic polyvinyl alcohol brain phantom based on Colin27 for use in multimodal imaging. *Medical Physics.* 2012, **39**(1), pp.554-561.

138. Gallas, R.R., Hünemohr, N., Runz, A., Niebuhr, N.I., Jäkel, O. and Greilich, S. An anthropomorphic multimodality (CT/MRI) head phantom prototype for end-to-end tests in ion radiotherapy. *Zeitschrift fuer Medizinische Physik.* 2015, **25**(4), pp.391-399.

139. Soliman, A.S., Burns, L., Owrangi, A., Lee, Y., Song, W.Y., Stanisz, G. and Chugh, B.P. A realistic phantom for validating MRI-based synthetic CT images of the human skull. *Medical Physics.* 2017, **44**(9), pp.4687-4694.

140. Steinmann, A., Alvarez, P., Lee, H., Court, L., Stafford, R., Sawakuchi, G., Wen, Z., Fuller, C.D. and Followill, D. MRIgRT head and neck anthropomorphic QA phantom: Design, development, reproducibility, and feasibility study. *Medical Physics.* 2020, **47**(2), pp.604-613.

141. De Deene, Y., Wheatley, M., Greig, T., Hayes, D., Ryder, W. and Loh, H. A multi-modality medical imaging head and neck phantom: Part 1. Design and fabrication. *Physica Medica.* 2022, **96**, pp.166-178.

142. Wells, M. and Goldstein, L. The Role of Phantoms and Simulation in Teaching Ultrasound Skills in Emergency Medicine. 2017.

143. Mille, M.M., Griffin, K.T., Maass-Moreno, R. and Lee, C. Fabrication of a pediatric torso phantom with multiple tissues represented using a dual nozzle thermoplastic 3D printer. *Journal of Applied Clinical Medical Physics.* 2020.

144. Zhang, H., Hou, K., Chen, J., Dyer, B.A., Chen, J.-C., Liu, X., Zhang, F., Rong, Y. and Qiu, J. Fabrication of an anthropomorphic heterogeneous mouse phantom for multimodality medical imaging. *Physics in Medicine & Biology.* 2018, **63**(19), p.195011.

145. Khaledi, N., Khan, R. and Gräfe, J.L. Historical Progress of Stereotactic Radiation Surgery. *Journal of Medical Physics.* 2023, **48**(4), pp.312-327.

146. Dimitriadis, A., Palmer, A.L., Thomas, R.A., Nisbet, A. and Clark, C.H. Adaptation and validation of a commercial head phantom for cranial radiosurgery dosimetry end-to-end audit. *The British journal of radiology.* 2017, **90**(1074), p.20170053.

147. Nierer, L., Kamp, F., Reiner, M., Corradini, S., Rabe, M., Dietrich, O., Parodi, K., Belka, C., Kurz, C. and Landry, G. Evaluation of an anthropomorphic ion chamber and 3D gel dosimetry head phantom at a 0.35 T MR-linac using separate 1.5 T MR-scanners for gel readout. *Zeitschrift für Medizinische Physik.* 2022, **32**(3), pp.312-325.

148. Knight, S.P., Browne, J.E., Meaney, J.F., Smith, D.S. and Fagan, A.J. A novel anthropomorphic flow phantom for the quantitative evaluation of prostate DCE-MRI acquisition techniques. *Physics in Medicine and Biology.* 2016, **61**(20), p.7466.

149. Hoffmans, D., Niebuhr, N., Bohoudi, O., Pfaffenberger, A. and Palacios, M. An end-to-end test for MR-guided online adaptive radiotherapy. *Physics in Medicine & Biology.* 2020, **65**(12), p.125012.

150. Niebuhr, N., Johnen, W., Echner, G., Runz, A., Bach, M., Stoll, M., Giske, K., Greilich, S. and Pfaffenberger, A. The ADAM-pelvis phantom—an anthropomorphic, deformable and multimodal phantom for MRgRT. *Physics in Medicine & Biology.* 2019, **64**(4), p.04NT05.

151. Battista, J.J., Rider, W.D. and Van Dyk, J. Computed tomography for radiotherapy planning. *International Journal of Radiation Oncology* Biology* Physics.* 1980, **6**(1), pp.99-107.

152. Dirix, P., Haustermans, K. and Vandecaveye, V. The value of magnetic resonance imaging for radiotherapy planning. In: *Seminars in radiation oncology*: Elsevier, 2014, pp.151-159.

153. Tan, J., Lim Joon, D., Fitt, G., Wada, M., Lim Joon, M., Mercuri, A., Marr, M., Chao, M. and Khoo, V. The utility of multimodality imaging with CT and MRI in defining rectal tumour volumes for radiotherapy treatment planning: a pilot study. *Journal of Medical Imaging and Radiation Oncology.* 2010, **54**(6), pp.562-568.

154. Đan, I., Petrović, B., Erak, M., Nikolić, I. and Lučić, S. Radiotherapy treatment planning: benefits of CT-MR image registration and fusion in tumor volume delineation. *Vojnosanitetski pregled.* 2013, **70**(8), pp.735-739.

155. Niebuhr, N.I., Johnen, W., Güldaglar, T., Runz, A., Echner, G., Mann, P., Möhler, C., Pfaffenberger, A., Jäkel, O. and Greilich, S. radiological properties of tissue surrogates used in a multimodality deformable pelvic phantom for MR-guided radiotherapy. *Medical Physics.* 2016, **43**(2), pp.908-916.

156. Cunningham, J.M. and Glide-Hurst, C.K. End-to-end phantom evaluation for transition from MR/CT combined to MR-Only workflow. 2017.

157. Johnen, W., Niebuhr, N., Runz, A. and Echner, G. The ADAM-pelvis phantom: from DICOM data to a patient-like model. *Radiother Oncol.* 2018, **127**, p.S930.

158. Litt, H.I. and Brody, A.S. BaSO4-loaded agarose: a construction material for multimodality imaging phantoms. *Academic radiology.* 2001, **8**(5), pp.377-383.

159. Mutic, S., Dempsey, J.F., Bosch, W.R., Low, D.A., Drzymala, R.E., Chao, K.C., Goddu, S.M., Cutler, P.D. and Purdy, J.A. Multimodality image

registration quality assurance for conformal three-dimensional treatment planning. *International Journal of Radiation Oncology* Biology* Physics.* 2001, **51**(1), pp.255-260.

160. Daisne, J.-F., Sibomana, M., Bol, A., Cosnard, G., Lonneux, M. and Grégoire, V. Evaluation of a multimodality image (CT, MRI and PET) coregistration procedure on phantom and head and neck cancer patients: accuracy, reproducibility and consistency. *Radiotherapy and Oncology.* 2003, **69**(3), pp.237-245.

161. Young, J., Shahedi, M., Dormer, J.D., Johnson, B., Gahan, J. and Fei, B. A low-cost PVC-based dual-modality kidney phantom. In: *Medical Imaging 2022: Image-Guided Procedures, Robotic Interventions, and Modeling*: SPIE, 2022, pp.639-647.

162. Cloutier, M., Harnagea, C., Hale, P., Seddiki, O., Rosei, F. and Mantovani, D. Long-term stability of hydrogenated DLC coatings: Effects of aging on the structural, chemical and mechanical properties. *Diamond and related materials.* 2014, **48**, pp.65-72.

163. DeWerd, L.A. and Smith, B.R. Calorimetry. In: *Radiation Therapy Dosimetry: A Practical Handbook*.   CRC Press, 2021, pp.31-38.

164. Chmarra, M.K., Hansen, R., Mårvik, R. and Langø, T. Multimodal phantom of liver tissue. *PloS One.* 2013, **8**(5), p.e64180.

165. He, Y., Qin, S., Dyer, B.A., Zhang, H., Zhao, L., Chen, T., Zheng, F., Sun, Y., Shi, L. and Rong, Y. Characterizing mechanical and medical imaging properties of polyvinyl chloride-based tissue-mimicking materials. *Journal of Applied Clinical Medical Physics.* 2019, **20**(7), pp.176-183.

166. Ruschin, M., Davidson, S.R., Phounsy, W., Yoo, T.S., Chin, L., Pignol, J.P., Ravi, A. and McCann, C. Multipurpose CT, ultrasound, and MRI breast phantom for use in radiotherapy and minimally invasive interventions. *Medical Physics.* 2016, **43**(5), pp.2508-2514.

167. Vargas, J., Le, P., Shahedi, M., Gahan, J., Johnson, B., Dormer, J.D., Shahub, S., Pfefferle, M., Judson, B.O. and Alshara, Y. A complex dual-modality kidney phantom for renal biopsy studies. In: *Medical Imaging 2020: Ultrasonic Imaging and Tomography*: SPIE, 2020, pp.105-110.

168. He, Y., Liu, Y., Dyer, B.A., Boone, J.M., Liu, S., Chen, T., Zheng, F., Zhu, Y., Sun, Y. and Rong, Y. 3D-printed breast phantom for multi-purpose and multi-modality imaging. *Quantitative imaging in medicine and surgery.* 2019, **9**(1), p.63.

169. Surry, K., Austin, H., Fenster, A. and Peters, T. Poly (vinyl alcohol) cryogel phantoms for use in ultrasound and MR imaging. *Physics in Medicine & Biology.* 2004, **49**(24), p.5529.

170. Orr, T.N., Winter, J., Campbell, G., Thompson, R.T. and Gelman, N. A Phantom Material for Mri of the Neonatal Brain. *CMBES Proceedings.* 2007, **30**.

171. Mano, I., Goshima, H., Nambu, M. and Iio, M. New polyvinyl alcohol gel material for MRI phantoms. *Magnetic Resonance in Medicine.* 1986, **3**(6), pp.921-926.

172. Taghizadeh, S., Labuda, C. and Mobley, J. Development of a tissue-mimicking phantom of the brain for ultrasonic studies. *Ultrasound in Medicine & Biology.* 2018, **44**(12), pp.2813-2820.

173. Yee, Y., Tee, H., Azhar, N.A.A., Abdul Manan, H., Awang, M.N.A. and Yusoff, A.N. T1 and T2 characteristics of poly (vinyl) alcohol slime

phantom with different relaxation modifier concentrations. *Solid State Sci Technol.* 2019, **27**(1 & 2), pp.105-121.

174. Radiation Products Design, I. *Super Stuff Bolus.* [Online]. 2021. [Accessed]. Available from: https://www.rpdinc.com/super-stuff-bolus-10-pound-bucket-1723.html

175. Humimic Medical. *Material Safety Data Sheet (MSDS)* [Online]. 2016. [Accessed 04 March 2023]. Available from: https://humimic.com/material-safety-data-sheet-msds/

176. Humimic Medical. *Medical Gels.* [Online]. 2023. [Accessed 04 March 2023]. Available from: https://humimic.com/product-category/medical-gels/medical-gels-medical-gels/

177. Smooth-On. *Silicone Rubber - Platinum Cure.* [Online]. 2023. [Accessed 04 March 2023]. Available from: https://www.smooth-on.com/category/platinum-silicone/

178. Polytek Development Corp. *Products.* [Online]. 2023. [Accessed 03 March 2023]. Available from: https://polytek.com/products/

179. R. Varges, P., M. Costa, C., S. Fonseca, B., F. Naccache, M. and de Souza Mendes, P.R. Rheological characterization of carbopol® dispersions in water and in water/glycerol solutions. *Fluids.* 2019, **4**(1), p.3.

180. Bojorquez, J.Z., Bricq, S., Acquitter, C., Brunotte, F., Walker, P.M. and Lalande, A. What are normal relaxation times of tissues at 3 T? *Magnetic resonance imaging.* 2017, **35**, pp.69-80.

181. Pileggi, G., Speier, C., Sharp, G.C., Izquierdo Garcia, D., Catana, C., Pursley, J., Amato, F., Seco, J. and Spadea, M.F. Proton range shift analysis on brain pseudo-CT generated from T1 and T2 MR. *Acta Oncologica.* 2018, **57**(11), pp.1521-1531.

182. Cho, T.A., Bhattacharyya, S. and Helfgott, S. *Neurorheumatology: A Comprehenisve Guide to Immune Mediated Disorders of the Nervous System.* Springer, 2019.

183. Anderson, S.W., Soto, J.A., Sakai, O. and Jara, H. Adaptive Iterative T2 Mapping with Maximum Pearson Correlation in the Presence of Noise. In: *Proc. Intl. Soc. Mag. Reson. Med*, 2011, p.4557.

184. Veit, M., Perrin, R., Siti, M. and Sylvain, D. Magnetic resonance imaging for brain stereotactic radiotherapy. *Strahlentherapie und Onkologie.* 2020, **196**(5), pp.444-456.

185. Shetty, A.S., Sipe, A.L., Zulfiqar, M., Tsai, R., Raptis, D.A., Raptis, C.A. and Bhalla, S. In-phase and opposed-phase imaging: applications of chemical shift and magnetic susceptibility in the chest and abdomen. *Radiographics.* 2019, **39**(1), pp.115-135.

186. Marcu, L.G. and Marcu, D. The role of hypofractionated radiotherapy in the management of head and neck cancer–a modelling approach. *Journal of theoretical biology.* 2019, **482**, p.109998.

187. Birkl, C., Langkammer, C., Golob-Schwarzl, N., Leoni, M., Haybaeck, J., Goessler, W., Fazekas, F. and Ropele, S. Effects of formalin fixation and temperature on MR relaxation times in the human brain. *NMR in Biomedicine.* 2016, **29**(4), pp.458-465.

188. Captur, G., Gatehouse, P., Keenan, K.E., Heslinga, F.G., Bruehl, R., Prothmann, M., Graves, M.J., Eames, R.J., Torlasco, C. and Benedetti, G. A medical device-grade T1 and ECV phantom for global T1 mapping quality assurance—the T 1 Mapping and ECV Standardization in

cardiovascular magnetic resonance (T1MES) program. *Journal of Cardiovascular Magnetic Resonance.* 2016, **18**, pp.1-20.

189. Kudo, H., Mukai, N., Gouping, C., Numanno, T., Honma, K., Tateishi, T., Miyanaga, Y. and Miyakawa, S. The evaluation of collagen gel with various connection states by using MRI. *Materials Science and Engineering: C.* 2008, **28**(2), pp.270-273.

190. Guo, T., Ma, Y., Jerban, S., Jang, H., Zhao, W., Chang, E.Y., Chen, M., Bydder, G.M. and Du, J. T1 measurement of bound water in cortical bone using 3D adiabatic inversion recovery ultrashort echo time (3D IR-UTE) Cones imaging. *Magnetic Resonance in Medicine.* 2020, **84**(2), pp.634-645.

191. Mafee, M.F., Rapoport, M., Karimi, A., Ansari, S.A. and Shah, J. Orbital and ocular imaging using 3-and 1.5-T MR imaging systems. *Neuroimaging Clinics.* 2005, **15**(1), pp.1-21.

192. Stanisz, G.J., Odrobina, E.E., Pun, J., Escaravage, M., Graham, S.J., Bronskill, M.J. and Henkelman, R.M. T1, T2 relaxation and magnetization transfer in tissue at 3T. *Magnetic Resonance in Medicine: An Official Journal of the International Society for Magnetic Resonance in Medicine.* 2005, **54**(3), pp.507-512.

193. Mishra, S., Bajpai, R., Katare, R. and Bajpai, A. Radiation induced crosslinking effect on semi-interpenetrating polymer networks of poly (vinyl alcohol). *Express polymer letters.* 2007, **1**(7), pp.407-415.

194. Seo, M.-K., Rhee, K.-Y. and Park, S.-J. Influence of electro-beam irradiation on PTC/NTC behaviors of carbon blacks/HDPE conducting polymer composites. *Current Applied Physics.* 2011, **11**(3), pp.428-433.

195. Kim, H., Hong, H., Park, J. and Lee, A.L. Intracranial migration of intravitreal silicone oil: a case report. *Clinical neuroradiology.* 2016, **26**, pp.93-95.

196. Hashemi, S., Kandala, S.K., Agbo, B., Colwell, Z.A., Song, K., Xie, R. and Sohn, S.-M. Flexible, stretchable, and MR-invisible dielectric material for magnetic resonance imaging. *IEEE Journal of Electromagnetics, RF and Microwaves in Medicine and Biology.* 2023.

197. Bley, T.A., Wieben, O., François, C.J., Brittain, J.H. and Reeder, S.B. Fat and water magnetic resonance imaging. *Journal of Magnetic Resonance Imaging.* 2010, **31**(1), pp.4-18.

198. Tsukiashi, A., Min, K.S., Kitayama, H., Terasawa, H., Yoshinaga, S., Takeda, M., Lindoy, L.F. and Hayami, S. Application of spin-crossover water soluble nanoparticles for use as MRI contrast agents. *Scientific Reports.* 2018, **8**(1), p.14911.

199. Keenan, K.E., Ainslie, M., Barker, A.J., Boss, M.A., Cecil, K.M., Charles, C., Chenevert, T.L., Clarke, L., Evelhoch, J.L. and Finn, P. Quantitative magnetic resonance imaging phantoms: a review and the need for a system phantom. *Magnetic Resonance in Medicine.* 2018, **79**(1), pp.48-61.

200. Jackson, E., Bronskill, M., Drost, D., Och, J., Pooley, R., Sobol, W. and Clarke, G. Acceptance testing and quality assurance procedures for magnetic resonance imaging facilities. *American Association of Physicists in Medicine One Physics Ellipse College Park.* 2010.

201. Price, R., Allison, J., Clarke, G., Dennis, M., Hendrick, R., Keener, C., Masten, J., Nessaiver, M., Och, J. and Reeve, D. Magnetic resonance imaging quality control manual. *American College of Radiology.* 2015.

202. McRobbie, D. and Semple, S. Quality control and artefacts in magnetic resonance imaging. *IPEM Report.* 2017, **112**, pp.164-165.

203. Lennie, E., Tsoumpas, C. and Sourbron, S. Multimodal phantoms for clinical PET/MRI. *EJNMMI physics.* 2021, **8**(1), pp.1-24.

204. Molineu, A., Followill, D.S., Balter, P.A., Hanson, W.F., Gillin, M.T., Huq, M.S., Eisbruch, A. and Ibbott, G.S. Design and implementation of an anthropomorphic quality assurance phantom for intensity-modulated radiation therapy for the Radiation Therapy Oncology Group. *International Journal of Radiation Oncology* Biology* Physics.* 2005, **63**(2), pp.577-583.

205. Molineu, A., Hernandez, N., Nguyen, T., Ibbott, G. and Followill, D. Credentialing results from IMRT irradiations of an anthropomorphic head and neck phantom. *Medical physics.* 2013, **40**(2), p.022101.

206. Wood, S., Krishnamurthy, N., Santini, T., Raval, S., Farhat, N., Holmes, J.A. and Ibrahim, T.S. Design and fabrication of a realistic anthropomorphic heterogeneous head phantom for MR purposes. *PloS one.* 2017, **12**(8), p.e0183168.

207. Badiuk, S.R., Sasaki, D.K. and Rickey, D.W. An anthropomorphic maxillofacial phantom using 3-dimensional printing, polyurethane rubber and epoxy resin for dental imaging and dosimetry. *Dentomaxillofacial Radiology.* 2022, **51**(1), p.20200323.

208. Followill, D.S., Evans, D.R., Cherry, C., Molineu, A., Fisher, G., Hanson, W.F. and Ibbott, G.S. Design, development, and implementation of the radiological physics center's pelvis and thorax anthropomorphic quality assurance phantoms. *Medical physics.* 2007, **34**(6Part1), pp.2070-2076.

209. Hazelaar, C., van Eijnatten, M., Dahele, M., Wolff, J., Forouzanfar, T., Slotman, B. and Verbakel, W.F. Using 3D printing techniques to create an anthropomorphic thorax phantom for medical imaging purposes. *Medical physics.* 2018, **45**(1), pp.92-100.

210. Adjeiwaah, M., Garpebring, A. and Nyholm, T. Sensitivity analysis of different quality assurance methods for magnetic resonance imaging in radiotherapy. *Physics and imaging in radiation oncology.* 2020, **13**, pp.21-27.

211. Lewis, B.C., Shin, J., Maraghechi, B., Quinn, B., Cole, M., Barberi, E., Kim, J.S., Green, O. and Kim, T. Assessment of a novel commercial large field of view phantom for comprehensive MR imaging quality assurance of a 0.35 T MRgRT system. *Journal of Applied Clinical Medical Physics.* 2022, **23**(4), p.e13535.

212. Alliance, Q.I.B. QIBA profile: Diffusion-weighted magnetic resonance imaging (DWI). *Profile consensus (QIBA, 2019).* 2020.

213. Miften, M., Olch, A., Mihailidis, D., Moran, J., Pawlicki, T., Molineu, A., Li, H., Wijesooriya, K., Shi, J. and Xia, P. Tolerance limits and methodologies for IMRT measurement-based verification QA: recommendations of AAPM Task Group No. 218. *Medical physics.* 2018, **45**(4), pp.e53-e83.

214. Speight, R., Schmidt, M.A., Liney, G.P., Johnstone, R.I., Eccles, C.L., Dubec, M., George, B., Henry, A. and McCallum, H. IPEM topical report: a 2018 IPEM survey of MRI use for external beam radiotherapy treatment planning in the UK. *Physics in Medicine & Biology.* 2019, **64**(17), p.175021.

215. Speight, R., Tyyger, M., Schmidt, M.A., Liney, G., Johnstone, R., Eccles, C.L., Dubec, M., George, B., Henry, A. and Herbert, T. IPEM Topical

Report: An international IPEM survey of MRI use for external beam radiotherapy treatment planning. *Physics in Medicine & Biology.* 2021, **66**(7), p.075007.

216. Gach, H.M. T1 and T2 and complex permittivities of mineral oil, silicone oil, and glycerol at 0.35, 1.5, and 3 T. *Medical physics.* 2019, **46**(4), pp.1785-1792.

217. Lesch, A.J. Quantification of T1, T2 and Pseudo Spin Density using bSSFP with Correction for Non-Ideal Flip Angle Profiles. 2014.

218. Rueden, C.T., Schindelin, J., Hiner, M.C., DeZonia, B.E., Walter, A.E., Arena, E.T. and Eliceiri, K.W. ImageJ2: ImageJ for the next generation of scientific image data. *BMC bioinformatics.* 2017, **18**, pp.1-26.

219. McMahon, K.L., Cowin, G. and Galloway, G. Magnetic resonance imaging: the underlying principles. *journal of orthopaedic & sports physical therapy.* 2011, **41**(11), pp.806-819.

220. Mazaheri, Y., Vargas, H.A., Nyman, G., Akin, O. and Hricak, H. Image artifacts on prostate diffusion-weighted magnetic resonance imaging: trade-offs at 1.5 Tesla and 3.0 Tesla. *Academic radiology.* 2013, **20**(8), pp.1041-1047.

221. Winter, R.M., Leibfarth, S., Schmidt, H., Zwirner, K., Mönnich, D., Welz, S., Schwenzer, N.F., la Fougère, C., Nikolaou, K. and Gatidis, S. Assessment of image quality of a radiotherapy-specific hardware solution for PET/MRI in head and neck cancer patients. *Radiotherapy and Oncology.* 2018, **128**(3), pp.485-491.

222. Brock, K.K., Mutic, S., McNutt, T.R., Li, H. and Kessler, M.L. Use of image registration and fusion algorithms and techniques in radiotherapy: Report of the AAPM Radiation Therapy Committee Task Group No. 132. *Medical physics.* 2017, **44**(7), pp.e43-e76.

223. Sahoo, N., Sawakuchi, G.O., Gillin, M.T. and Zhu, X.R. Radiation Dosimetry of Proton Beams. *Particle Radiotherapy: Emerging Technology for Treatment of Cancer.* 2016, pp.77-94.

224. De Los Santos, J., Popple, R., Agazaryan, N., Bayouth, J.E., Bissonnette, J.-P., Bucci, M.K., Dieterich, S., Dong, L., Forster, K.M. and Indelicato, D. Image guided radiation therapy (IGRT) technologies for radiation therapy localization and delivery. *International journal of radiation oncology, biology, physics.* 2013, **87**(1), pp.33-45.

225. Maund, I., Benson, R., Fairfoul, J., Cook, J., Huddart, R. and Poynter, A. Image-guided radiotherapy of the prostate using daily CBCT: the feasibility and likely benefit of implementing a margin reduction. *The British journal of radiology.* 2015, **87**(1045), p.20140459.

226. Ding, G.X. and Munro, P. Radiation exposure to patients from image guidance procedures and techniques to reduce the imaging dose. *Radiotherapy and Oncology.* 2013, **108**(1), pp.91-98.

227. Chargari, C., Goodman, K.A., Diallo, I., Guy, J.-B., Rancoule, C., Cosset, J.-M., Deutsch, E. and Magne, N. Risk of second cancers in the era of modern radiation therapy: does the risk/benefit analysis overcome theoretical models? *Cancer and Metastasis Reviews.* 2016, **35**, pp.277-288.

228. Wood, T., Moore, C., Saunderson, J. and Beavis, A. Validation of a technique for estimating organ doses for kilovoltage cone-beam CT of the prostate using the PCXMC 2.0 patient dose calculator. *Journal of Radiological Protection.* 2015, **35**(1), p.153.

229. Sykes, J., Lindsay, R., Iball, G. and Thwaites, D. Dosimetry of CBCT: methods, doses and clinical consequences. In: *Journal of Physics: Conference Series*: IOP Publishing, 2013, p.012017.

230. Khan, M., Sandhu, N., Naeem, M., Ealden, R., Pearson, M., Ali, A., Honey, I., Webster, A., Eaton, D. and Ntentas, G. Implementation of a comprehensive set of optimised CBCT protocols and validation through imaging quality and dose audit. *The British journal of radiology.* 2022, **95**(1139), p.20220070.

231. Martin, C., Kron, T., Vassileva, J., Wood, T., Joyce, C., Ung, N., Small, W., Gros, S., Roussakis, Y. and Plazas, M. An international survey of imaging practices in radiotherapy. *Physica Medica.* 2021, **90**, pp.53-65.

232. Alaei, P. and Spezi, E. Imaging dose from cone beam computed tomography in radiation therapy. *Physica Medica.* 2015, **31**(7), pp.647-658.

233. Ding, G.X., Alaei, P., Curran, B., Flynn, R., Gossman, M., Mackie, T.R., Miften, M., Morin, R., Xu, X.G. and Zhu, T.C. Image guidance doses delivered during radiotherapy: quantification, management, and reduction: report of the AAPM Therapy Physics Committee Task Group 180. *Medical physics.* 2018, **45**(5), pp.e84-e99.

234. Ding, G.X., Duggan, D.M., Coffey, C.W., Deeley, M., Hallahan, D.E., Cmelak, A. and Malcolm, A. A study on adaptive IMRT treatment planning using kV cone-beam CT. *Radiotherapy and Oncology.* 2007, **85**(1), pp.116-125.

235. Nijkamp, J., Pos, F.J., Nuver, T.T., De Jong, R., Remeijer, P., Sonke, J.-J. and Lebesque, J.V. Adaptive radiotherapy for prostate cancer using kilovoltage cone-beam computed tomography: first clinical results. *International Journal of Radiation Oncology* Biology* Physics.* 2008, **70**(1), pp.75-82.

236. Foroudi, F., Wong, J., Kron, T., Rolfo, A., Haworth, A., Roxby, P., Thomas, J., Herschtal, A., Pham, D. and Williams, S. Online adaptive radiotherapy for muscle-invasive bladder cancer: results of a pilot study. *International Journal of Radiation Oncology* Biology* Physics.* 2011, **81**(3), pp.765-771.

237. Zhang, G.-s., Huang, S.-m., Chen, C., Zhang, D.-d. and Deng, X.-w. A Method to Convert Cone-Beam Computed Tomography (CBCT) Image for Dose Calculation and the Phantom Evaluation. In: *World Congress on Medical Physics and Biomedical Engineering, June 7-12, 2015, Toronto, Canada*: Springer, 2015, pp.372-372.

238. Liu, Y., Lei, Y., Wang, T., Fu, Y., Tang, X., Curran, W.J., Liu, T., Patel, P. and Yang, X. CBCT-based synthetic CT generation using deep-attention cycleGAN for pancreatic adaptive radiotherapy. *Medical physics.* 2020, **47**(6), pp.2472-2483.

239. Liu, J., Yan, H., Cheng, H., Liu, J., Sun, P., Wang, B., Mao, R., Du, C. and Luo, S. CBCT-based synthetic CT generation using generative adversarial networks with disentangled representation. *Quantitative imaging in medicine and surgery.* 2021, **11**(12), p.4820.

240. Chen, L., Liang, X., Shen, C., Nguyen, D., Jiang, S. and Wang, J. Synthetic CT generation from CBCT images via unsupervised deep learning. *Physics in Medicine & Biology.* 2021, **66**(11), p.115019.

241. Li, J., Yao, W., Xiao, Y. and Yu, Y. Feasibility of improving cone-beam CT number consistency using a scatter correction algorithm. *Journal of Applied Clinical Medical Physics.* 2013, **14**(6), pp.167-176.
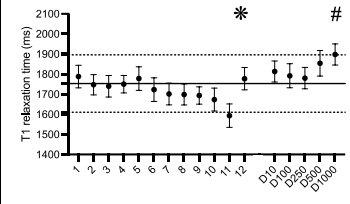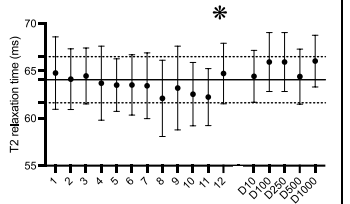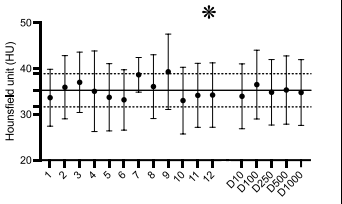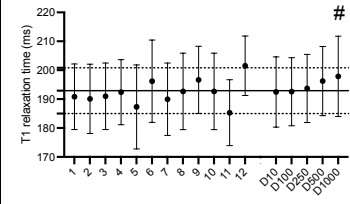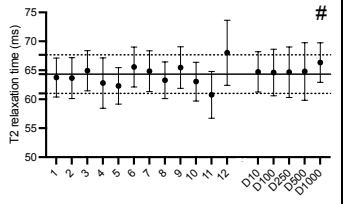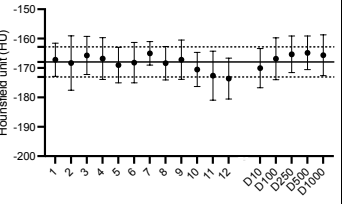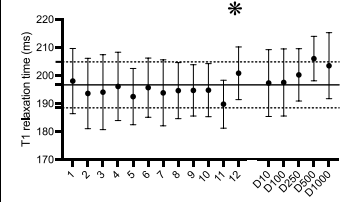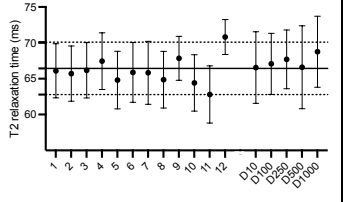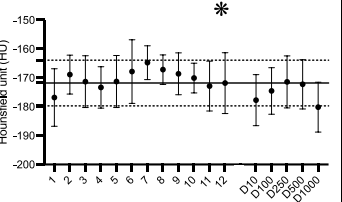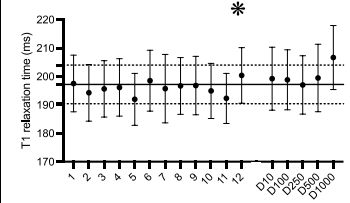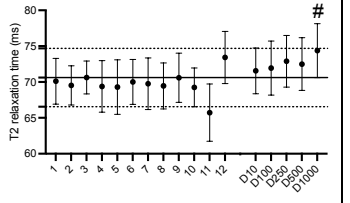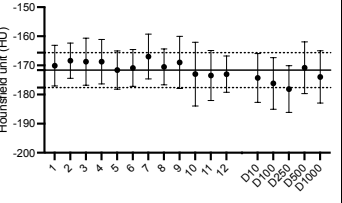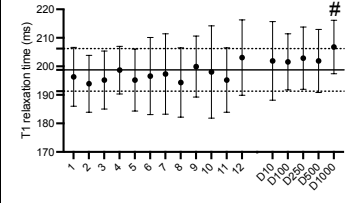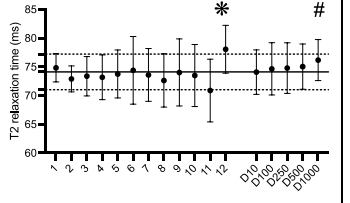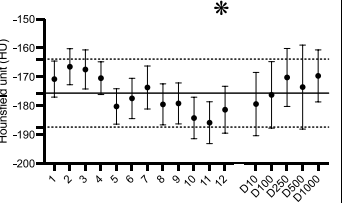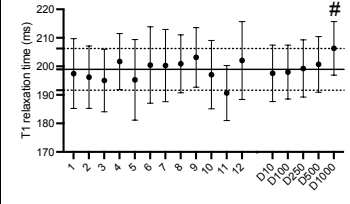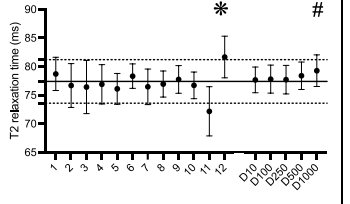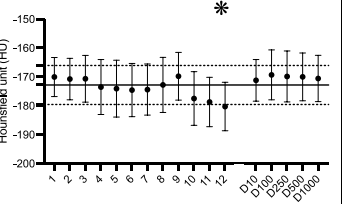
242. Agnew, C.E., McCallum, C., Johnston, G., Workman, A. and Irvine, D.M. Optimisation of Varian TrueBeam head, thorax and pelvis CBCT based on patient size. *Journal of Radiotherapy in Practice.* 2021, **20**(3), pp.248-256.

243. Yan, H., Cervino, L., Jia, X. and Jiang, S.B. A comprehensive study on the relationship between the image quality and imaging dose in low-dose cone beam CT. *Physics in Medicine & Biology.* 2012, **57**(7), p.2063.

244. Tomic, N., Devic, S., DeBlois, F. and Seuntjens, J. Reference radiochromic film dosimetry in kilovoltage photon beams during CBCT image acquisition. *Medical physics.* 2010, **37**(3), pp.1083-1092.

245. Cheng, H.C., Wu, V.W., Liu, E.S. and Kwong, D.L. Evaluation of radiation dose and image quality for the Varian cone beam computed tomography system. *International Journal of Radiation Oncology* Biology* Physics.* 2011, **80**(1), pp.291-300.

246. Giaddui, T., Cui, Y., Galvin, J., Yu, Y. and Xiao, Y. Comparative dose evaluations between XVI and OBI cone beam CT systems using Gafchromic XRQA2 film and nanoDot optical stimulated luminescence dosimeters. *Medical physics.* 2013, **40**(6Part1), p.062102.

247. Moon, Y.M., Kim, H.-J., Kwak, D.W., Kang, Y.-R., Lee, M.W., Ro, T.-I., Kim, J.K. and Jeong, D.H. Effective dose measurement for cone beam computed tomography using glass dosimeter. *Nuclear Engineering and Technology.* 2014, **46**(2), pp.255-262.

248. Nobah, A., Aldelaijan, S., Devic, S., Tomic, N., Seuntjens, J., Al-Shabanah, M. and Moftah, B. Radiochromic film based dosimetry of image-guidance procedures on different radiotherapy modalities. *Journal of Applied Clinical Medical Physics.* 2014, **15**(6), pp.229-239.

249. Gwet, K.L. Computing inter-rater reliability and its variance in the presence of high agreement. *British Journal of Mathematical and Statistical Psychology.* 2008, **61**(1), pp.29-48.

250. Gwet, K.L. *Handbook of inter-rater reliability: The definitive guide to measuring the extent of agreement among raters.* Advanced Analytics, LLC, 2014.

251. Savi, M., Villani, D., Andrade, B., Soares, F., Rodrigues Jr, O., Campos, L. and Potiens, M. Step-by-step of 3D printing a head-and-neck phantom: Proposal of a methodology using fused filament fabrication (FFF) technology. *Radiation Physics and Chemistry.* 2024, **223**, p.111965.

252. Pereira, D.D., Cardoso, S.C., Batista, D.V., de Souza, F.M., de Sousa, J.V., Gonçalves, O.D. and da Rosa, L.A. Development of an anthropomorphic phantom based on 3D printing for assessment of dose delivered to the eye and adjacent tissues. *Radiation Physics and Chemistry.* 2022, **199**, p.110292.

253. Candemil, A.P., Salmon, B., Freitas, D.Q., Ambrosano, G.M., Haiter-Neto, F. and Oliveira, M.L. Metallic materials in the exomass impair cone beam CT voxel values. *Dentomaxillofacial Radiology.* 2018, **47**(6), p.20180011.

254. Men, K., Dai, J.-R., Li, M.-H., Chen, X.-Y., Zhang, K., Tian, Y., Huang, P. and Xu, Y.-J. A method to improve electron density measurement of cone-beam CT using dual energy technique. *BioMed research international.* 2015, **2015**.
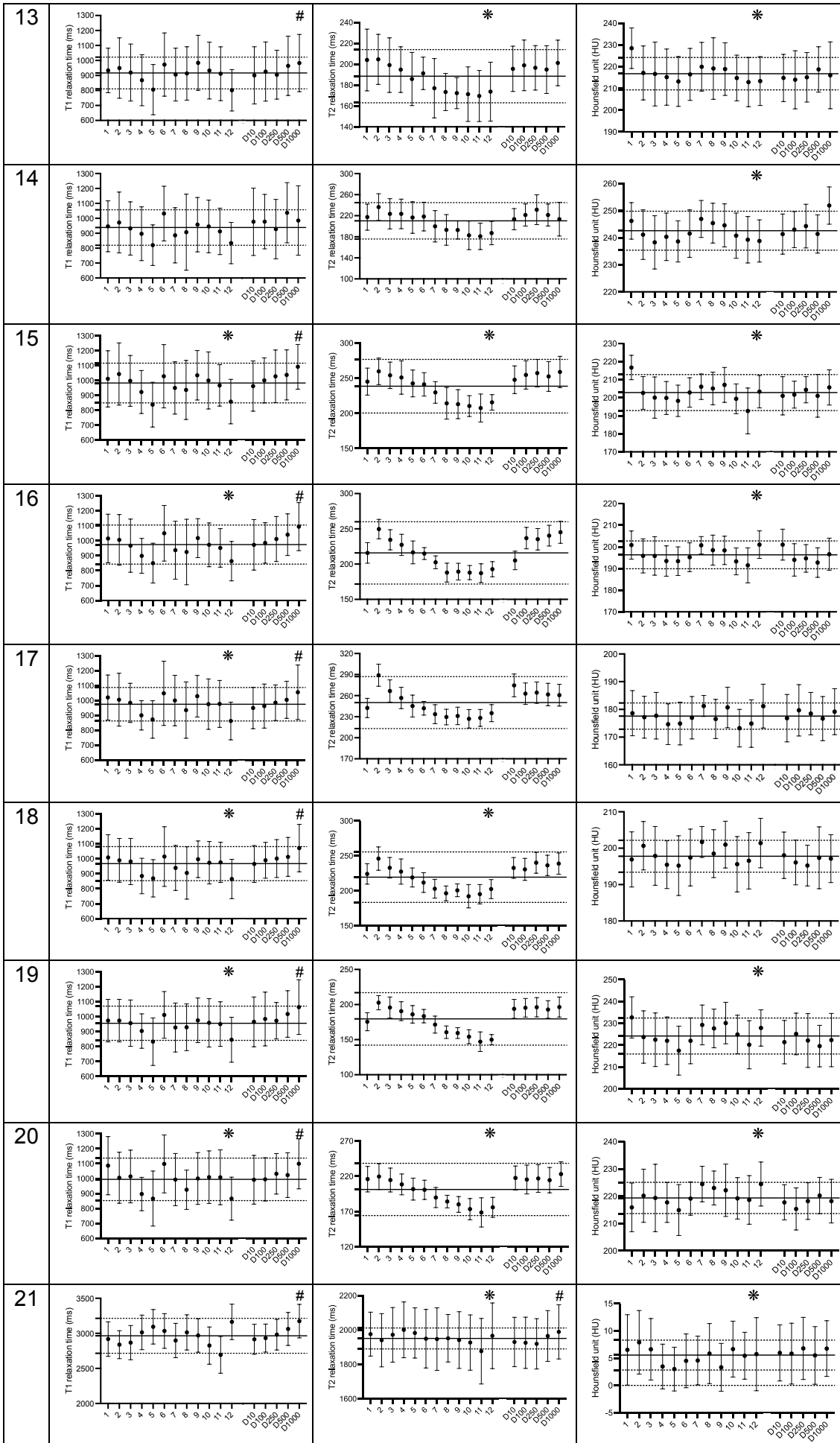
255. Srinivasan, K., Mohammadi, M. and Shepherd, J. Applications of linac-mounted kilovoltage Cone-beam Computed Tomography in modern radiation therapy: A review. *Polish journal of radiology.* 2014, **79**, p.181.

256. Zhao, W., Vernekohl, D., Zhu, J., Wang, L. and Xing, L. A model-based scatter artifacts correction for cone beam CT. *Medical physics.* 2016, **43**(4), pp.1736-1753.

Appendices

Appendix 1

This appendix complements the results presented in Chapter 4 by containing the results for materials that were assessed but deemed unsuitable as candidates for simulating H&N tissues in MRI and CT scans. These include detailed data on their CT numbers, T1 and T2 relaxation times, and statistical analysis outcomes.

205

Figure. T1 (left) and T2 (middle) relaxation times and Hounsfield unit (right) values over time and radiation exposure. Mean values (circle) and their standard deviations (error bars) are displayed for Materials 3-23. Numbers denote monthly measurements, and D(x) indicates the radiation dose, where x is the dose received by the sample in Gray. Across all measurements, the solid line is the mean, and the dashed black lines are ± 2 SD. Any measurements that demonstrated a statistically significant change compared to the baseline is highlighted with ✳ or # for changes over time or dose respectively.

Appendix 2

This appendix complements the results presented in Chapter 4 by providing the T1 and T2 relaxation times for the remaining tubes in the T1MES phantom.
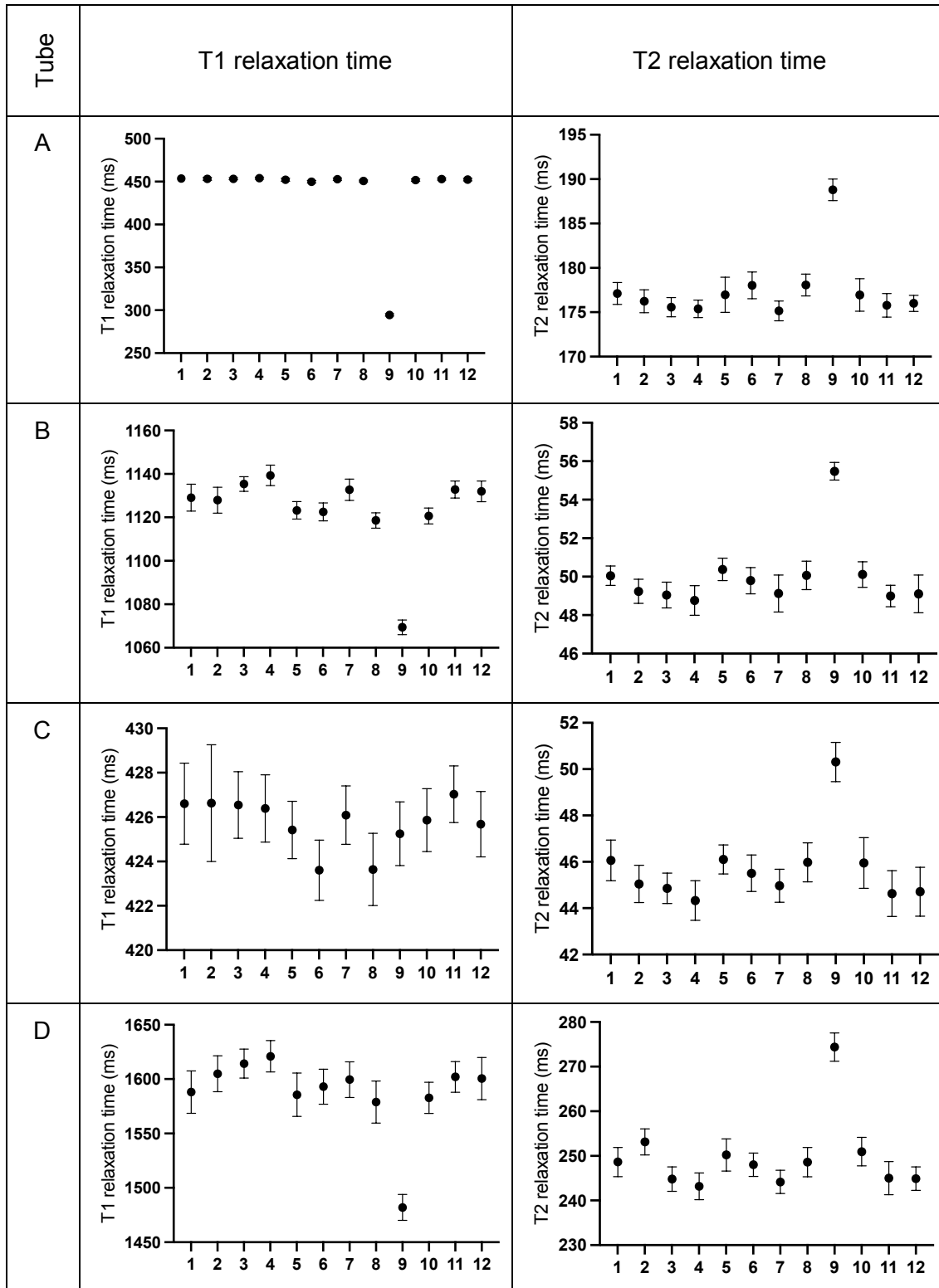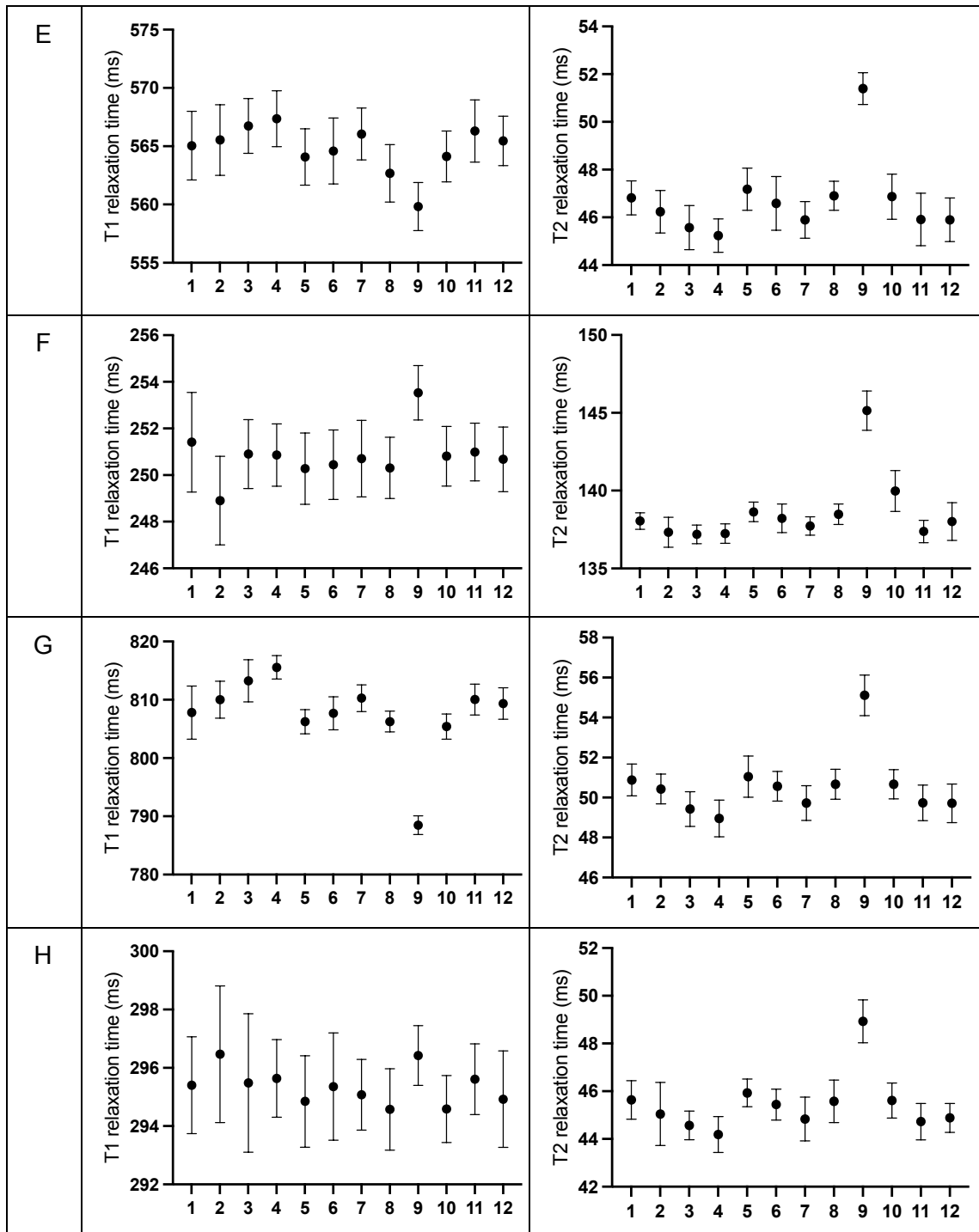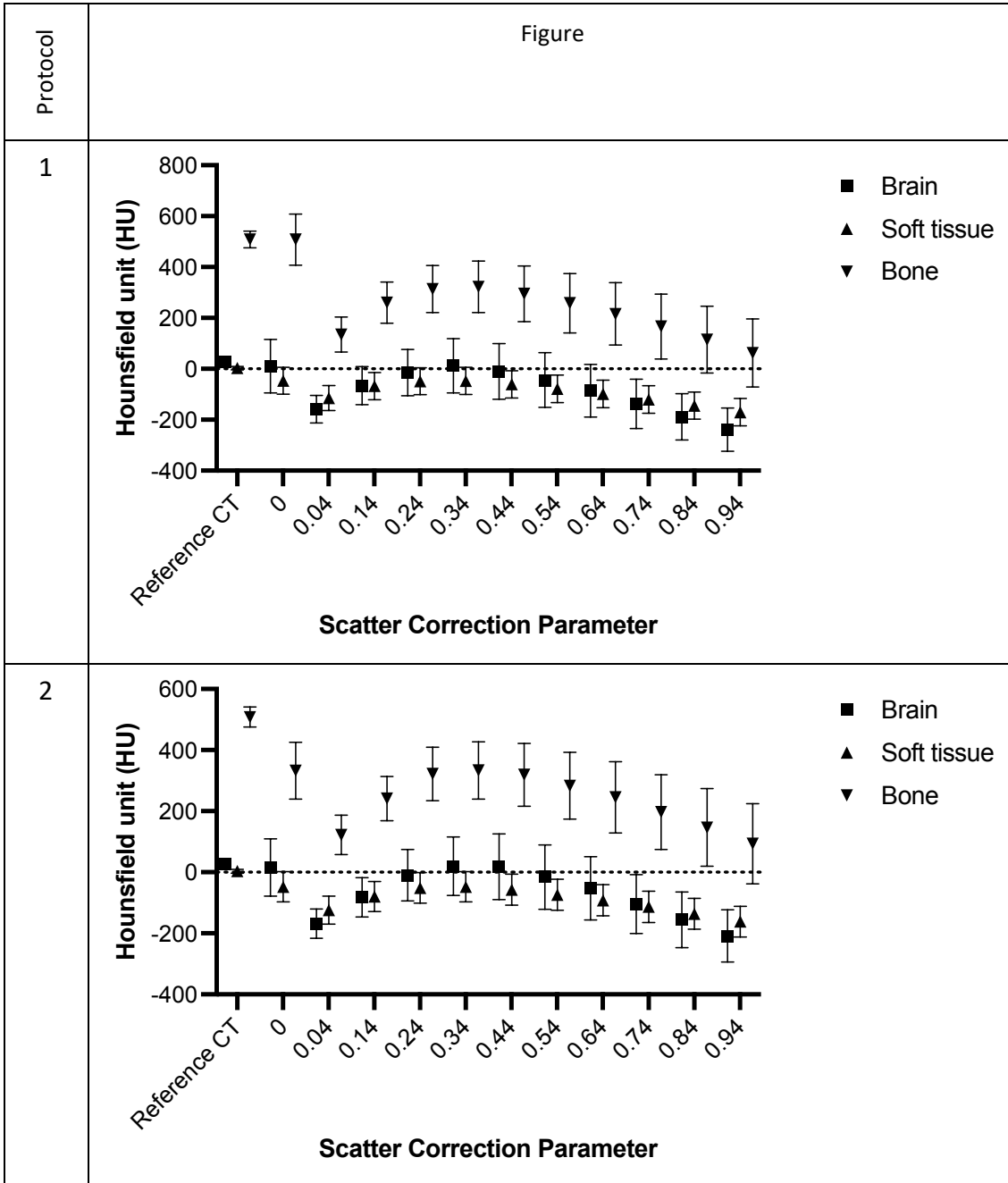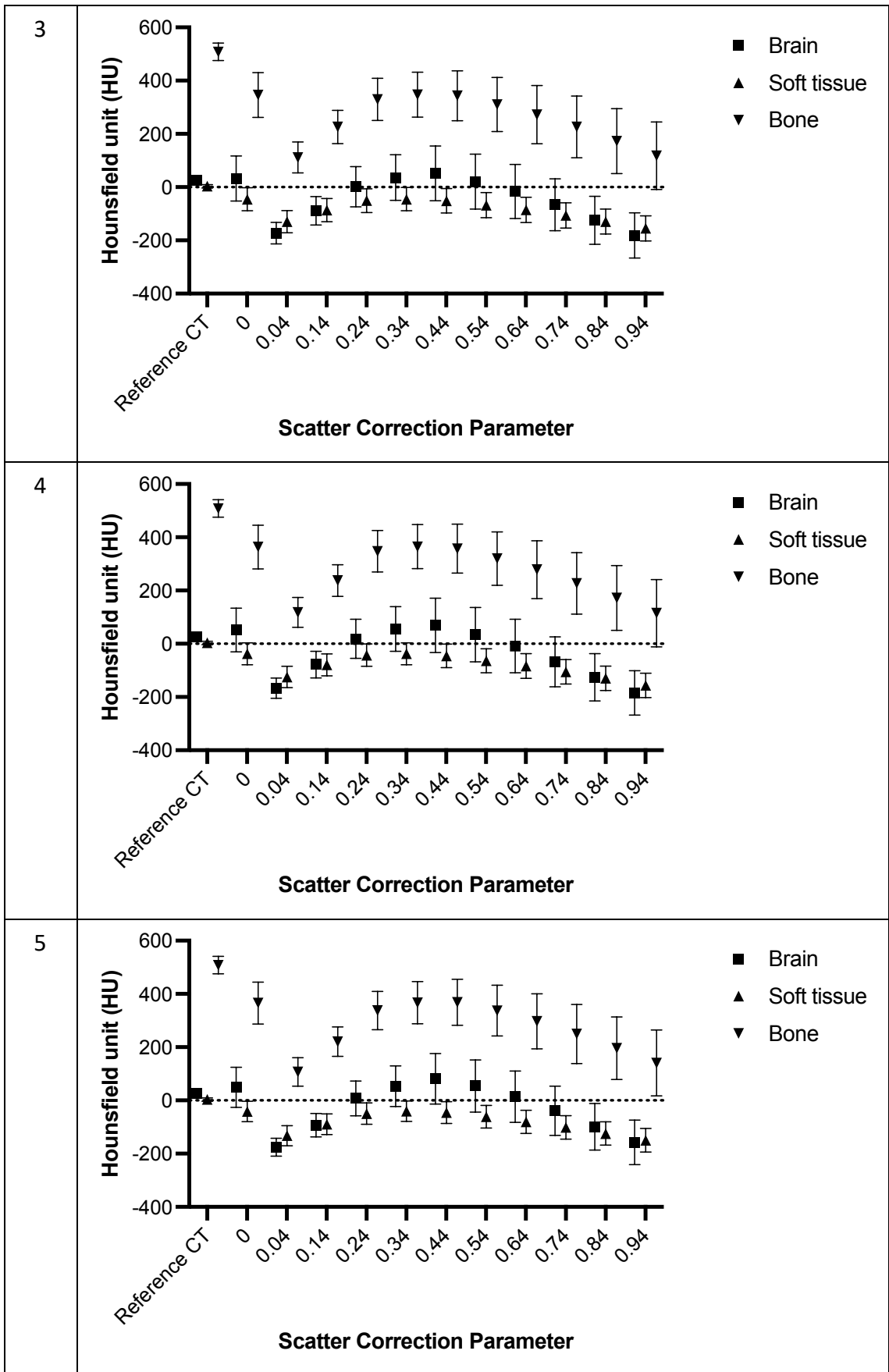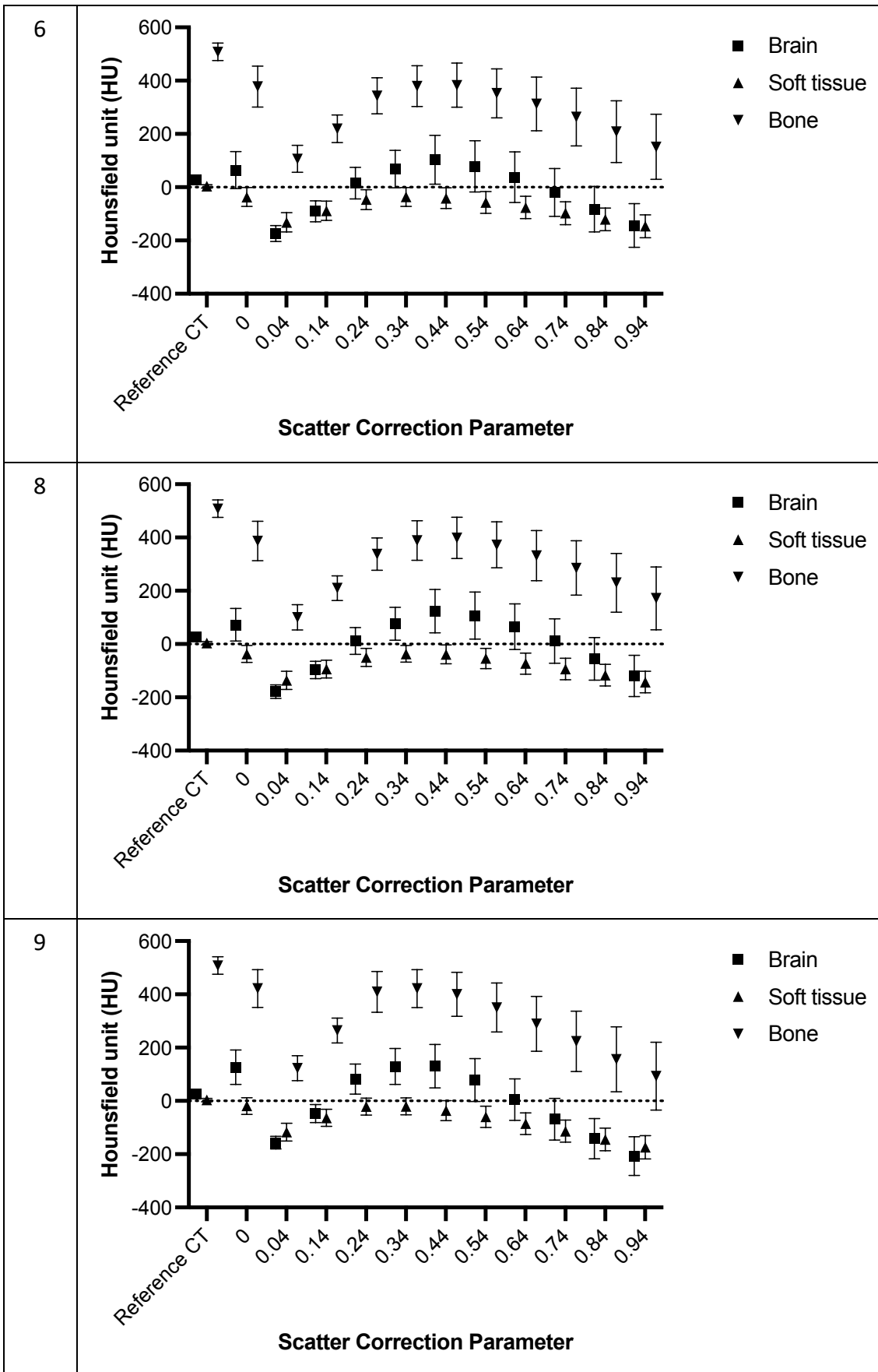
Figure. Mean T1 and T2 relaxation times (circle) and standard deviations (SD, error bars) across the voxels within the regions of interest for all tubes in the T1MES phantom. Solid lines denote the average of the mean values over time. Dashed black lines are ± 2 SD.

Appendix 3

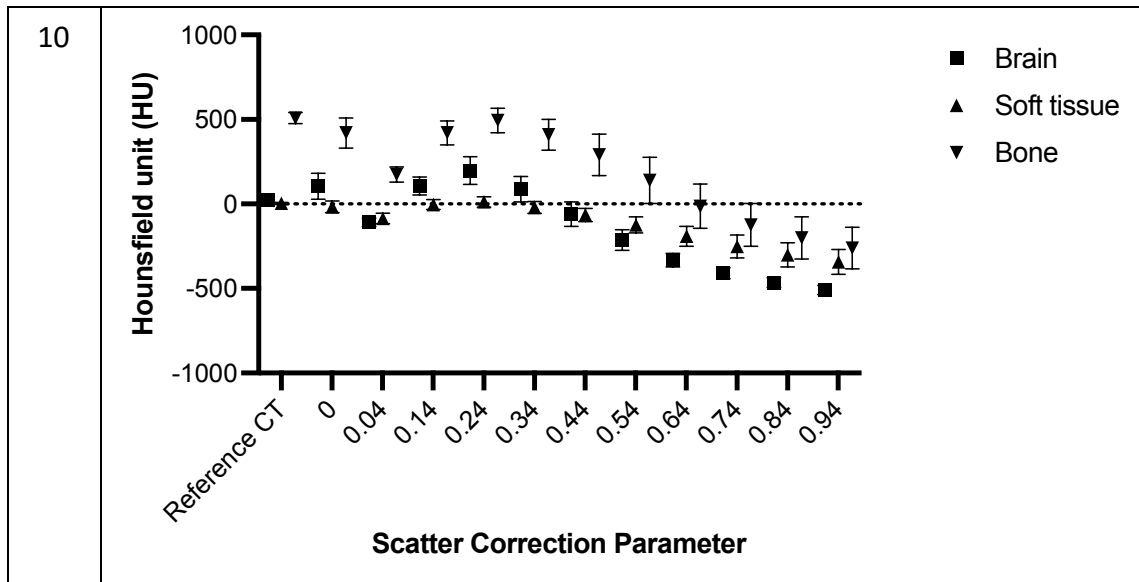| Protocol	Figure
1	
2	

Figure. The Mean and Standard Deviation (SD) of CT Numbers for voxels containing brain, soft tissue, and bone for reference CT and across different scatter correction parameters for protocols (1-6) and (8-10).